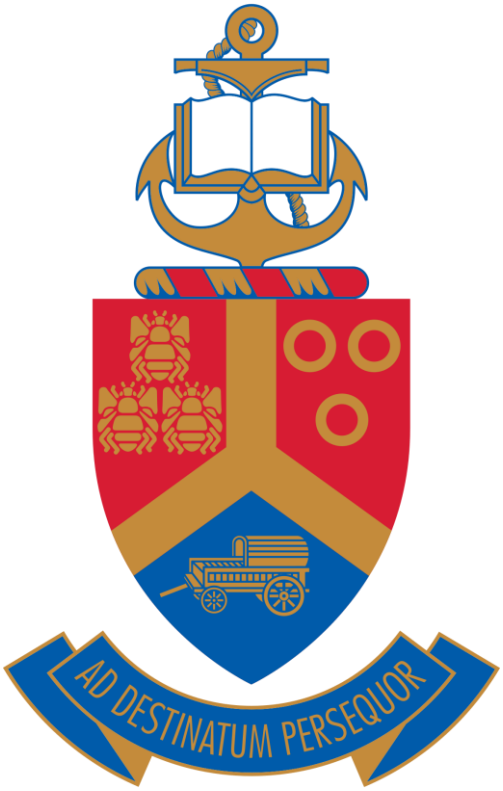

Evaluation of Iron Ore Concentrate and Micropellets as Potential Feed for Sinter Production

By

Thato Nkogatse

Supervisor: Prof. A.M Garbers-Craig

Submitted in fulfillment of the requirements for the degree of

Masters of Engineering

In

Metallurgical Engineering

© University of Pretoria

ABSTRACT

The use of iron ore concentrate has become of interest as the demand for higher grade sinter feed is increasing. The fine nature of the concentrate however raises concerns as it can affect permeability during sintering which could have a drastic impact on sinter productivity. In this study the use of iron ore concentrate and micropellets as sinter feed was evaluated. Five mixtures containing different proportions of iron ore concentrate and micropellets, together with iron ore fines, were prepared. These mixtures were agglomerated through pilot scale sinter pot tests, followed by measuring the sinter strength, reduction disintegration and reducibility. Samples of the produced sinters were also subjected to X-ray Fluorescence (XRF), X-ray Diffraction (XRD) and Scanning Electron Microscopy – Energy Dispersive Spectroscopy (SEM-EDS) analyses for mineralogical analysis, and Micro focus X-ray tomography for granule and sinter structure analysis.

Granulation and permeability tests revealed that the mixture containing 0% micropellets – 40% concentrate showed superiority in material transfer efficiency of just over 95% while the mixture containing 30% micropellets – 10% concentrate showed superiority in permeability of over 38 Japanese Permeability Units. Micro focus X-ray tomography analysis on the wet granules revealed three main layering mechanisms namely; auto layering, coalescence and adhesion of micropellets. Auto layering was observed for all mixtures, coalescence was observed for the 0% micropellet – 40% concentrate mixture and the adhesion of micropellets was observed on the 40% micropellet – 0% concentrate mixture. Auto layering was slightly more extensive in the 0% micropellet – 40% concentrate, however it remained fairly similar across the other sinter mixtures.

X-ray diffraction analysis (XRD) revealed an increase in hematite as micropellet content increased. The analysis also revealed high total SFCA content for the 0% micropellet – 40% concentrate sample, which decreased as micropellet content increased. This was mainly associated with a decrease in reactivity. Optical microscopy revealed significant precipitation of secondary hematite, magnetite and columnar SFCA in the mixtures containing more concentrate, compared to those containing more micropellets. It also revealed a pronounced presence of acicular SFCA in the micropellet-rich mixtures. SEM analysis revealed the presence of hematite, magnetite, columnar SFCA, acicular SFCA-I, larnite and a glassy phase. Scanning electron microscopy (SEM) using energy dispersive spectrometry (EDS) revealed similar phase compositions across the different sinter mixtures. This was mainly associated to similar chemical compositions of the starting mixtures. Analysis of the sinter structure particles through MF-XRT revealed that sinters produced from the base case, 0% micropellet – 40% concentrate and 20% micropellet – 20% concentrate appeared denser than the 10% micropellet – 30% concentrate and 30% micropellet – 10% concentrate. Micropellets were seldom detected in the sinters produced. However,

© University of Pretoria

micropellets that were individually subjected to a sinter process consisted of an unreacted hematite-silica core surrounded by a Fe-rich rim.

It was further determined that the introduction of iron ore concentrate and micropellets to the sinter feed did not significantly impact sinter strength and reducibility as similar tumble indices (TI) and reducibility indices (RI) were observed. A variation in reduction disintegration index (RDI) was however seen with micropellet-rich sinters showing a higher degree of degradation compared to concentrate-rich sinters (increasing $RDI_{-3.5\ mm}$ and $RDI_{-0.5\ mm}$). It would therefore be viable to rather use iron ore concentrate as sinter feed as it has a lower production cost compared to micropellets and produces less fines on reduction.

Keywords: sintering, concentrate, micropellets, granulation, permeability, mineralogy, microstructure

© University of Pretoria

DECLARATION

I Thato Curt Ntladi Nkogatse with the identity number: 960225 5202 081 declare that the produced written work was produced by myself with no copying of other authors' work without appropriate interpretation and reference techniques applied on the published material. I therefore take complete responsibility of the work produced in this document.

Signature of author

30 April 2020
Date

© University of Pretoria

PREFACE

I started this work with a desire to obtain a deeper understanding of the role of iron ore concentrate and micropellets in iron ore granulation and sintering. I am aiming for this work to provide important insights towards the development of advanced sintering methods. I would therefore like to thank everybody that supported me and provided me with the necessary patience to complete this work, this includes my mother Ouma and father Phillip Nkogatse who supported me in both my undergraduate and postgraduate years. I would also like to thank Prof Andrie Garbers-Craig whom I also call Mangwane for her significant contribution to my work. These among many helped me walk smoothly on this treacherous path.

Thank you and God bless.

© University of Pretoria

ACKNOWLEDGEMENTS

I would like to extend my gratitude to Prof. Andrie Garbers-Craig my supervisor together with the rest of the Center of Pyrometallurgy team for the encouragement and support I received from you guys. It has been a real pleasure working amongst great minds and I really gained a lot.

This project would not have existed if it was not for the financial support from Anglo American and for that I say thank you. I would also like to extend my gratitude to Kobus Vreugdenburg, Phindile Mbele, Andre Dippienaar and my brothers at Value-In-Use as it is because of their support that I was able to complete my project.

I would also like to thank Dr. Frikkie de Beer, Jakobus Hoffman and Lunga Bam for assisting me with the Micro Focus X-ray Tomography during my study of quasi-particle and sinter structures.

Scanning Electron Microscopy and Energy Dispersive Spectrometry played a major role in this project, I would therefore like to thank Carel Coetzee as well as the IMMRI team for assisting me with utilizing the equipment.

X-ray Diffraction analysis and mineral phase quantification also played an integral role in my research and I would like to thank Wiebke Grote for her assistance with my project.

Thank you.

© University of Pretoria

TABLE OF CONTENTS

© University of Pretoria

© University of Pretoria

LIST OF FIGURES

© University of Pretoria

© University of Pretoria

© University of Pretoria

LIST OF TABLES

© University of Pretoria

Chapter 1
Introduction

Iron ore is still a key component in the production of steel, currently over 70% of steel produced comes from iron ore (Poveromo, 2010, 2018). The availability of high-grade iron ore is however depleting and the use of concentrate is on the rise. Since iron ore concentrate comes from complex beneficiation processes, it is very fine and cannot be used directly in the blast furnace due to permeability and clogging concerns (Pal *et al.*, 2013; Pettersson, 2015). It is therefore necessary to agglomerate the fine ore prior to addition into the blast furnace. Sintering and pelletization are typical methods during which iron ore is agglomerated, however pelletization has been the most practical method to agglomerate iron ore concentrate due to its ultra-fine nature (Eisele and Kawatra, 2010; Mbele, 2012; Mežibrický and Goettgens, 2019).

Iron ore micropellets are produced by balling a mixture of iron ore concentrates and binders to form -5+1 mm spherical particles. Similar to the pelletization process, binders are also used to ensure satisfactory green strength. Also similar to the pelletization process, it is required that the feed particle size distribution be such that 80% of the material passes 200 mesh (74 microns) and have a minimum surface area of 900 cm^2/g (Roshan *et al.*, 2018). In South Africa the advancement of iron ore beneficiation technology has allowed for the upgrading of the previously discarded slime leading to the production of a hematite concentrate (Mbele, 2012).

Despite a coarser particle size distribution compared to the iron ore concentrate, the top size of iron ore micropellets is still lower than the bottom size of iron ore generally accepted in the blast furnace. A significant amount of work is therefore being undertaken to assess the viability of utilizing iron ore micropellets as feed to the sinter making process together with the existing iron ore fines (Pal *et al.*, 2013; Nyembwe *et al.*, 2016b).

The aim of this work was focused on assessing the viability of utilizing mixtures of Northern Cape iron ore concentrate and micropellets as feed for sinter making. This was done by analyzing the green sinter bed, sinter mineralogy, sinter properties as well as sinter structure.

© University of Pretoria

Chapter 2
Literature Review

2.1 Overview on the application of iron ore concentrate and micropellets in sinter making

The role of ultrafine material (< 200 µm) during the granulation of iron sinter mixtures is known to lead to quasi-particle formation. The ultrafine materials that adhere to the coarse particles also assist in the attachment of the quasi-particles to each other (Fernández-González *et al.*, 2017b). The introduction of ultrafine material such as iron ore concentrate depends on a number of factors such as moisture as well as granulation time (Lwamba, 2007; Fernández-González *et al.*, 2017b). Mixtures with too high ultrafine contents are however known to have a drastic impact on sinter bed permeability.

The impact of the introduction of ultrafine materials in granulation and sinter making has been noted by a few authors; Fan *et al.*, (2013) reported that the addition of ultrafine iron ore improves the sintering conditions by increasing reaction surface area which in turn improves sinter quality. Fernández-González *et al.*, (2017a) also established that the addition of ultrafine material during granulation improves overall strength of the sinter bed; the ultrafine material tends to cement the particles together when moisture is driven off during sintering. Hsieh, (2017) however noticed both degradation and an improvement in sintering conditions resulting from the addition of iron ore concentrates. It was seen that fine (-20 µm) concentrate improved sinter bed permeability as well as productivity while a coarse (+40 µm) concentrate showed an opposite effect. Work conducted by Nyembwe *et al.*, (2016a) however showed a slight decrease in sinter bed permeability as a result of the addition of iron ore concentrate (-100 µm; Nyembwe *et al.*, (2016b)). From a mineralogical perspective, Fröhlichová *et al.*, (2018) noted that the addition of iron ore concentrate to sinter did not change the resulting mineralogy however changed slightly the respective phase quantities.

Although iron ore concentrate was introduced in its fine form in some cases, some authors studied the viability of the introduction of green micropellets to the sinter feed. Nyembwe *et al.*, (2016a) studied the introduction of iron ore micropellets to the sinter mixture and noted a slight decrease in permeability compared to the base case. Roshan *et al.*, (2018) also studied the effect of iron ore micropellets on sinter permeability, the study also observed the behavior of micropellets under different moisture conditions. Pal *et al.*, (2013) studied the viability of lime and coke fines addition to the production of micropellets. The micropellets were subjected to carbon dioxide treatment and it was noted that such treatment and pre-conditioning led to slight improvements in Abrasion Index as well as sinter yield. The process of micropellet production has allowed an increased use of ultrafine material in the sintering process with some authors reporting an increase of 30% in ultrafine use (Pal, 2016). Umadevi *et al.*, (2011) observed the effect of iron ore particle size on sinter quality. It was found from their study that the alumina content of the finer size particles was relatively higher compared to coarser size particles.

© University of Pretoria

In this study the comparison of mixtures containing iron ore concentrate and micropellets is based only on particle size as all size fractions had the same chemical composition.

2.2 Iron ore sintering

The sintering process is based on treating a mix layer of iron ore fines, return fines and fluxes in the presence of coke breeze to the action of a burner placed on the surface of the layer. In this way, heating takes place from the top to the bottom section (Fernández-González *et al.*, 2017a). The mix layer rests over a strand system and an exhaust system allows the whole thickness to reach a high enough temperature for the partial melting of the mix which eventually facilitates agglomeration. In the Dwight-Loyd system, the sintering grate consists of a continuous chain formed by the union of a series of pallet cars that make the sinter strand as shown in Figure 1.

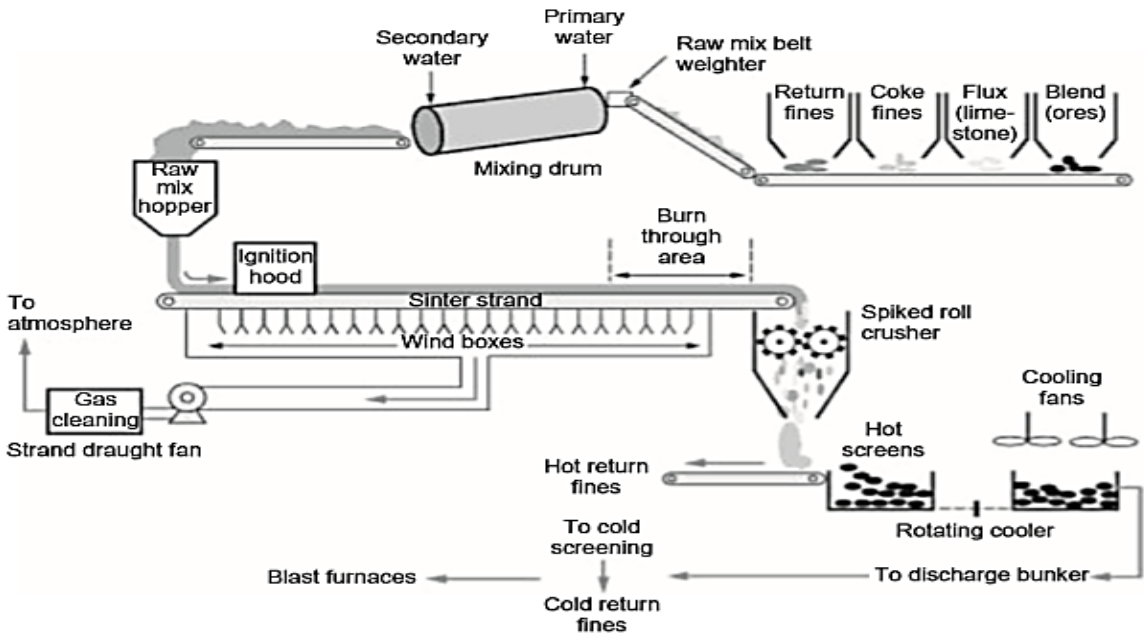

Figure 1: Typical material flowsheet during the sintering process (Lu, 2015).

During sinter production, a continuous chain of pallets passes below a feed hopper where coarse sinter particles are initially charged to form a grid layer. The introduction of the coarse sinter particles is then followed by the introduction of the granulated sinter mixture. A sinter bed therefore consists of a layer of coarse grid layer as well as green quasi-particles.

The pallet car passes below an ignition hood where the combustible material ignites at the surface of the bed. The bed is also subjected to a downdraught suction through the load. The pallet car continues moving forward and combustion progresses in the direction of gas flow. Combustion does not happen simultaneously through the entire thickness of the bed however; it happens as a horizontal layer that moves vertically across the bed. In the region above the combustion zone, a hot sintered product heats the air that passes through this layer. In this way, pre-heated air reaches the combustion area. The heat of the air/gases previously heated is absorbed in

© University of Pretoria

these cold sections, causing preheating of the load and evaporation of the water. High temperatures that cause partial melting are thereby reached, and the sintering process takes place.

The thermal efficiency is caused by heat accumulation in a layer of the load called the sintering zone or flame front. The flame front progresses at 10-30 mm/min toward the sintering grate (Fernández-González *et al.*, 2017a). In a bed height of 500-600 mm the process would take about 25 minutes.

Once the end of the strand is reached, the sintered material is discharged and subjected to cooling, crushing and screening. The obtained product can be divided into three size classes;

- Return fines which range in particle size from 0 – 5 mm
- Grid layer material ranging from 5 to 20 mm
- Blast furnace feed > 20 mm

Return fines are unavoidably formed during the sintering process, and are recycled back into the sintering process, making up 30% to 40% of the iron bearing materials (Fernández-González *et al.*, 2017a). According to the literature, return fines from the sintering process assimilate better than blast furnace fines due to lower high Ca-ferrite phases (Fernández-González *et al.*, 2017a).

Four zones can be identified across the bed height (Fernández-González *et al.*, 2017a);

- Cold and wet zone: This is the zone of the sinter bed with a temperature lower than 100 ˚C. This area is formed by the mix to be sintered, with the upper layer saturated in water/water vapour.
- Drying zone: Sinter area with temperatures between 100 ˚C and 500 ˚C. The vaporization of the free moisture of the mix and subsequent dehydration of hydroxides take place.
- Reaction zone: This zone reaches a maximum of 1250 to 1480 ˚C. It includes the zone of the sinter bed with a temperature ranging from 500 (coke ignition beginning) to 900 ˚C (cooling). The main processes that happen in this zone are coke combustion (exothermal), carbonates decomposition (endothermal), solid phase reactions, reduction and re-oxidation of iron oxides and reaction and formation of the sintered mass.
- Cooling zone: This zone is found immediately after the reaction zone. Cooling and recrystallization of the sintered product takes place. There is a superficial zone where the sinter layer is more brittle than the rest of the sinter bed.

© University of Pretoria

2.3 Sinter parameters

Careful control of the sintering process is essential in ensuring that sinters of acceptable quality are produced. This is beneficial for the blast furnace as well as the sinter plant in terms of productivity.

2.3.1 Granulation

The key purpose of granulation is to produce a mixture of a coarse narrow grain size distribution. According to Figure 2, a narrow coarse size distribution gives rise to a high void fraction which in turn increases permeability. Bed void fraction is also a function of packing density. It is also important that the granules maintain their strength and roundness on the sinter bed. A drop in packing density may result from the destruction of the granules and can cause a significant drop in permeability (Geerdes *et al.*, 2009).

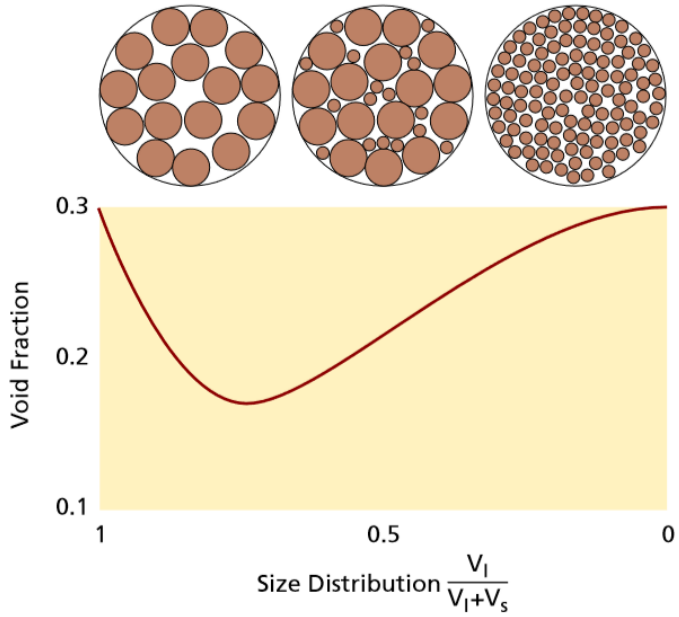

Figure 2: Relationship between bed void fraction and particle size distribution, V_l refers to large particles and Vs refers to small particles (Geerdes *et al.*, 2009).

The addition of water is also important during granulation as it is known to facilitate layering through capillary action as shown in Figure 3 (Fernández-González *et al.*, 2017b). It is also dependent on factors such as ore porosity, particle size distribution of the mixture as well as reactivity of the limestone if added. It was reported that ores with high porosity have high moisture saturation limits which in turn make them require more water before achieving optimum permeability (see Figure 4) (Lu, 2015).

© University of Pretoria

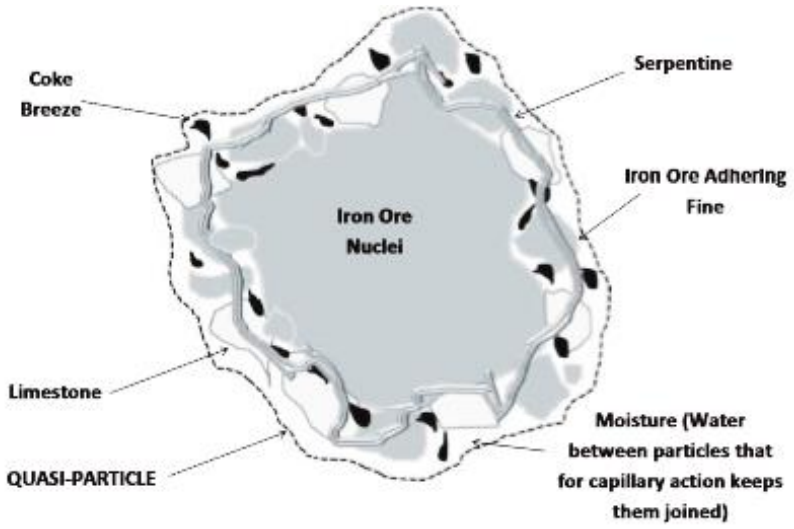

Figure 3: Quasi-particle forming as a result of granulation (Fernández-González *et al.*, 2017b).

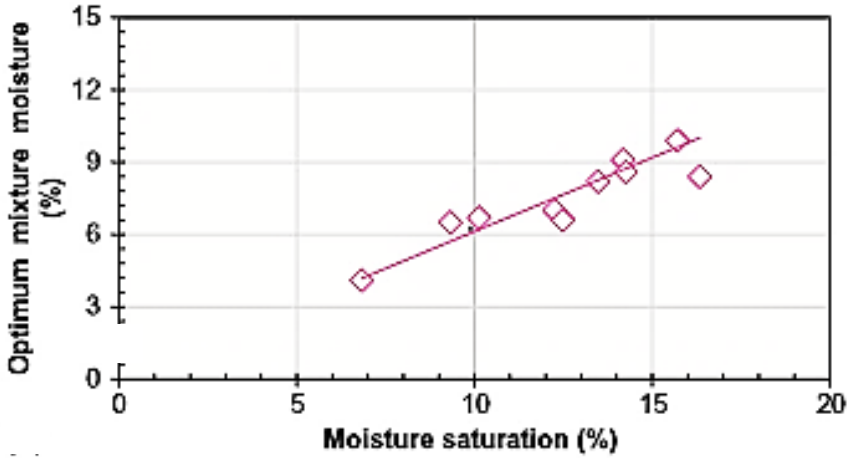

Figure 4: Influence of moisture saturation on optimum moisture required in a mixture, high porosity ores have high moisture saturation (Lu, 2015).

During granulation three different classes of material interact namely coarse nuclei, intermediate particles and adhering fines. The granulation process is said to be efficient when the interaction of these particles leads to the formation of strong granules that can attach to each other. As the adhering fines layer around the nucleus particle they should also maximize the inter-granular contact in order to facilitate melt formation between the granules during sintering. Intermediate particles are typically classified as those ranging between 0.2 mm to 0.7 mm. They are reported to have a negative impact on the granulation process, this is because they are too small to act as nuclei and too big to act as adhering fines (Formoso *et al.*, 2003; Lwamba and Garbers-Craig, 2008). The presence of ultrafine particles has also been reported to improve the granulation efficiency of certain ore mixtures. This is reported to be due to the formation of finely dispersed water bridges between the adhering fines and the nuclei (see Figure 5) (Fernández-González *et al.*, 2017b).

© University of Pretoria

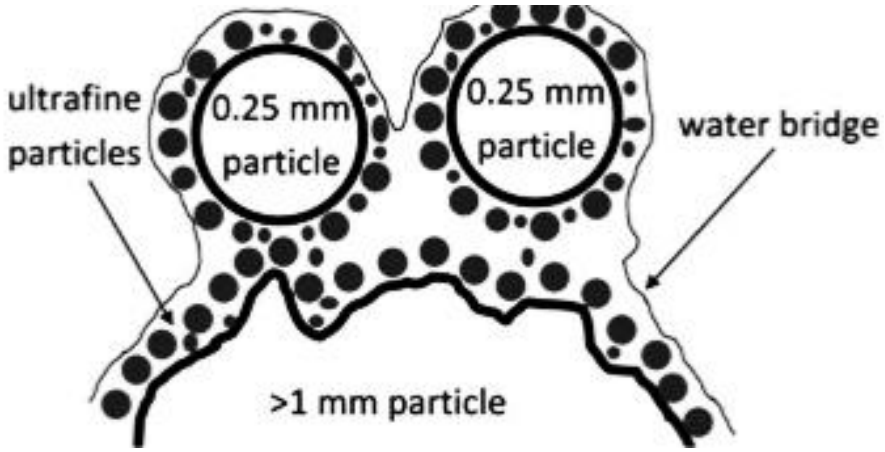

Figure 5: Ultrafine dispersed water bridge formed between adhering fines and a nucleus (Fernández-González *et al.*, 2017b).

Some studies also showed that the surface properties of the nuclei particles have an important effect on the layering ability of the adhering fines. It was found that as the contact angle between the ore particle and water decreases, the granulation efficiency increases. It was also found that nuclei with an angular orientation tends to facilitate layering better than nuclei with a spherical orientation, while nuclei with a high roughness improve the granulation efficiency (Mao *et al.*, 2013).

Improvement of granulation efficiency is also a matter of understanding the layering mechanisms taking place during granulation. Figure 6a) shows a schematic for the different layering mechanisms encountered during the granulation of mixtures containing iron ore concentrate and micropellets. Group I layering is referred to as auto layering and is shown in Figure 6a) and b). This mechanism is characterized by the larger particles maintaining their shape even when the adhering fines attach to the surface. Group II layering involves coalescence which is seen in Figure 6a) and c). This mechanism is characterized by the formation of spherical granules caused mainly by the addition of fine concentrate. Group III layering referred to as the adhesion of micropellets is shown in Figure 6a) and c). This occurs when micropellets coated with adhering fines attach to each other, upon further granulation the micropellets gets coated to form one single granule. It is however clear that the high sphericity of the micropellets does not provide sufficient contact area for the micropellets to attach sufficiently. Group IV layering referred to as two stage layering occurs when adhesion occurs between larger particles and small granules and is shown in Figure 6a) and d). Observing both groups III and IV layering mechanisms in Figure 6d) it becomes clear that there is insufficient adhering fines and these particles are most likely to disintegrate back into their constituent parts (Nyembwe *et al.*, 2016b, 2017).

© University of Pretoria

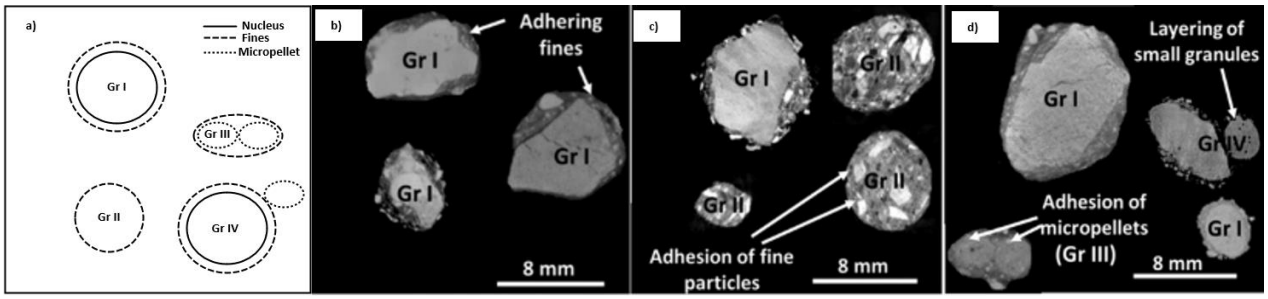

Figure 6: Different layering mechanisms resulting from the addition of different iron ore material in sinter mixtures a) schematic b) base case c) 20% concentrate d) 20% micropellets (Nyembwe *et al.*, 2016b).

2.3.2 Permeability

Permeability is an important parameter in sintering because the process highly depends on gas movement across the sinter bed. As previously mentioned, granulation is an important fundamental process which should be carefully controlled in order to ensure that maximum permeability is achieved.

Optimum moisture is the level of moisture where permeability is maximum, and this is determined prior to the sintering process. Figure 7 is a typical graph used for selecting moisture for maximum permeability. The permeability for all the mixtures shown in Figure 7 is low at low moisture and this is followed by an increase in permeability until a maximum is reached (mostly at 5.5% moisture). High moisture addition also leads to a drop in permeability as a result of the formation of deformable granules (Venkataramana *et al.*, 1999). It was however also discussed in the previous section that ore porosity influences how much moisture needs to be added to achieve maximum permeability.

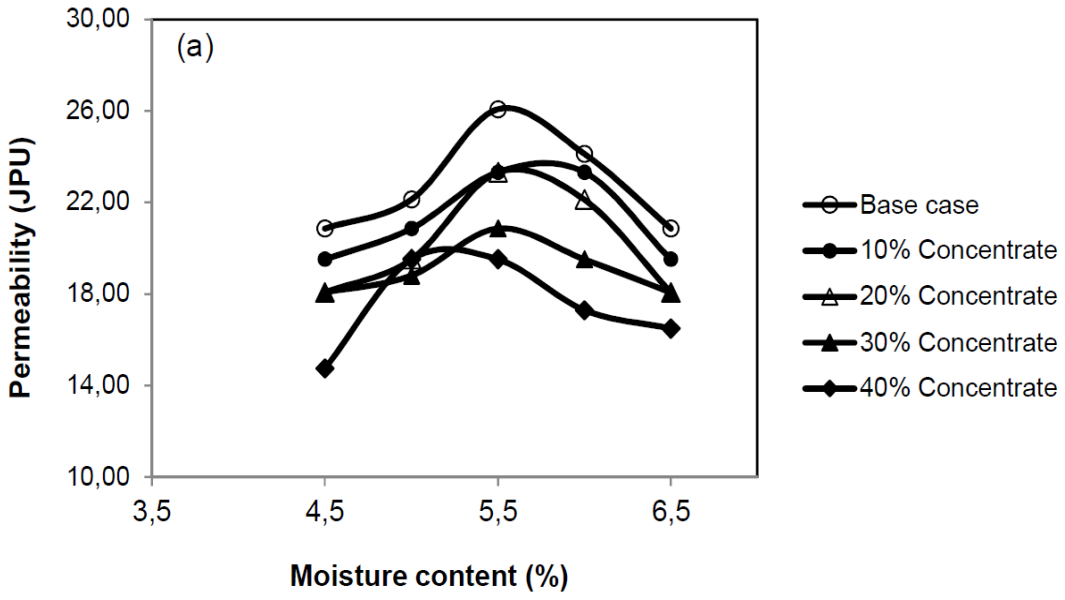

Figure 7: Relationship between moisture and permeability for sinter mixtures with different quantities of iron ore concentrate (Nyembwe *et al.*, 2016a).

© University of Pretoria

Mixtures containing iron ore concentrate and mixtures containing iron ore micropellets have been reported to show a decrease in permeability (Figure 8). This was a result of a reduction in mean granule size which caused a reduction in bed void fraction (Nyembwe *et al.*, 2016b).

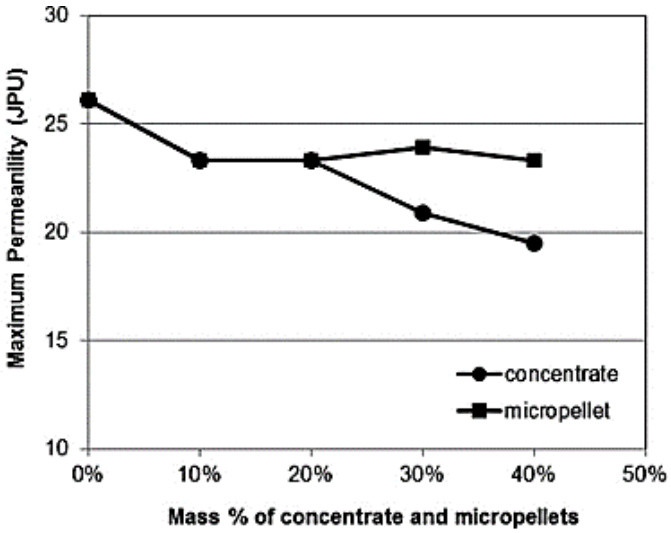

Figure 8: Effect of concentrate and micropellet addition on maximum permeability (Nyembwe *et al.*, 2016a).

2.3.3 Thermal densification

Thermal densification occurs when the fluxes added and the fine iron ore react to form a low melting liquid (known as a melt) in the flame front. The melt continues to react with nearby iron ores on heating and solidifies during cooling to form a matrix bonding the unreacted ore particles together. During thermal densification, the effective porosity of the sinter bed decreases, while properties such as mechanical strength increase (Lu. 2015).

The process of thermal densification occurs at the flame front through the following mechanisms (Lu, 2015):

- Reordering of granules at the flame front – the first melt is subjected to capillary forces which pulls it into the pores and causes the unreacted particles to rearrange into a more favorable packing arrangement that allows for melt movement.
- Assimilation and precipitation – the smaller reactive particles are assimilated preferentially when they are in contact with the melt to contribute to the final melt and the melt solidifies onto the unreacted larger particles, leading to densification.
- Final densification – densification of the solid skeletal network, leading to melt movement from efficiently packed regions into pores.

The efficiency of thermal densification is dependent on the bed packing which is mainly determined by granulation and the PSD.

© University of Pretoria

The viscosity of the melt is also another important factor to consider and depends largely on the sintering temperature as well as the chemical composition of the melt. This becomes clear when observing Figure 9 which shows a decrease in viscosity as temperature increases and an increase when the concentrations of various oxides such as SiO_2, Al_2O_3 and MgO are increased (Lu *et al.*, 2007).

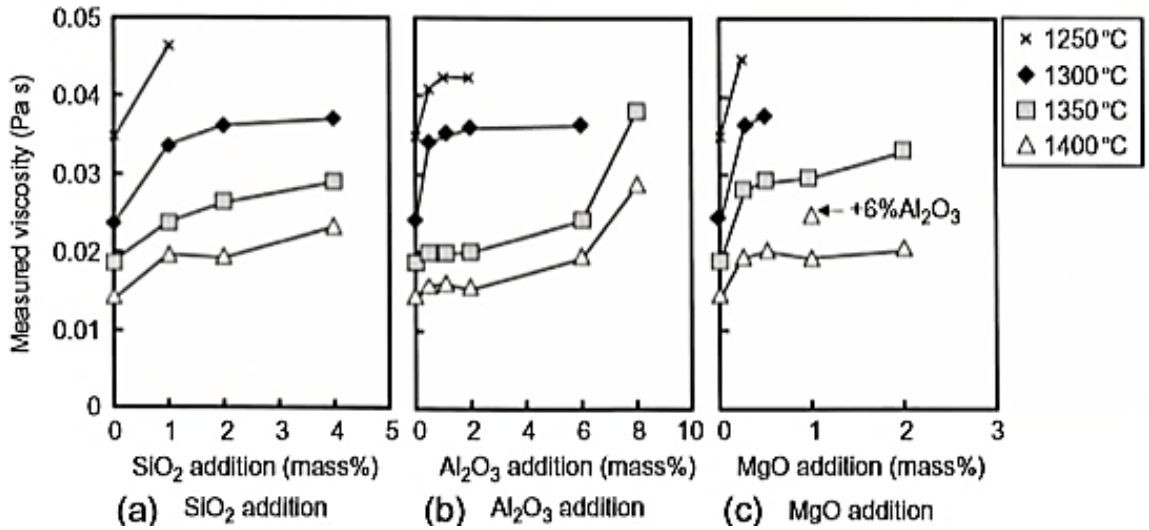

Figure 9: Relationship between melt viscosity and sintering temperature and chemical composition (Lu, 2015).

2.3.4 Production rate

The production rate of sintering is a great techno-economic indicator of the sintering process and is calculated according to Equation 1. The time factor in the equation is the time it takes for the sintering process to come to an end. This strongly depends on the sinter bed permeability. The bed is said to have fully sintered when the off gas temperature reaches a maximum value, as this suggests that the flame front has reached the bottom of the bed (Umadevi *et al.*, 2010).

$$\boldsymbol{P} = \frac{\boldsymbol{m_{total} - m_{-5mm} - (m_{grid_{in}} - m_{grid_{out}})}}{\boldsymbol{A * t}} \qquad \textbf{Equation 1}$$

Where

P = productivity (t/m^2/day)

m_{total} = total mass of sinter produced (t)

m_{-5mm} = mass of the - 5 mm fraction (t)

m_{gridin} = mass of grid layer added onto the strand (t)

$m_{gridout}$ = mass of grid layer recovered (t)

A = area of the grate (m^2)

t = sintering time (day)

© University of Pretoria

Since it normally takes longer for a flame front to move through a bed with low permeability under constant pressure, it takes longer to complete sintering, hence a lower production rate will be experienced. A flame front that is too fast can however be of detriment in terms of production rate as it will increase the amount of return fines (the -5 mm fraction). The melt must be given enough time to assimilate the relict material before the flame front passes so as to produce sinters with a higher strength.

The mean size of the iron ore particles has also been reported to have an influence on the productivity and this is mainly due to the effect that mean size has on permeability (Umadevi *et al.*, 2011). Figure 10 gives an indication of how the mean size affects the flame front speed and fines production. As it was observed in Figure 2, large particles with a uniform distribution tend to have a higher void fraction. Higher void fractions suggest better passage of the flame front across the sinter bed. Fines production is primarily impacted by the ratio of nuclei to adhering fines. Low mean size suggests excess amounts of adhering fines which eventually lead to fines production. As the mean size increases, adhering fines decrease while coarser nuclei increase, large amounts of coarse particles would therefore result in less fines produced.

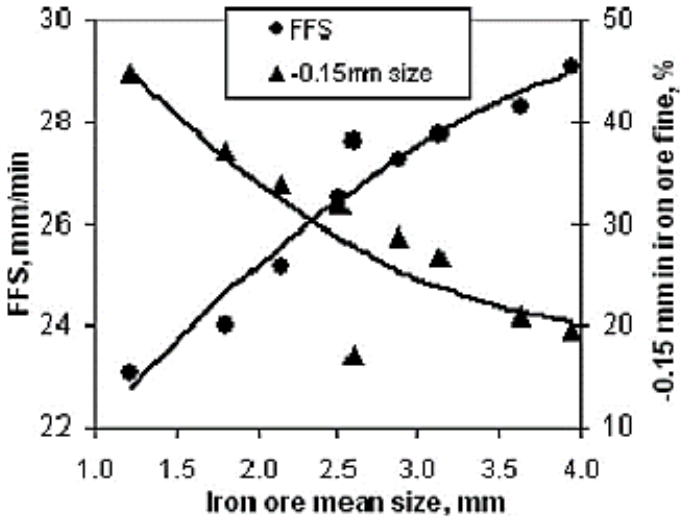

Figure 10: Relationship between iron ore mean size and flame front speed as well as fines production (FFS = flame front speed), (Umadevi *et al.*, 2011).

© University of Pretoria

2.4 Sinter mineralogy and properties

Sinter properties are mainly a function of the sintering parameters such as raw material selection, granulation and the sintering process itself (thermal stage) (Lu, 2015). This section discusses some of the important properties relating to sinter.

2.4.1 Sinter mineralogy

Iron ore sinter is a multi-phase material with a heterogeneous microstructure. Typically, the mineralogy of iron ore sinter comprises of hematite, magnetite, silico ferrites of calcium and aluminum (SFCAs) as well as silicates. Depending on process conditions, these phases can exist in different quantities as well as morphologies which will determine the microstructure which in turn determines the physical properties of the sinter (Yang and Davis, 1999; Scarlett *et al.*, 2004b). According to the literature, sinter structures comprise of the following; iron oxides (~40 – 70 vol%), ferrites such as SFCA (~ 20 – 50 vol%), silicates (~up to 10 vol%) and a glassy phase (~ up to 10%). Factors that play a role in determining the quantities as well as structure of these sinter phases include chemical composition, mineralogy and partial arrangement (Scarlett *et al.*, 2004a).

2.4.1.1 Iron Oxides

Hematite is generally the most abundant phase found in sinters. It exists in two forms viz. relict hematite (unreacted) and secondary hematite which could precipitate from the melt (Chaigneau, 1994). Relict hematite often appears dense (He_2 in Figure 11) and its presence is influenced mainly by the particle size of the starting ores, as finer ores tend to react with melt faster than coarser ores. This often results in complete assimilation of fine ore particles and partial assimilation of coarser ore particles (Yang and Matthews, 1997). Secondary hematite is characterized by euhedral crystal shapes and relatively smooth grain boundaries (He_3 in Figure 11) (Van den Berg and De Villiers, 2009). Magnetite-rich ores are not commonly used in sinter mixtures hence magnetite identified in sinters is mainly secondary magnetite. This magnetite forms as a result of hematite reduction under conditions of low oxygen partial pressure (Chaigneau, 1994). Secondary magnetite can also crystalize from Fe-rich melts during cooling (Kalenga and Garbers-Craig, 2010). The presence of Mg^{2+} ions in the melt can also lead to the formation of magnesio-spinels. Magnesio-spinels are often preferred as it is argued that they tend to decrease the temperature at which hematite reduces to magnetite (Panigrahy *et al.*, 1984). Since it is difficult to distinguish between pure hematite and magnetite using scanning electron microscopy, the magnesio-spinel solid solution also enables for easy identification through energy dispersive spectrometry.

© University of Pretoria

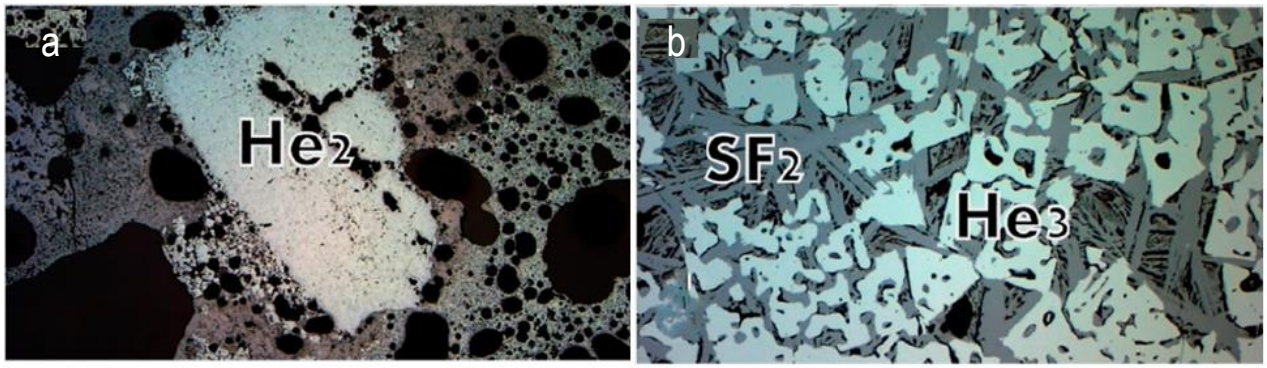

Figure 11: Optical micrographs depicting primary and secondary hematite observed by Hapugoda *et al.,* (2016) (He_2 = primary hematite; SF_2 = SFCA; He_3 = secondary hematite).

2.4.1.2 Silico ferrites of calcium and aluminum

SFCA is a major bonding phase found in iron ore sinters. It is a complex quaternary phase of $CaO.2Fe_2O_3$ solid solution with small amounts of Al_2O_3 and SiO_2 (Patrick and Lovel, 2001; De Magalhaes and Brandao, 2003). SFCA phases form a series of solid solutions which can also contain M^{2+} ions (Mumme, 2003). Considered as the main bonding phase in iron ore sintering, SFCA has been studied extensively in order to understand its role on sinter strength, reducibility and reduction disintegration (Mochon *et al.*, 2014).

Studies by Mumme, (2003) and Mumme *et al.*, (1988) on synthetic SFCA prepared from Fe_2O_3, Al_2O_3, SiO_2 and $CaCO_3$ revealed a coexistence of homologue structures that can be represented by the formula $M_{14+6n}O_{20+8n}$ with n = 0, 1 and M = Al, Ca, Si and Fe. Two different structures were observed namely; SFCA ($M_{14}O_{20}$) and SFCA-I ($M_{20}O_{28}$). Mumme, (2003) and Mumme *et al.,* (1988) also suggested a third homologue structure SFCA-II with the formula $M_{34}O_{48}$ with a unit cell volume almost similar to the sum of SFCA and SFCA-I unit cell volumes. Mumme, (2003) also reported the existence of another homologue structure ($M_{26}O_{36}$) with an XRD pattern similar to that of $Ca_5Si_2(Fe, Al)_{18}O_{36}$. It was then predicted that the structure is the next possible member of the series, corresponding to n = 2.

Scarlett *et al.*, (2004a) studied the microstructures SFCA phases based on their chemical compositions. The results revealed a coexistence of two main types of SFCA as shown in Figure 12. SFCA-I, which had high amounts of Fe and low Si, shows a platy morphology which may be acicular or needle-like in cross section. The morphology of SFCA with low amounts of Fe was columnar, blocky or lath shaped (Scarlett *et al.*, 2004a).

© University of Pretoria

Webster *et al.*, (2012) studied SFCA formation mechanisms through in-situ X-ray diffraction using hematite, calcite, gibbsite and quartz as starting materials. The following reaction mechanism was suggested:

- At 200 °C : Gibbsite decomposition starts to form alumina and water ($Al(OH)_3 = Al_2O_3 + H_2O$)
- At 600 °C : Calcite decomposition starts to form lime and carbon dioxide ($CaCO_3 = CaO + CO_2$)
- At 750 °C : Lime and hematite react to form dicalcium ferrite ($2CaO + Fe_2O_3 = 2CaO.Fe_2O_3$)
- At 950 °C : C_2F reacts with Fe_2O_3 to form CF ($2CaO.Fe_2O_3 + Fe_2O_3 = CaO.Fe_2O_3$)
- At 1000 °C : Formation of SFCA-I and SFCA begins. ($CaO.Fe_2O_3 + Fe_2O_3 + SiO_2 + Al_2O_3$ = SFCA-I + SFCA)
- Above 1200 °C : SFCA-I is consumed by the reaction with hematite and silica to form SFCA

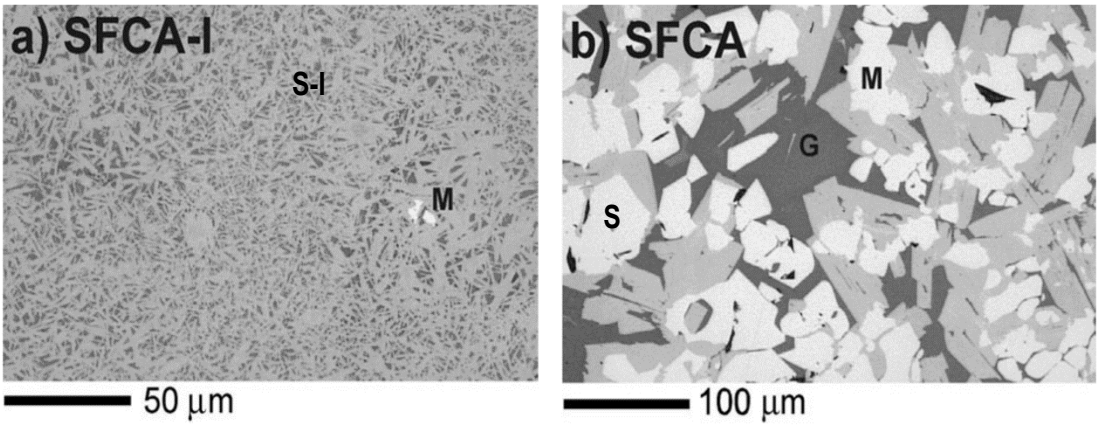

Figure 12: Electron backscatter images of a) SFCA-I and b) SFCA (S = SFCA; S-I = SFCA-I needles; M = magnetite; G = glass) (Scarlett *et al.*, 2004).

2.4.1.3 Silicates

The silicate phases in sinter typically include a crystalline calcium silicate and a non-crystalline slag phase. The slag phase is formed by partial melting of fluxes, which is facilitated by low basicity and excessive sintering temperatures (typically over 1300 °C). The non-crystalline slag phase is glassy and results from the solidification of the silicate melt with higher viscosity. Although the slag phase normally appears in small capillary fillings between the crystalline phases, instances where melt viscosity is too low or sintering temperature is too high, it can be seen to cover larger areas (Figure 13a). Dicalcium silicate (Ca_2SiO_4) also called larnite is the most common crystalline calcium silicate found in iron ore sinter (labeled L in Figure 13b). Similar to the slag phase, it usually exists in small capillary fillings between other micro-constituents (Hapugoda *et al.*, 2016). Larnite has been reported to be a potential contributor the loss of strength in iron ore sinter if β-Ca_2SiO_4 to γ-Ca_2SiO_4 transformation takes place during cooling (Patrick and Lovel, 2001). Larnite is also know to incorporate a wide variety of impurities such as phosphorous in industrial sinters which can be detrimental to steel quality (Mežibrick and Goettgens, 2019; Patrick and Lovel, 2001).

© University of Pretoria

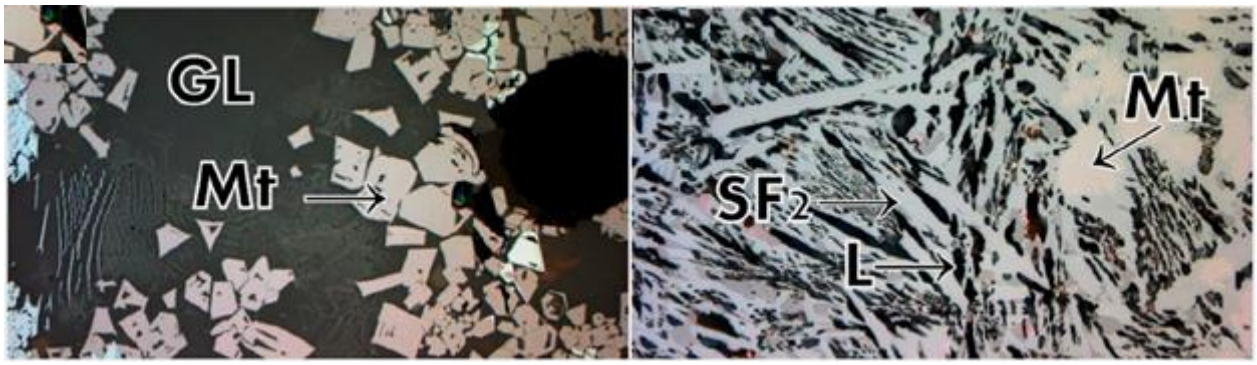

Figure 13: Optical micrographs of iron ore sinter depicting a) a glassy phase and b) larnite phase (GL = glass; Mt = magnetite; SF_2 = SFCA; L = larnite) (Hapugoda *et al*., 2016).

2.4.2 Sinter strength

Sinter cold strength is an important factor in determining the overall sinter quality. Iron ore sinter must have enough strength to withstand handling and transportation between the sinter plant and the blast furnace. For sinter to be regarded as having sufficient strength, it has to have a minimum of 70 mass% retained after tumbling on the 6.3 mm sieve, this is known as the Tumble Index (TI) (Bhagat *et al.*, 2006).

According to the literature, sinter strength is highly dependent on the ability of the individual phases to resist cracking and crack propagation. Dense phases such as primary hematite, magnetite and SFCA are known to provide fracture toughness, while SFCA-I (acicular SFCA) with a porous microstructure is generally desired for the prevention of crack propagation (Chaigneau, 1994; Husslage *et al.*, 1999; Zi-wei *et al.*, 2006). Umadevi *et al.*, (2011) who studied the relationship between the mass% of the SFCA and sinter strength noticed a considerable increase in strength as the SFCA content increased (Figure 14). Zi-wei *et al.* (2006) on the other hand examined how mixtures of different mineral compositions and microstructures impact crack resistance. It was noticed from the study that SFCA-I played a dominant role in improving crack resistance. Whilst cracks were propagated at loads of 245 mN for structures of SFCA (columnar SFCA), magnetite and silicates, it took a minimum of 490 mN for crack propagation for structures of SFCA-I. It was also reported that for finer a SFCA microstructure, loads can be increased to 1960 mN before a crack can propagate (Zi-wei *et al.* 2006).

© University of Pretoria

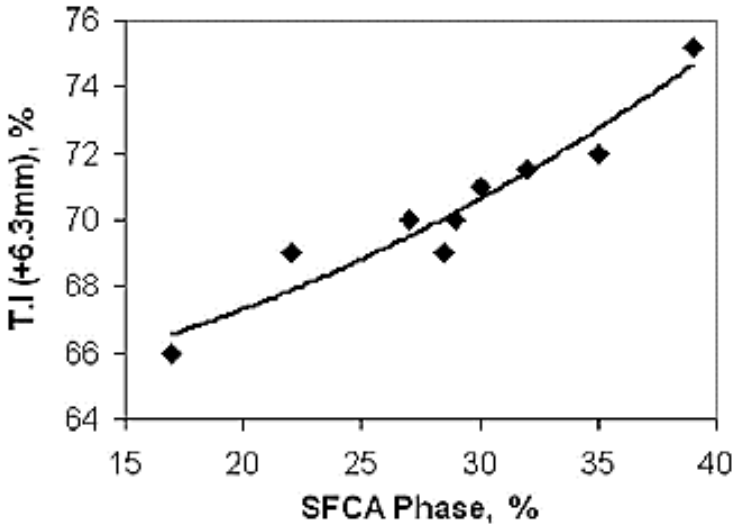

Figure 14: Influence of SFCA on tumble index (Umadevi *et al.*, 2011).

2.4.3 Reduction disintegration

The reduction disintegration index is measured to assess the ability of sinter to maintain strength in the upper part of the furnace as reduction starts to progress. The breakdown of sinters at the top part of the furnace would have a deleterious effect on the furnace permeability.

The primary cause of reduction disintegration in sinter is the transformation of iron oxide from hexagonal hematite to cubic magnetite. This transformation is accompanied by a significant change in volume and lattice distortion. Internal stresses can be generated by the volume change, which would result in propagation of cracks and fragmentation of the sinter particle. Reduction disintegration was also reported to be facilitated by a large presence of skeletal rhombohedral hematite, SFCA (columnar SFCA) as well as a glassy phase (Husslage *et al.,* 1999). Similar to cold strength, the presence of phases with a porous microstructure such as SFCA-I assists in absorbing such stresses, hence preventing disintegration. Fan *et al.*, (2013) reported that the addition of an ultrafine concentrate (produced from a high-pressure grinding roll step) facilitated the stabilization of SFCA-I which assisted in improving reduction disintegration. The stabilization of magnetite during sintering was also seen to improve the disintegration resistance and reduce coke consumption in the blast furnace (Van den Berg and De Villiers, 2009).

2.4.4 Reducibility

The reducibility is a measure of how well a reducing gas enters the core of the sinter particle. It is largely determined by the porosity and mineral composition of the sinter cake (Higuchi *et al.,* 2006). Several authors reported that the morphology of SFCA structure plays an important role in determining sinter reducibility. It is argued that the fine porosity found in SFCA-I provides a reaction area of contact between reducing gas and solid particles (Husslage *et al.,* 1999; Zi-Wei *et al.,* 2006; Higuchi *et al.*, 2006). According to a study by Hida *et al.*,

© University of Pretoria

(1983), sinter reducibility is directly related to the internal pore volume and surface area of the ore. Umadevi *et al.* (2011) argued that, high concentrations of relict hematite and low magnetite contents improve sinter reducibility. Kalenga and Garbers-Craig, (2010) also found that increasing MgO contents led to a decrease in reducibility as MgO stabilizes spinel formation (Figure 15).

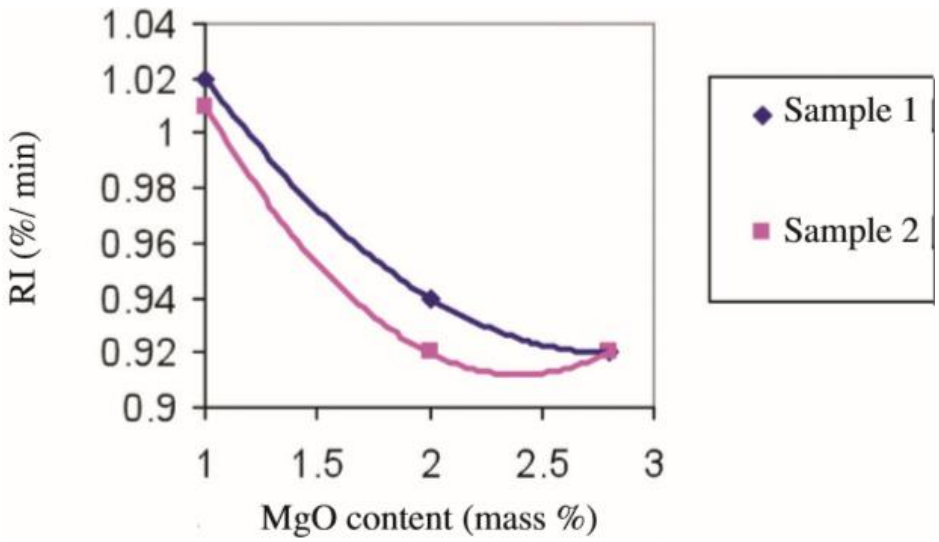

Figure 15: MgO addition on sinter RI, sample 1 is dolomite and sample 2 is fused magnesia (Kalenga and Garbers-Craig, 2010).

© University of Pretoria

Chapter 3
Experimental procedure

The objectives of this study were:

1. To study the granulation behavior and mechanisms of mixtures containing both concentrate and micropellets.
2. To measure moisture levels at which the mixtures achieve maximum permeability.
3. To evaluate the properties of sinters produced from the mixtures containing concentrate and micropellets.
4. To analyze the mineralogical and microstructural differences in mixtures containing the different proportions of concentrate and micropellets.

The tests related to granulation and sintering were conducted at Anglo American Value-In-Use pilot plant in Pretoria West; X-ray micro-tomography analysis was conducted at the Nuclear Energy Corporation of South Africa and mineralogical studies were conducted at the University of Pretoria.

3.1 Preparation of raw materials

The raw materials used for this study included two types of standard Northern Cape iron ore fines (A and B), iron ore concentrate, iron ore micropellets (prepared from the concentrate and starch), Suprachem coke, burnt lime and dolomite. The chemical compositions and particle size distributions of the raw materials are shown in Table 1 and Figure 16, while the particle size distributions of the sinter mixtures before granulation are given in Table 2: Particle size distributions of sinter mixtures before granulation (in wt%).Table 2. Iron ore micropellets were prepared from the concentrate hence they had similar chemical compositions. The ultrafine nature of the concentrate with respect to the rest of the material can be seen in Figure 16. Table 2 shows that as micropellets increase in the sinter mixture, there was a considerable decrease in the -0.5 mm fraction. There was also an increase in the +1 mm fraction.

Table 1: Chemical compositions of the raw materials.

Material	Fe(tot)	FeO	Fe_2O_3	K_2O	Na_2O	CaO	MgO	MnO	Al_2O_3	SiO_2
NC[1] fines A	63,8	0,27	91,81	0,15	0,01	0,00	0,02	0,26	2,45	5,02
NC[1] fines B	65,2	0,27	93,86	0,21	0,07	0,17	0,02	0,05	1,20	4,14
Concentrate	66,3	0,10	95,64	0,21	0,01	0,11	0,03	0,05	1,34	2,50
Micropellets	66,3	0,00	95,79	0,21	0,01	0,11	0,03	0,00	1,34	2,51
RF[2]	58,7	2,03	79,87	0,22	0,03	9,05	2,81	0,25	1,67	4,07
Coke ash	1,35	0,93	9,54	1,43	0,71	5,27	1,97	0,22	23,97	55,95
Calcined Dolomite	0,49	0,73	0,44	0,55	0,00	94,61	2,05	1,08	0,27	0,27
Doloma	0.97	0.0	2.59	0.04	0.00	56.03	37.48	1.56	0.19	2.12

[1] Northern Cape fines.
[2] Return fines, produced from sinters containing no concentrate nor micropellets.

© University of Pretoria

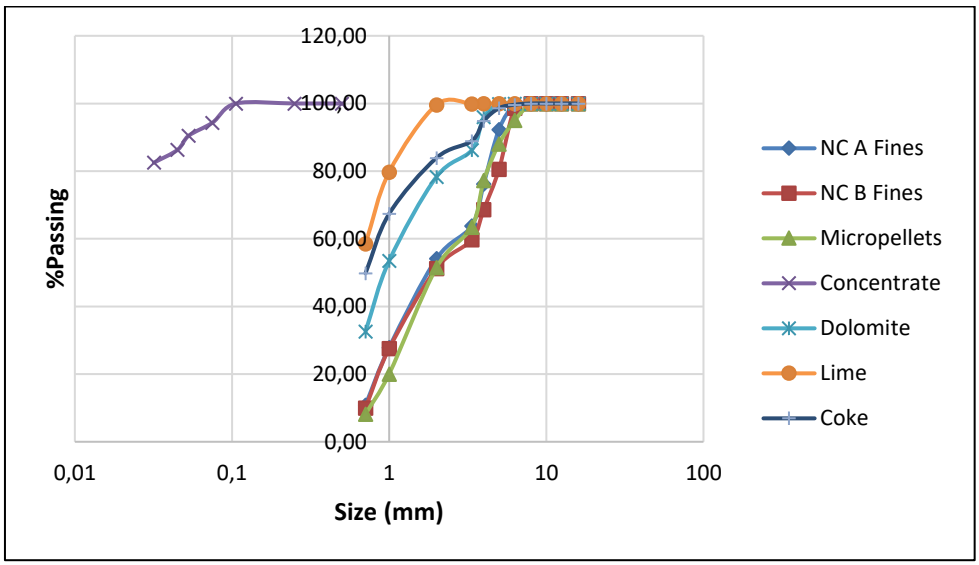

Figure 16: Particle size distribution of the starting raw materials.

Table 2: Particle size distributions of sinter mixtures before granulation (in wt%).

Size (mm)	BC	0% MP	10% MP	20% MP	30% MP	40% MP
+4	29,63	19,29	21,97	24,67	27,36	30,04
-4 + 3.35	7,74	5,29	6,17	7,05	7,93	8,81
-3.35 + 2	23,89	16,66	18,97	21,29	23,60	25,92
-2 + 1	18,14	12,96	13,83	14,70	15,58	16,45
-1 + 0.5	6,99	4,86	4,86	4,86	4,86	4,86
-0.5	13.60	40.95	33.60	26.22	18.86	11.51

The raw materials were used to make up sinter mixtures with varying amounts of iron ore concentrate and iron ore micropellets, the respective mass ratios and sample names are given in Table 3. The total composition of each mixture is shown in Table 4. The return fines used in each of the mixtures were individually prepared by burning 'dummy' sinters of the same composition but without the addition of any concentrate or micropellets.

Table 3: Ore ratios for each sinter composition

Ore	BC	0% MP	10% MP	20% MP	30% MP	40% MP
NC fines A	50	30	30	30	30	30
NC fines B	50	30	30	30	30	30
Concentrate	0	40	30	20	10	0
Micropellets	0	0	10	20	30	40
Total	**100**	**100**	**100**	**100**	**100**	**100**

© University of Pretoria

Table 4: Total composition of each sinter mixture without moisture.

Material	BC	0% MP	10% MP	20% MP	30% MP	40% MP
NC fines A	24.37	15.98	16.03	15.61	15.50	15.12
NC fines B	24.37	15.98	16.03	15.61	15.50	15.12
Concentrate	0.00	21.24	15.98	10.38	5.15	0.00
Micropellets	0.00	0.00	5.33	10.38	15.46	20.10
RF	32.73	27.87	27.38	29.52	30.01	31.73
Coke	4.31	4.59	4.61	4.49	4.46	4.35
Lime	7.19	5.81	5.83	5.68	5.64	5.50
Dolomite	8.02	8.54	8.57	8.35	8.29	8.08

BC = Base Case
MP = Micropellets
RF = Return Fines

3.2 Granulation

Granulation is carried out to produce a narrow particle size distribution which in turn improves permeability and productivity of the sinter plant. For each sinter mixture, 30 kg samples of varying moisture contents were prepared and fed into a 500 mm x 400 mm pilot granulation drum (Figure 17). The 30 kg samples were then mixed in the drum rotating at 20 rpm. Prior to starting up the drum, the required water was added in order to facilitate quasi-particle formation. Granulation was carried out for 2 minutes after which the material was discharged into a tray where it was sampled for permeability testing. Mixtures with a maximum permeability were also sampled for granule size distribution measurements.

Figure 17: Pilot granulation drum (500 x 400) used at Anglo American VIU.

© University of Pretoria

3.2.1 Permeability – Moisture tests and granule size distribution

Permeability was measured for the 4% to 6% moisture range at 0.5% increments. For the base case mixture however, permeability was measured from 3.25% as maximum permeability was not seen in the 4 – 6% moisture range. A similar approach was followed for the 10% MP mixture where 5.25% moisture was tested in order to determine the peak in permeability. The granulated mixtures were randomly charged into a permeameter (Figure 18) to create a 535 mm bed. A venturi system was then sealed securely on top of the permeameter. The permeameter consists of a 1 mm screen which serves as a support for the bed. The bottom of the permeameter was connected to a suction fan which consisted of a manual valve to control pressure across the bed. Air was drawn across the bed at 1000 mmH_2O suction pressure and pressure was measured in the venturi, above and below the bed. The pressure in the venturi was used to calculate the flow rate (Q) which was then used to calculate permeability from Equation 2. Permeability was reported in JPU.

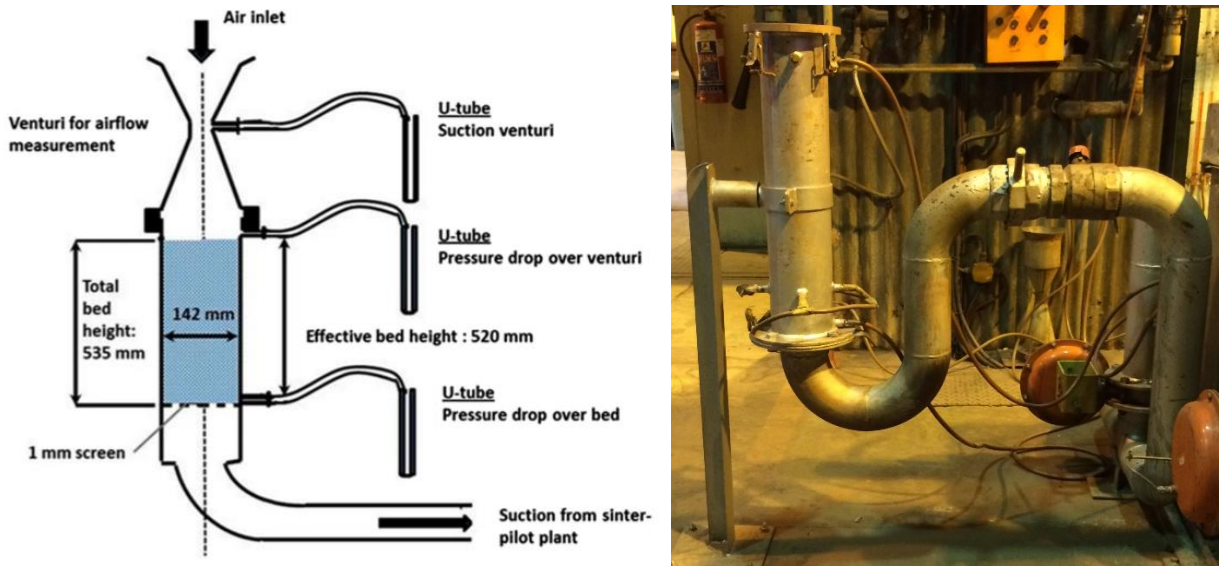

Figure 18: Experimental setup for the measuring of JPU (Nyembwe *et al*,.2016).

$$JPU = \frac{Q}{A}\left(\frac{H}{\Delta P}\right)^{0.6} \qquad \textbf{Equation 2}$$

Where

JPU = Japanese Permeability Unit

Q = air flow rate (m^3/min)

A = cross sectional area (m^2)

H = water level (mm)

ΔP = Pressure drop across the bed (mmH_2O)

© University of Pretoria

Grain size distribution (GSD) was measured using the wet granulated sample from the permeability tests. For each sample, a wet subsample of 1 kg was randomly collected from the granulated mixture for GSD measurement. The screen sizes used for the analysis were 4, 2, 1 and 0,5 mm respectively and only mixtures with optimum moisture (maximum permeability) were analysed. The results from the GSD were used to calculate the mean sizes of the granules (D), material transfer (S) and fines elimination efficiency (E_x) using the following equations:

$$\boldsymbol{D} = \frac{\mathbf{100}}{(\sum \frac{x_i}{d_i})} \qquad \textbf{Equation 3}$$

$$\boldsymbol{S} = (\% < \boldsymbol{X\ mm})_{\boldsymbol{BG}} - (\% < \boldsymbol{X\ mm})_{\boldsymbol{AG}} \qquad \textbf{Equation 4}$$

$$\boldsymbol{E_X} = \mathbf{100} * \frac{\boldsymbol{S}}{\boldsymbol{S'}} \qquad \textbf{Equation 5}$$

Where

D = mean granule size (mm)

x_i = mass % of granules of size fraction d_i

d_i = screen aperture (mm), mean granule diameter of size fraction i

S = material transfer (%)

S' = $(\% < X\ mm)_{BG}$

E_x = material transfer efficiency (%)

$(\% < X\ mm)_{BG}$ = mass fraction less than X mm before granulation

$(\% < X\ mm)_{AG}$ = mass fraction less than X mm after granulation

X = screen size at which there is neither loss nor gain (mm)

© University of Pretoria

3.3 Sinter production

The sintering process was conducted on a pilot scale set up similar to that shown in Figure 19. In this study, the samples with optimized moisture content for maximum permeability were chosen for sinter pot testing.

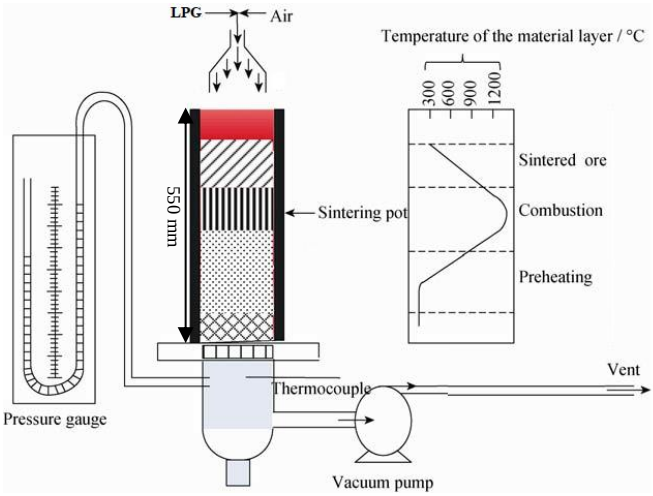

Figure 19: Sinter pot test schematic (Chen *et al.*, 2011).

The sinter pot test was carried out twice for every sinter mixture and the average of the properties was taken. Raw materials were fed into a mixing drum according to their respective ratios as shown in Table 1. The raw materials were then mixed for 1 minute without moisture and 1 minute with moisture. After mixing the material was transferred into a granulation drum of 500 mm diameter and 1000 mm height and granulated for 2 minutes after which it was discharged onto a conveyor belt which fed the granulated mixture into the sinter pot. A round sinter pot was used in this study due to its small capacity of 80 kg, internal diameter of 320 mm and 550 mm in height. The pot consisted of a grid layer which was made up of +16 mm sinter material, 50 mm in height; the granulated bed was therefore 500 mm in height (Figure 19).

The sintering process was initiated by igniting the surface of the bed to 1050 °C at a 500 mmH_2O pressure for approximately 60 seconds after which the sintering pressure was set to 1000 mmH_2O. When the thermocouple at the bottom of the bed reported the maximum temperature, the sintering process was stopped as this suggested that the flame front has passed through the bed. The sinter cake was then left to cool to 25 °C at 800 mmH_2O, which was followed by crushing, screening, tumbling and metallurgical property testing.

3.3.1 Sinter strength test

Sinter strength was measured following the ISO 3271:2015 test procedure. At the completion of the sintering process, the sinter cake was cooled in the sinter pot and thereafter crushed. The sinter cake was dropped three times, charged into a rotating drum where it was rotated for 80 revolutions and thereafter discharged onto vibrating screens starting from 40 mm to 5 mm and sieved for 3.5 minutes. After the screening process, a 15 kg sample was prepared from the -40 mm to +10 mm sinter fraction for the tumbling drum. This 15 kg sample was

© University of Pretoria

charged into the drum, rotated for 200 revolutions, followed by screening with screens having the following aperture sizes; 10mm, 6.3 mm and 0.5 mm. The mass fractions were used to calculate the Tumble Index according to Equation 6.

$$\boldsymbol{TI = \left(\frac{m_1}{m_0}\right) * 100} \qquad \textbf{Equation 6}$$

Where;

m_o = mass of the sample weighed and placed in the drum in kg

m_1 = mass of 6.3 mm oversize in kg

3.3.2 Metallurgical properties

The -12.5 mm + 10 mm size fraction of each sinter was split and weighed to 2 kg in preparation of the reduction disintegration (RDI) and reducibility (RI) tests. Each test was carried out twice per sinter composition.

3.3.2.1 RDI test

RDI was determined by performing a static reduction test on the -12.5 mm +10 mm sample at a temperature of 500 ^{o}C in an atmosphere consisting of 20% CO_2, 20% CO, 2% H_2 and 58% N_2 as per ISO 4696-1:2015 standard. After one hour the test sample was cooled to a temperature below 100 ^{o}C and tumbled in a tumbling drum for 300 revolutions at 25 rpm. The sample was then screened through 6.3, 3.5 and 0.5 mm sieves respectively. Equations 7 to 9 were used to calculate the RDI's for the respective size fractions.

$$\boldsymbol{RDI_{-6.3} = (1 - \left(\frac{m_1}{m_0}\right)) * 100} \qquad \textbf{Equation 7}$$

$$\boldsymbol{RDI_{-3.5} = \left(\frac{m_0 - (m_1 + m_2)}{m_0}\right) * 100} \qquad \textbf{Equation 8}$$

$$\boldsymbol{RDI_{-0.5} = \left(\frac{m_0 - (m_1 + m_2 + m_3)}{m_0}\right) * 100} \qquad \textbf{Equation 9}$$

where:

m_o = mass of sample after reduction before tumbling (in grams)

m_1 = mass of 6.3 mm oversize (in grams)

m_2 = mass of 3.5 mm oversize (in grams)

m_3 = mass of 0.5 mm oversize (in grams).

© University of Pretoria

3.3.2.2 RI test

The -12.5 mm +10 mm sample was also subjected to an isothermal reduction at a fixed temperature of 950 °C under 40% CO and 60% N_2 atmosphere as per ISO 4696:2015 standard. The final mass after reduction was measured against the initial mass and Equation 10 was used to calculate the Reducibility Index.

$$\boldsymbol{RI}(\%/\boldsymbol{min}) = \left(\frac{\boldsymbol{m_0 - m_1}}{\boldsymbol{m_0 * \Delta t}}\right) * \boldsymbol{100} \qquad \textbf{Equation 10}$$

m_o = initial sample mass (g)

m_1 = final sample mass (g)

Δt = reduction time (min)

3.4 Micro-Focus X-ray Micro-Tomography (MF-XRT)

Micro-XRT was conducted on the granulated particles to observe the number of adhering fines attaching to the nuclei as the different quantities of concentrate and micropellets were added to the raw material mixture. It was also conducted on the micropellets after granulation to observe whether they maintain their integrity after sintering. The sinter particles (-25 +16 mm) were also analyzed through micro-XRT to observe the structure of the micropellets in the produced sinter.

The tests were conducted using the Nikon XT H 225L system at the Nuclear Energy Corporation of South Africa. The lead lined cabinet is fitted with an X-ray source, rotating stage, a scintillator screen and a CCD (charge-coupled-device). During the scan, X-rays transmitted from the rotating sample hit the scintillator screen which converts the X-ray pattern into visible light images which are then projected on to the CCD. Due to the rotating nature of the stage during the scan, multiple 2D images were formed and were stacked together using CT Pro 3D software to reconstruct a 3D structure. The 3D structures were then analyzed using VG-Studio 3.2 for granulation mechanisms, integrity of the micropellets and sinter morphology.

Figure 20: Nikon XTH 225L assembly used MF-XRT at NECSA MIXRAD facility (Hoffman and De Beer, 2012).

© University of Pretoria

3.5 Mineralogical Analysis

Mineralogical studies were conducted on crushed sinter samples from the -40 mm + 10 mm size fraction which were previously used for tumble index testing. The material was crushed to -2 mm, split and respective samples were collected for different micro analytical tests. The -12.5 mm + 10 mm size fraction used for metallurgical testing was also collected for SEM-EDS analysis

3.5.1 X-ray Fluorescence Spectrometry

X-ray fluorescence spectrometry utilizes the concept of transitioning electrons from different energy states. The classical atomic model described by Neils Bohr is shown in Figure 21, where the innermost shell is the K-shell, which is followed by the L-shell consisting of three sub-shells. The M-shell, which is the outermost shell, consists of 5 sub-shells (Figure 21). The analysis for elements in iron ore sinter by X-ray fluorescence is enabled by the behavior of atoms when they interact with radiation. When materials are excited with high-energy, short wavelength radiation such as X-rays, they can become ionized. If the radiation energy is sufficient to dislodge a tightly held inner electron (in the K-orbital), the atom becomes unstable and gets expelled from the inner shell (Brouwer, 2010). An electron from the outer shell then replaces the missing electron. When this happens, energy is released as a result of the decreased binding energy of the electron in the inner orbital compared with an outer one. Energy of the emitted photon is lower than that of the incoming X-ray and is known as the characteristic X-ray. Since the energy of the emitted X-ray is specific to a transition between specific electron orbitals in every element, X-ray fluorescence can be used to detect quantities of elements in a sample (Fitton, 1997).

In X-ray fluorescence spectrometry, an X-ray tube is used to irradiate the chemical elements in the sample, causing them to release energy as a result of the transition of electrons to lower, vacant energy states. The released energies are then captured using a detector which provides the information onto a computer (Figure 22). In this study samples were taken from the – 40 mm + 10 mm size fractions and pulverized for XRF analysis. The pulverized samples were submitted to UIS Analytical Services which utilized the Thermo Scientific ARL Advant'X Pro instrument.

© University of Pretoria

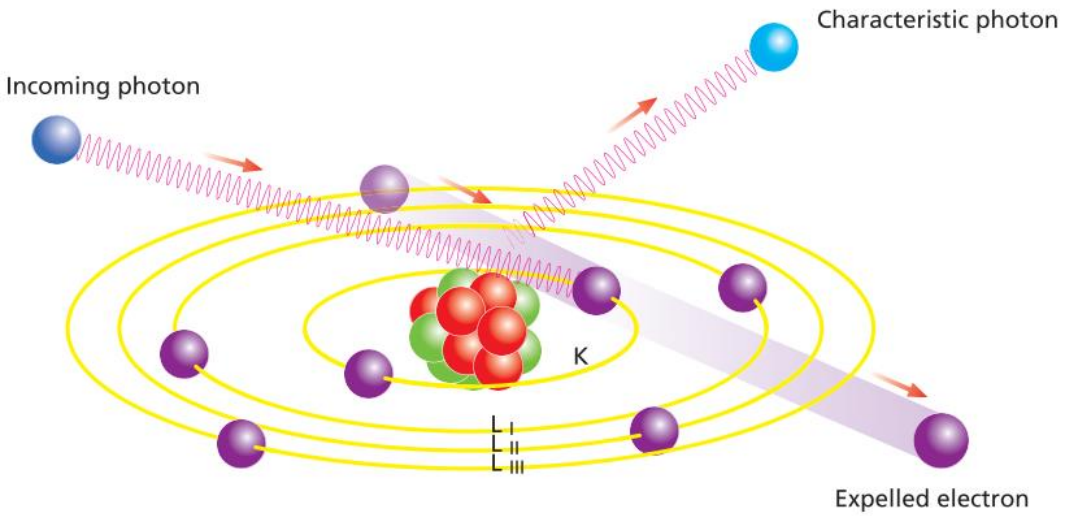

Figure 21: Bohr's atomic model showing different energy states of an atom (Brouwer, 2010).

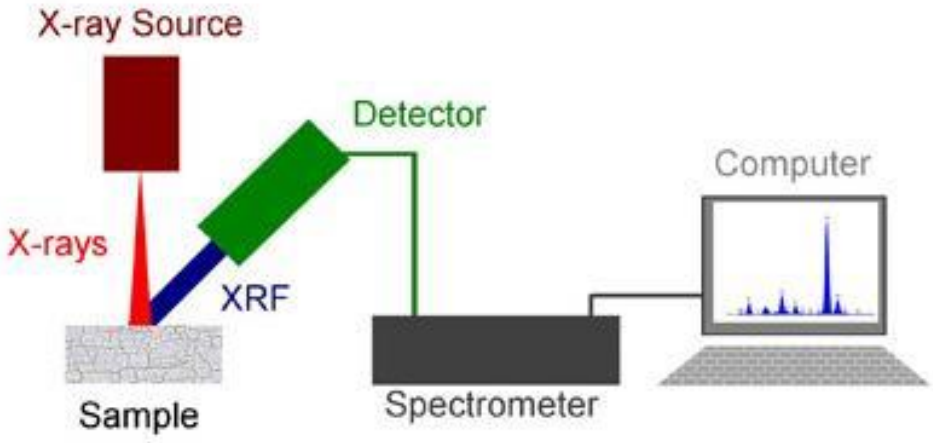

Figure 22: Operating principle of an XRF spectrometer (Garba *et al.*, 2013).

3.5.2 X-ray Diffraction

X-ray powder diffraction (XRD) is an analytical technique used primarily for the identification of crystalline phases in a sample and can also provide information on unit cell dimensions. The analysis is normally carried out on milled samples (-10 μm) in order to achieve random crystallographic orientations (Bish and Post, 1989). It is based on using a monochromatic beam of X-rays to radiate a sample with an X-ray source and a detector making variable angles on a typically flat sample. The interaction of the incident rays with the sample produces constructive interference (and a diffracted ray) when conditions satisfy Bragg's Law (Equation 11). Figure shows a schematic diagram of the most common setup used in modern XRD machines (named Bragg-Brentano geometry). The X-ray beam from the X-ray source (cathode ray tube) is directed onto a flat sample while both the source and detector rotate towards 90°. The machine consists of a set of slits to keep the beams focused on the sample. The detector records and processes the X-ray signal and converts it to a count rate which is then

© University of Pretoria

fed to a computer monitor. Results of X-ray diffraction analysis show peaks as a function of diffraction angles (called diffraction patterns) typically ranging from 5° to 75° (Lu, 2015). The value of d in Equation 11 is unique for most crystalline minerals and phases, as it represents the spacing between parallel planes in a crystal (Figure 24).

$$n\lambda = 2dsin\theta$$ **Equation 11**

Where

n = integer

λ = wavelength of the X-ray source

d = spacing between the planes in the atomic lattice

θ = angle between the X-ray source and the crystalline planes (see Figure 25)

The instrument used in this study was a PANalytical X'Pert Pro diffractometer fitted with an X'Celerator detector and CuK_{α} radiation with a Fe filter located at the Geology Department, University of Pretoria. Rietveld refinement was carried out using Autoquan software for quantitative analyses of the sinter phases. For qualitative analysis, Highscore software was used.

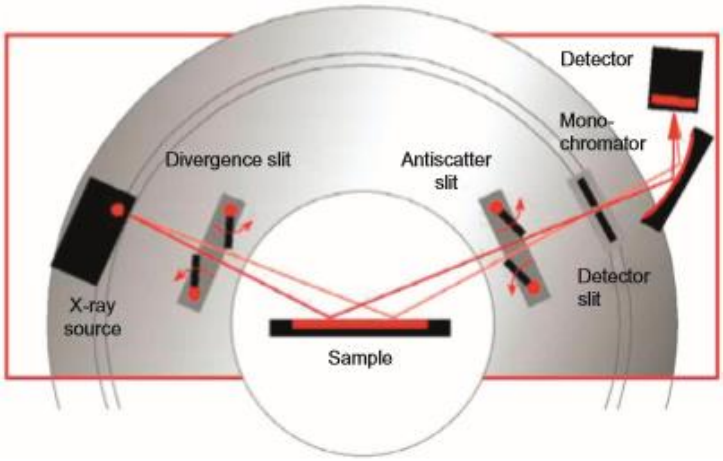

Figure 23: Basic operation of an XRD instrument (Lu, 2015).

© University of Pretoria

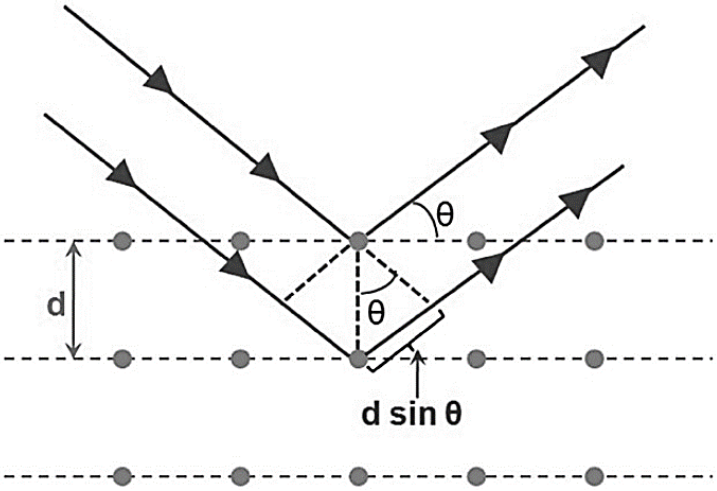

Figure 24: Diffraction of a monochromatic x-ray beam by a single crystal.

3.5.3 Scanning Electron Microscope Analysis

A scanning electron microscope was used to study the microstructures and phase compositions of the produced sinters. This microscope utilizes a beam of high energy electrons to form an image. When the surface of the sample and electrons interact, they give rise to a variety of signals from which the morphology, chemical composition and crystal structure can be observed. The types of signals obtained from the interaction of the sample surface and the beam of electrons include secondary electrons (SE), backscattered electrons (BSE) and characteristic X-rays (Sharma *et al.*, 2018).

Samples collected from the -12.5 + 10 mm size fraction (also used for RI and RDI tests) were sampled for analysis through SEM and optical microscopy. The samples were also crushed to -2 mm in order to ensure that the analysis is representative. The crushed particles were resin mounted, polished and gold coated for SEM and reflected light microscope analysis. SEM analysis was conducted at the Industrial Minerals and Metals Research Institute (IMMRI) at the University of Pretoria using a JEOL JSM – IT300 InterScope instrument (Figure 25). Energy dispersive spectrometry (EDS) was used to determine the chemical compositions of the phases in the sinter.

© University of Pretoria

Figure 25: Scanning electron microscope at the IMMRI, University of Pretoria.

© University of Pretoria

Chapter 4
Results

4.1 Granulation

Granulation is an important part of sinter mix preparation. The important parameters considered during this process were moisture content and granule size distribution. This is because both moisture and granule size distribution play an important role in the strength of quasi-particles and permeability of the bed respectively.

4.1.1 Correlation between moisture addition and permeability

The moisture - permeability relationships investigated in this study are reported in Figure 26. Three permeability measurements were taken for every mixture of specific moisture content and the plot in Figure 26 represents the averages. The moisture levels were varied from 4% to 6% in 0.5% increments, except for the base case mixture where the moisture level was varied between 2.5 and 6%.

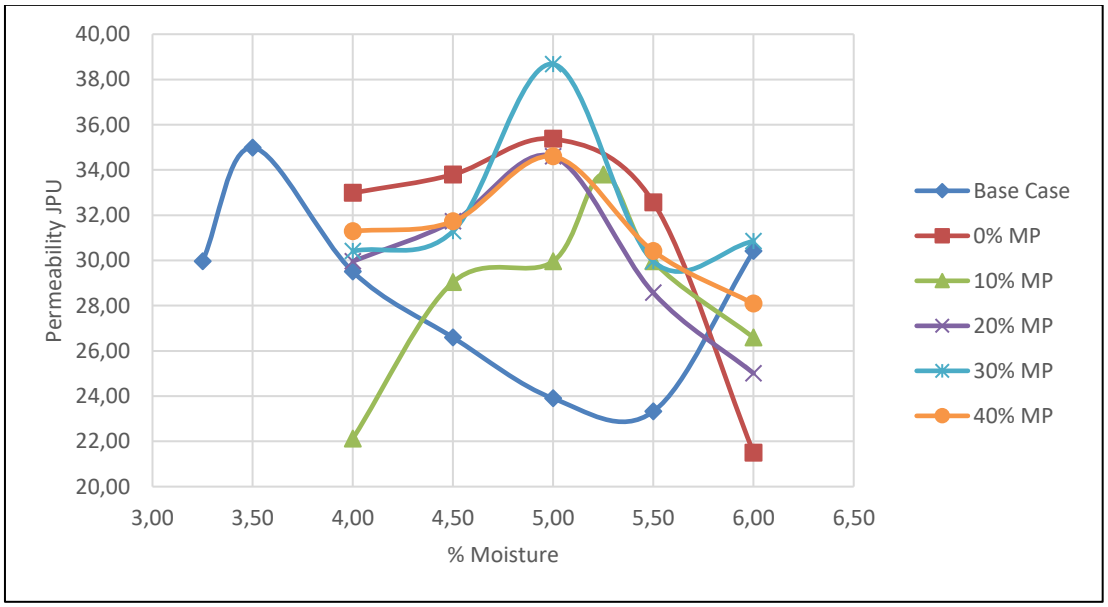

Figure 26: The effect of moisture on permeability of mixtures containing micropellets and concentrate (Data based on three permeability tests).

Permeability increased for all sinter mixtures with increasing moisture content until a certain percentage after which further addition caused a decrease in permeability (Figure 27). Most of the sinter mixtures reached their maximum permeability at 5% moisture with exceptions being the base case as well as the mixture containing 10% MP. The maximum permeabilities of both base case and the 10% MP sample were found at 3.50% and 5.25% respectively. The maximum permeability as a function of sinter mixture is plotted in Figure 27. According to this figure, increasing micropellet content while reducing the concentrate content leads to an increase in maximum bed permeability. The 30% MP mixture showed superior permeability with the pure mixtures, as well

© University of Pretoria

as the base case mixture showing rather low permeability values. The absence of error bars for some of the data points (e.g. base case sample) was due to little variability in the data.

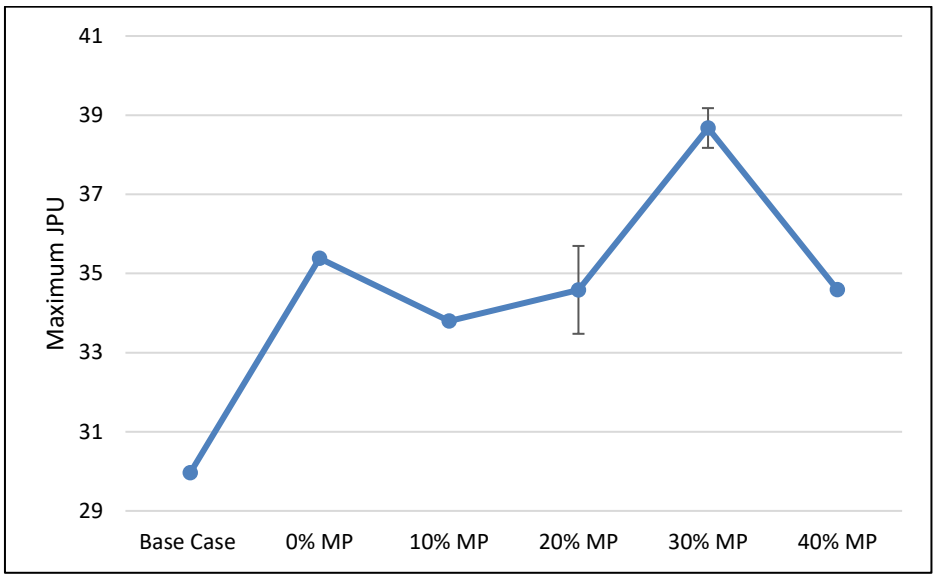

Figure 27: Maximum permeability as a function of micropellets to concentrate ratio.

There seems to be an increase in maximum permeability when the ratio of micropellets to concentrate was increased from 10% MP to 30% MP as seen in Figure 27. The 0% MP mixture shows the second highest permeability after the 30% MP mixture which is also higher than the mixture containing 40% MP. Nyembwe *et al.*, (2016a) compared the maximum permeability values of 0% MP and 40% MP mixtures and found that of the 40% MP to be higher. In this study however, with micropellets prepared from corn starch and Acronal (compared to those prepared with bentonite as in the case of Nyembwe *et al.*, (2016a)) the reverse effect was observed where the maximum permeability of the 40% MP mixture is slightly lower than that of the 0% MP mixture. This was presumably due to the large spherical particles formed from the concentrate during granulation. The relatively large granules shown in Figure 28(left) were due to the increased coalescence and contributed to the slightly higher permeability in the 0% MP mixture.

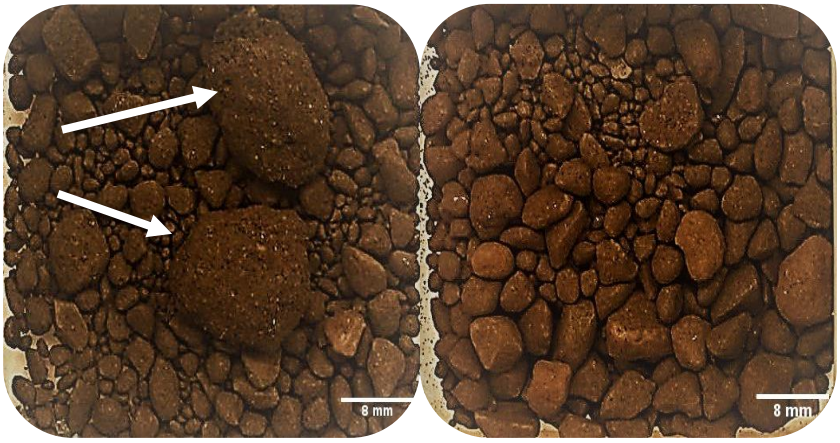

Figure 28: Granules for mixtures containing (left) 40% concentrate and (right) 40% micropellets.

© University of Pretoria

4.1.2 Granule Size Distribution

The general aim of granulation is to produce a narrow coarse size distribution in order to optimize airflow across the sinter bed. The coarsening of the sinter mixtures can be seen from Table 5 by comparing the size distributions before and after granulation. It can also be seen that mixtures containing high amounts of concentrate show a high amount of fines transfer across the size fractions.

Table 5: Particle size distribution of the mixtures before and after granulation.

	0% MP		10% MP		20% MP		30% MP		40% MP	
Size (mm)	Mass % (BG)	Mass % (AG)	Mass % (BG)	Mass % (AG)	Mass % (BG)	Mass % (AG)	Mass % (BG)	Mass % (AG)	Mass % (BG)	Mass % (AG)
4	19,29	34,71	21,97	39,12	24,67	32,15	27,36	38,37	30,04	31,62
2	21,95	39,2	25,14	44,13	31,53	40,87	31,53	38,59	34,73	39,48
1	12,96	21,35	13,83	14,73	14,7	20,92	15,58	18,62	16,45	20,73
0,5	4,86	4,62	4,86	1,95	4,86	5,95	4,86	4,13	4,86	7,12
0,35	40,95	0,12	33,6	0,07	26,22	0,1	18,86	0,28	11,51	1,05

BG = Before granulation
AG = After granulation

The mean granule sizes of the mixtures before and after granulation are shown in Figure 29. The 10% MP sample had the highest mean granule size after granulation. The increase in the micropellet content while decreasing the amount of concentrate led to a decrease in mean granule size. The mean granule size of the mixture that contained concentrate only was relatively lower, which suggests that the mixture was dominated by finer granules instead of the large lumps presented in Figure 28. The mean granule size of the 40% MP mixture was also low mainly due to a lack of adhering fines present in the mixture during granulation.

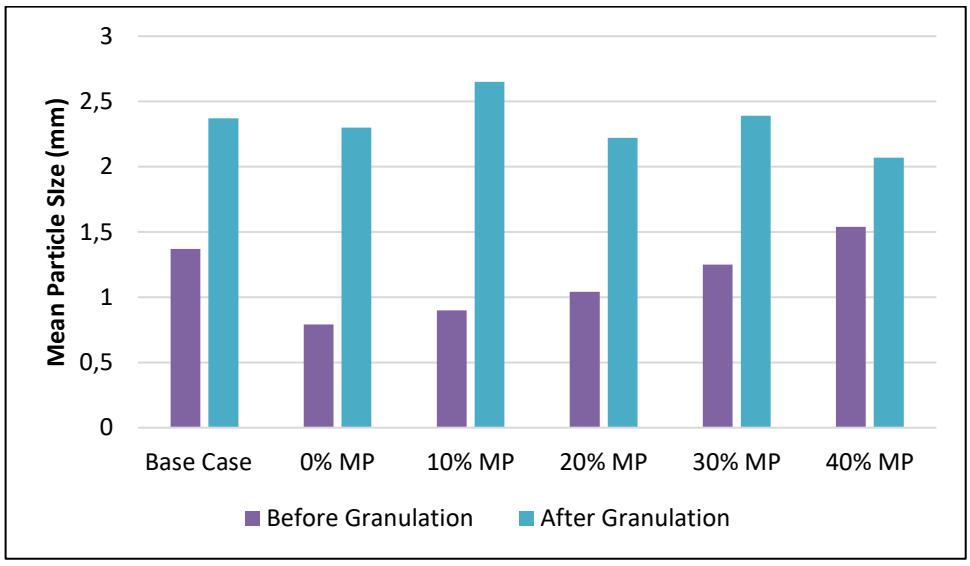

Figure 29: Mean granule size before (D(BG)) and after (D(AG)) granulation as a function of micropellet and concentrate addition.

© University of Pretoria

Material transfer curves for the different sinter mixtures are shown in Figure 30. These curves were plotted by calculating the difference in the mass fractions of the respective mixture before and after granulation with calculations shown in appendix A.1 Granulation Data. It can be seen that there was extensive transfer in material from the fines (-0.5 mm) fraction with over 40% loss of fines for the mixture containing 0% MP. The 10% MP coarse fraction shows the highest material gains followed closely by the 0% MP mixture. These gains can be attributed to the high amount of fine material available for granulation. The 40% MP reported the least gains especially on the highest size fraction of +4 mm which can also explain the low mean granule size shown in Figure 29. The 30% MP maintained a higher material gain for the largest size class despite having fewer fines than the 20% MP mixture.

Material transfer plotted in mass percentage as a function of the micropellet to concentrate ratio was calculated according to Equation 4 and is shown in Figure 31. It can be seen that an increase in micropellet content while reducing the concentrate content led to a decrease in material transfer.

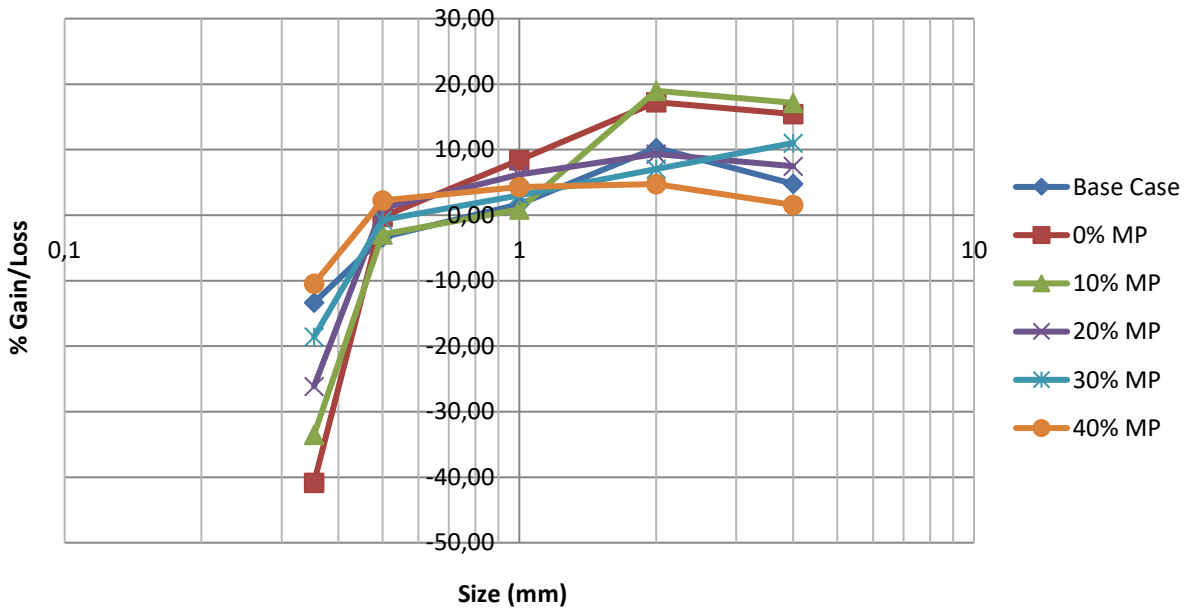

Figure 30: Material gain/loss as a function of size class for the different sinter mixtures.

© University of Pretoria

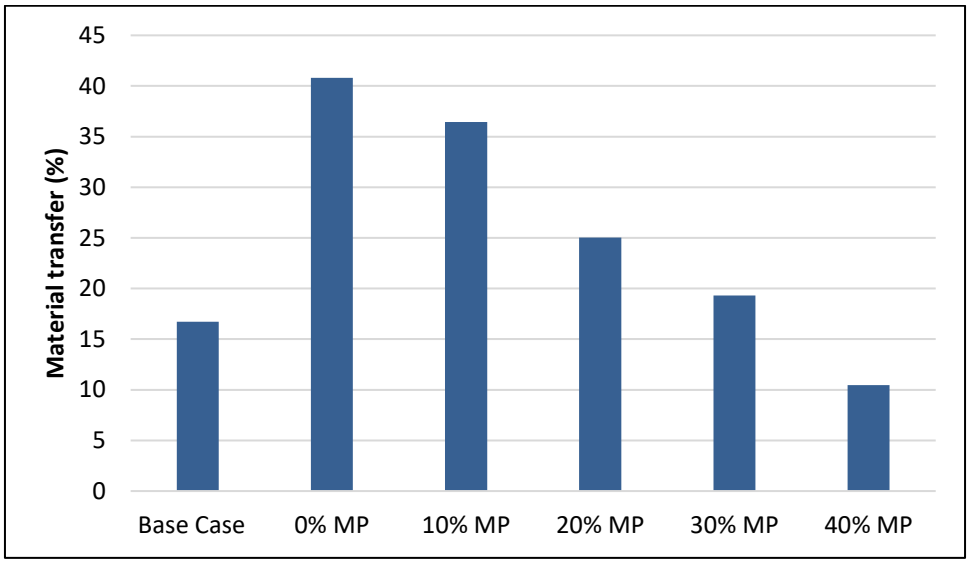

Figure 31: Material transfer (S) as a function of micropellet to concentrate ratio.

4.1.3 Quasi-particle properties

The role of micropellets in sinter mixtures is to not only act as large seed particles for granulation, but their shape and surface texture is also important. X-ray micro-tomography was conducted on the granulated material with the intention of determining the layering mechanisms involved during granulation. Nyembwe *et al.*, (2016a) classified the layering mechanisms using mixtures that only contained either micropellets or concentrate. In this study however the mixtures contained both concentrate and micropellets.

The layering mechanisms observed for the sinter mixtures with varying amounts of micropellets and concentrate are shown in Figure 32 - 38. Auto layering (group I) is a common layering mechanism in most of these mixtures. This is mainly due to the presence of nuclei particles and adhering fines other than micropellets and the concentrate. Auto layering is normally the main layering mechanism in most granulation scenarios. As expected, it was the primary layering mechanism in the base case as shown in Figure 32.

© University of Pretoria

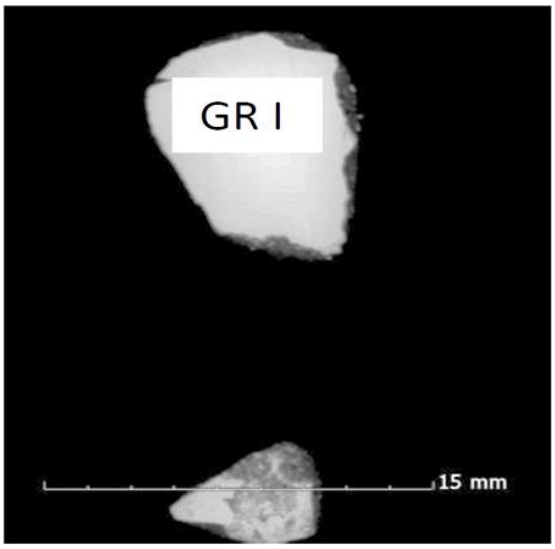

Figure 32: Base Case MF-XRT micrograph showing a group I layering mechanism.

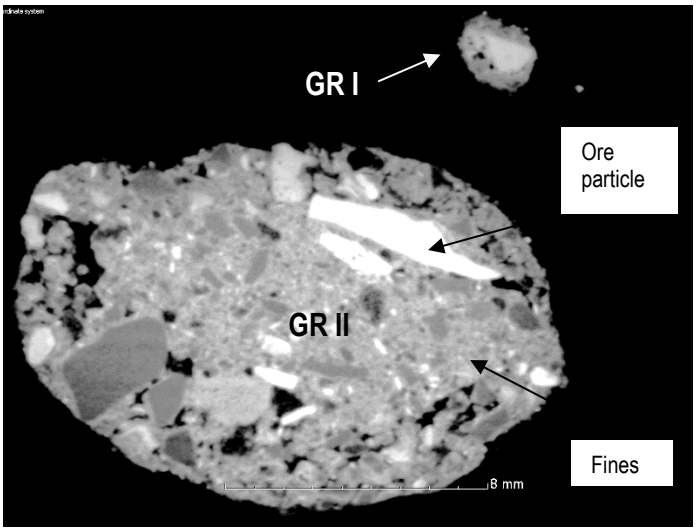

Figure 33: 0% MP MF-XRT micrograph showing a combination of group I and II layering mechanisms.

Group I and II layering mechanisms can be observed from Figure 33. The group I layering mechanism is typical of that classified by Nyembwe *et al.*, (2017) as the angular shaped nuclei provide surfaces of attachment for the adhering fines. As previously shown in Figure 28, the formation of the lumpy granules is mainly a result of group II layering of excess amounts of fines. During granulation, the lack of coarse particles has led to a pelletization phenomenon where some of the fines coagulated to form spherical lumps. According to Table 5, the amount of -0.5 mm particles was significant enough to allow for such phenomena to take place. The group II mechanism (Figure 33) also shows that during the pelletization process, other coarse particles could also be coalesced by the fine material.

© University of Pretoria

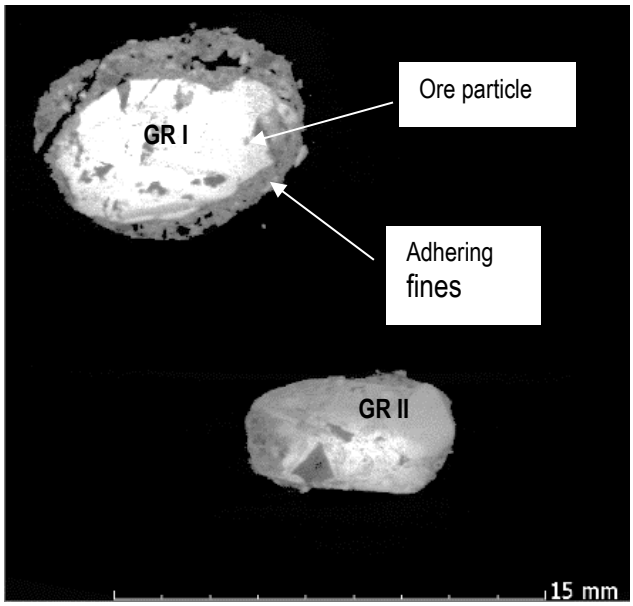

Figure 34: 10% MP MF-XRT micrograph showing group I and II layering mechanism.

Layering mechanisms observed when 10% micropellets were introduced and the amounts of concentrate decreased to 30% are shown in Figure 34. Based on the high material transfer of the 10% MP mixture in Figure 30, it can be argued to that the coalescence mechanism (Group II) was also present during granulation. Figure 35 (10% MP) shows a granule similar to that shown in Figure 28 for the 0% MP mixture, the formation of this lumpy granule was attributed to the pelletization effect associated with the group II mechanism. The lumpy granule also appeared to be smaller in this mixture as a result of the reduction in the quantity of the concentrate.

Figure 35: Granules from the mixture containing 10% micropellets and 30% concentrate.

When the micropellet content was increased to 20% and the concentrate decreased to 20%, the amount of available adhering fines was reduced. This can be seen from the group I mechanism in Figure 36 where the adhering layer appears thinner than the previously shown group I mechanisms.

© University of Pretoria

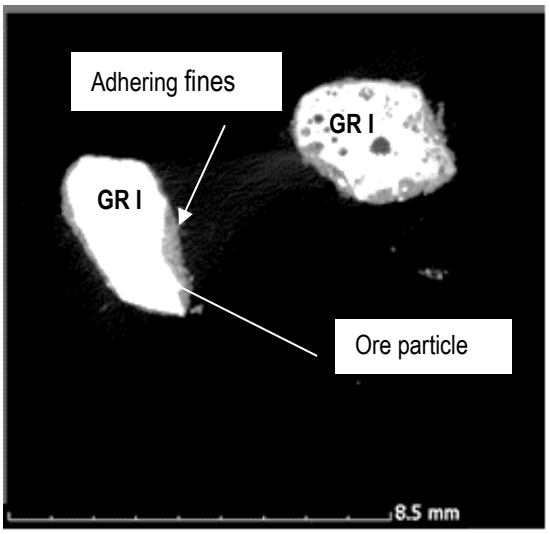

Figure 36: 20% MP MF-XRT micrograph showing group I layering mechanism.

The group I mechanism in Figure 37 (30% MP) is similar to that shown in Figure 36 with the thin layer of adhering fines around the coarse nuclei. In this case, the quantity of micropellets was increased to 30% and concentrate was decreased to 10%. The spherical nature of the micropellet in Figure 37 can be closely associated with the group II mechanism; this is mainly because the group II layering mechanism gives rise to pellets from fines without the use of coarse nuclei.

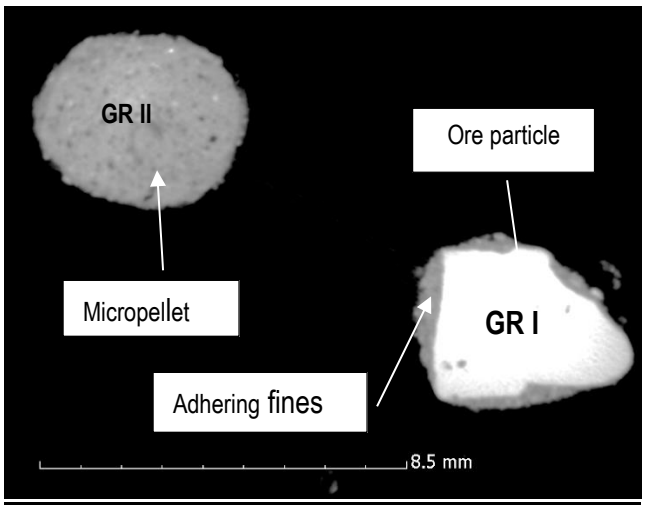

Figure 37: 30% MP MF-XRT micrograph showing group I and II layering mechanism.

When the concentrate was completely replaced with micropellets (40% MP) group III layering emerged (Figure 38). This mechanism is described as the adhesion of micropellets, which presumably have been facilitated by the presence of a large quantity of micropellets and some fines. Although the 40% MP mixture contained the lowest amounts of adhering fines; the granule formed by the adhesion of micropellets is covered by some adhering fines. It can also be seen from Figure 38 that the contact between the micropellets is not through cementation by adhering fines.

© University of Pretoria

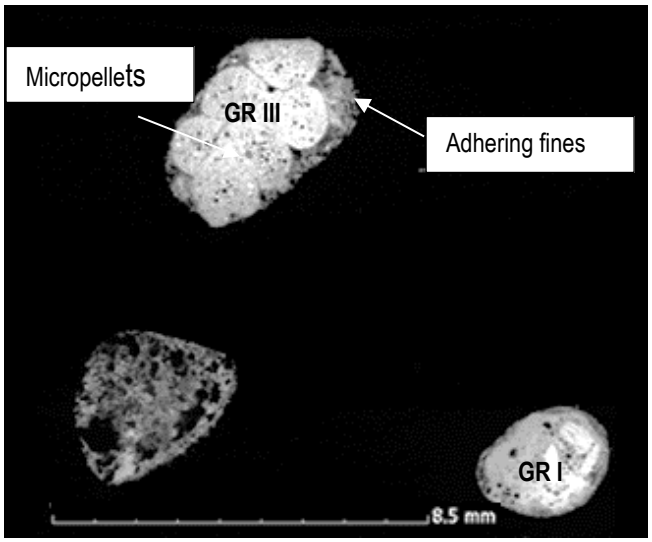

Figure 38: 40% MP MF-XRT micrographs showing group I and group III.

4.1.4 Role of Micropellets during granulation

MF-XRT was also conducted individually on the micropellets in order to understand the external and internal changes during granulation. The internal structure of micropellets before granulation consists of cracks and porosity whilst they appear smooth and highly spherical externally (Figure 39). Such particles have been reported to not granulate well due to their low roughness and insufficient points of contact (Lu and Ishiyama, 2016; Nyembwe *et al.*, 2016a). Micropellets from the granulated mixture containing 30% MP were sampled in order to observe the internal and external structure of the micropellets after granulation. Some micropellets disintegrated during granulation as shown in Figure 40, however some maintained their shape. The micropellets disintegrated into smaller lumps and not into the fine concentrate from which it was formed. Although the micropellets proved to be relatively tough prior to granulation, they softened significantly during granulation as a result of the addition of water and may break due to forces imposed by the bed. The micropellet that remained intact during granulation seems to have picked up fines relatively well in what can be argued to be auto layering (Figure 40).

© University of Pretoria

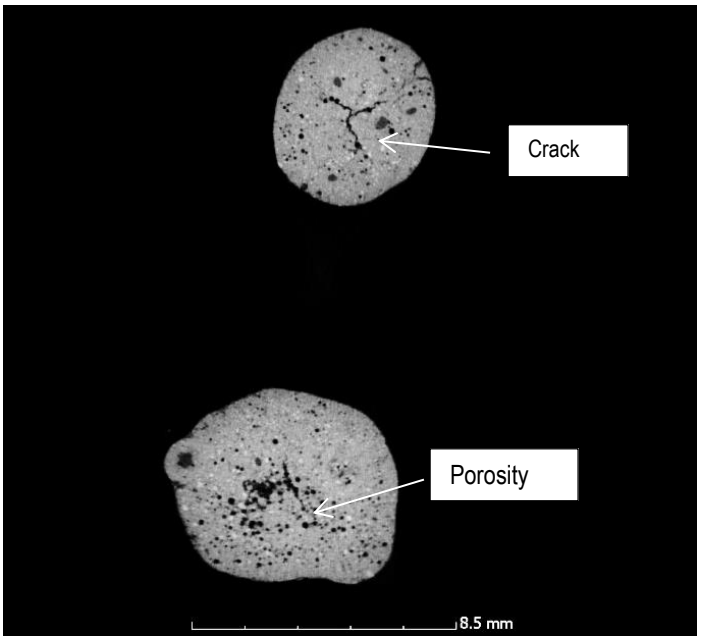

Figure 39: Tomogram of dry micropellets before granulation showing internal cracks and fine pores.

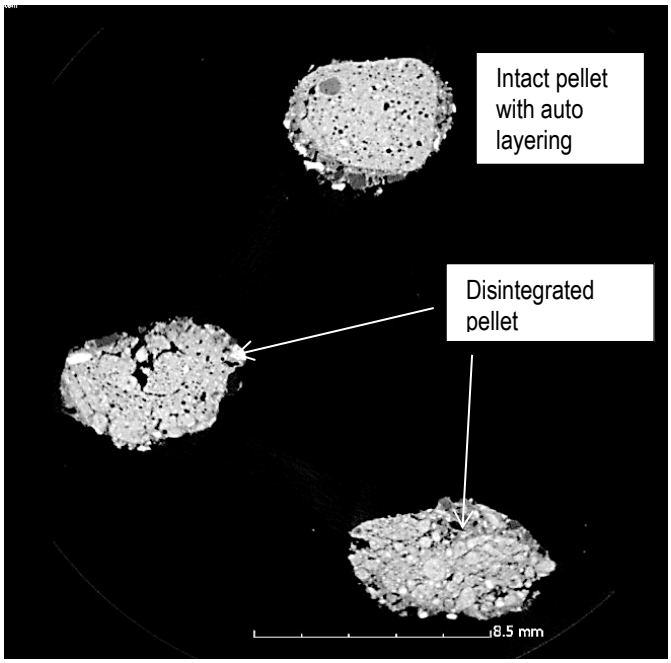

Figure 40: Tomogram of wet micropellets after granulation with some disintegration (30% MP sample).

The 30% MP mixture was also observed through MF – XRT to analyse the interaction of micropellets with the other raw materials. The mixture was collected off the granulation drum by means of a narrow tube of about 15 mm. The 3D structure that was reconstructed for the mixture is shown in Figure 41 and the three cross sections in different planes are shown in Figure 41.

© University of Pretoria

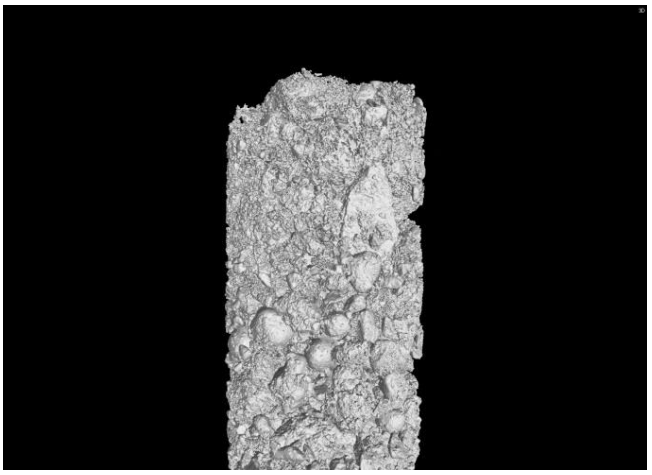

Figure 41: 3D image of the 'simulated' sinter bed.

Segregation of micropellets can be seen from all planes in Figure 42, which is primarily due to the inability of micropellets to attach adhering fines during granulation. This could however have a positive effect on the mixture because it can allow formation of voids which would improve permeability. Two stage layering can also be seen from Figure 42 where the elliptical micropellet is attached to the ore particle through a layering of micro-fines. The deformed micropellets therefore seem to participate more in granulation through layering of fines, than the unaffected spherical micropellets.

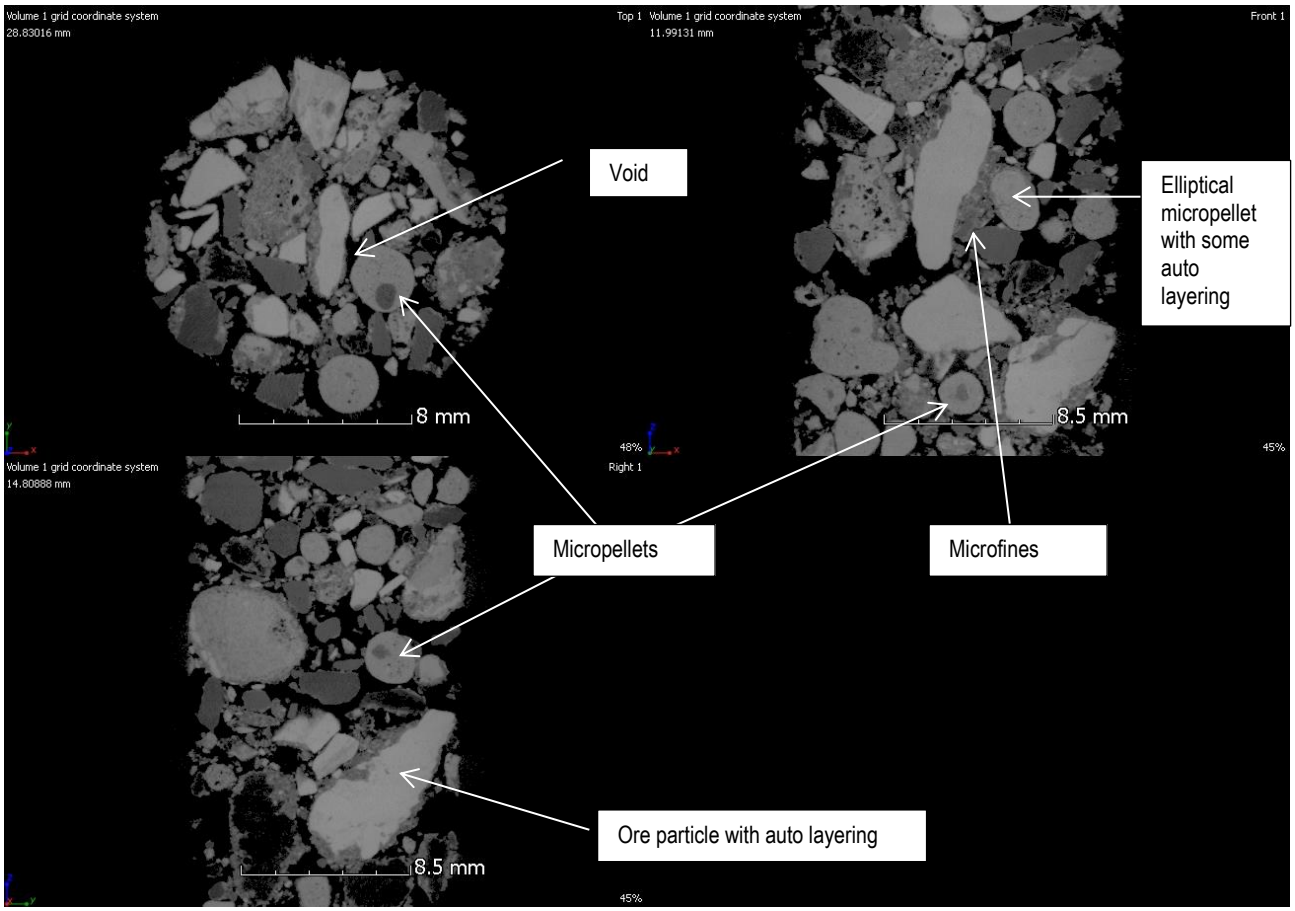

Figure 42: Isometric view of the 'simulated' granulated sinter mixture showing the relative positions of the micropellets.

© University of Pretoria

4.1.5 Summary and discussion of granulation results

A summary of the granulation results is tabulated in Table 6. From the table it can be observed that the material transfer efficiency (E_x) was relatively high for most of the mixtures (>90%), except for the BC and 30% MP samples. The low transfer efficiency for the 30% MP mixture is mainly due to insufficient amounts of adhering fines to facilitate attachment. It is however peculiar that the granulation efficiency of the 40% MP is higher than that of the 30% MP although there was no concentrate added into the mixture. This was presumably due to more water taken up by the micropellets leading to them becoming more deformed. This could have resulted in some picking up of adhering fines. Although there was more transference of material from the fine to the coarser size class, the amount of concentrate in the 30% MP mixture was not sufficient to maintain strong quasi-particles.

Table 6: Granulation potentials of different mixtures containing micropellets and concentrate.

	Max JPU	Moisture* (%)	X (mm)	S (%)	Ex (%)	D (B.G)	D (A.G)
BC	30.00	3.5	0.85	16.72	81.2	1.37	2.37
0% MP	35.37	5.0	0,5	40,82	99,68	0,79	2,3
10% MP	33.80	5.25	0,85	36,44	94,77	0,9	2,65
20% MP	34.59	5.0	0,5	25,03	95,45	1,04	2,22
30% MP	38.68	5.0	0,55	19,3	81,36	1,25	2,39
40% MP	34.59	5.0	0,45	10,46	90,9	1,54	2,07

*: At maximum permeability

The average granule size is also important to consider: The addition of micropellets into the sinter mixtures has led to an increase in average size prior to granulation. After granulation however, the mixtures containing higher amounts of concentrate (30 and 40%) showed superior granule growth with relatively higher average granule sizes. It can also be seen from Table 6 that the material transfer efficiencies (E_x) are generally higher for the mixtures containing higher amounts of concentrate as compared to those containing higher micropellet contents.

Permeability is the most important parameter to consider when choosing mixtures for industrial applications. From that standpoint, the mixture containing 30% MP shows the highest permeability compared to the mixtures containing higher amounts of concentrate. It has been reported that for a mixture to have superior granulation potential, it is to have a higher maximum permeability and material transfer efficiency at a lower optimum moisture (Lwamba and Garbers-Craig, 2008; Yang *et al.*, 2018). The 30% MP mixture shows superiority when it comes to maximum permeability however the 0% MP mixture shows superiority from a material transfer efficiency perspective. Generally, the mixtures showed a higher granulation potential (high E_x and JPU) as compared to the base case mixture.

© University of Pretoria

4.2 Chemical Composition

The chemical compositions of the produced sinters are reported in Table 7. Although the basicity (%CaO/%SiO_2) was initially set to 2.2, it varied from 2.10 to 2.44. This is mainly due to the variable amounts of return fines added in each sinter mixture. It can also be seen that although the proportions of micropellets and concentrate were varied, the chemical compositions of the samples remained similar. This is because of the similarity in chemical compositions between the micropellets and concentrate.

Table 7: Sinter chemical composition determined by XRF.

	FeO	Fe_2O_3	SiO_2	Al_2O_3	CaO	MgO	K_2O	MnO	Total	CaO/SiO2
BC	3.5	71.63	6.26	2.12	15.25	3.88	0.29	0.57	100.00	2.44
0% MP	6.22	72.48	6.51	2.32	13.68	4.17	0.35	0.49	100.00	2.10
10% MP	6.57	73.22	6.41	2.12	13.45	3.96	0.35	0.49	100.00	2.10
20% MP	5.77	73.31	6.25	2.13	13.50	3.97	0.34	0.50	100.00	2.16
30% MP	5.69	73.11	6.40	2.21	13.43	4.03	0.33	0.48	100.00	2.10
40% MP	2.71	72.84	6.16	2.11	13.90	4.17	0.32	0.49	100.00	2.26

4.3 Mineralogy of the produced sinters

The results reported in this section were obtained through XRD, SEM and optical microscopy. In the case of observing the internal structure of the sinter particles MF-XRT was used for the analysis.

Major phases determined in this study include hematite, magnetite, silico-ferrites of calcium and aluminum, calcium silicates as well as glass. These phases were determined in various proportions depending on the quantity of micropellets and concentrate that was present. The melt that formed could not be successfully quantified by XRD analysis due to its amorphous nature. It was however chemically analyzed by SEM-EDS. The table of quantitative XRD analysis for the major phases is given in appendix A.2.

4.3.1 XRD analysis

4.3.1.1 Hematite

Most of the hematite found in the sinters was mainly from the hematite ore, the NC fines A and NC fines B, which contained 92% and 94% hematite respectively and the concentrate which contains over 95% hematite. The presence of massive hematite is also due to the coarse nature of some of the ore particles obtained in the respective NC fines. Micropellets can also be a contributor of dense hematite in some mixtures. A massive hematite particle from the 0% MP sinter is shown in Figure 43. The presence of such a particle in the 0% MP mixture is only due to the presence of ore and not of the micropellets.

© University of Pretoria

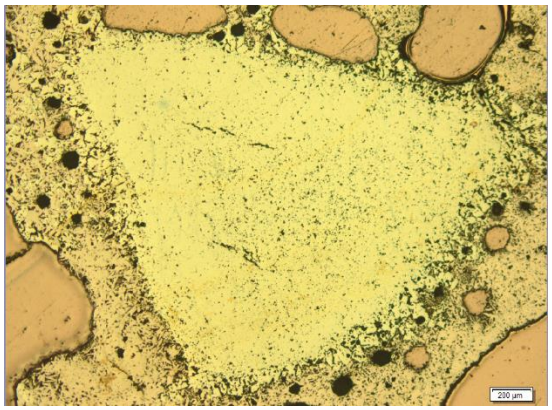

Figure 43: Reflected light micrograph of massive hematite particle from a 0% MP sinter particle.

Not all the hematite in the sinter is the result of the addition of hematite-based raw materials, some hematite may have formed as a result of precipitation and oxidation of magnetite during cooling (Hapugoda *et al.*, 2016).

The amount of hematite in the produced sinters as a function of the concentrate : micropellet ratio is shown in Figure 44. It can be observed that the replacement of the fine concentrate with the coarse micropellet has led to an increase in the amount of hematite. This is mainly due to the reduction in reaction surface as the fine concentrate mixes better with the fluxes in comparison to the micropellets (Fan *et al.*, 2013).

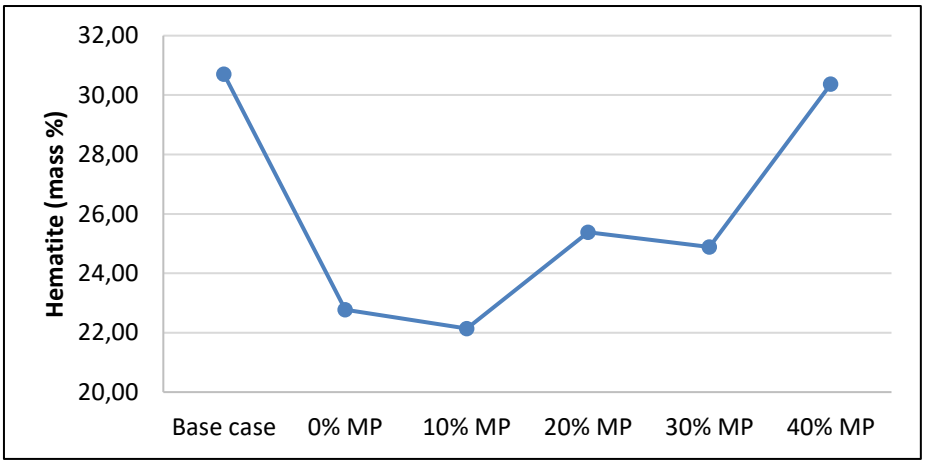

Figure 44: Effect of micropellet to concentrate ratio on the presence of hematite in sinter.

4.3.1.2 Magnetite

Northern cape ores are high hematite containing ores, even the concentrate and micropellets were found to contain at least 95% hematite. The magnetite observed in the sinters therefore was the result of hematite reduction and precipitation from the melt during cooling. The respective proportions of magnetite in the sinters show a nearly opposite relationship to that shown for hematite (Figure 45 vs. Figure 44). The mixture containing 10% MP contains the highest amount of magnetite followed by the 20% MP and 30% MP mixtures. The 40% MP sinter presented the lowest amounts of magnetite of the sinters that contained micropellets and concentrate.

© University of Pretoria

This indicates that the fundamental difference in reactivity between mixtures containing the concentrate and micropellets as the contact between concentrate and coke facilitated the reduction.

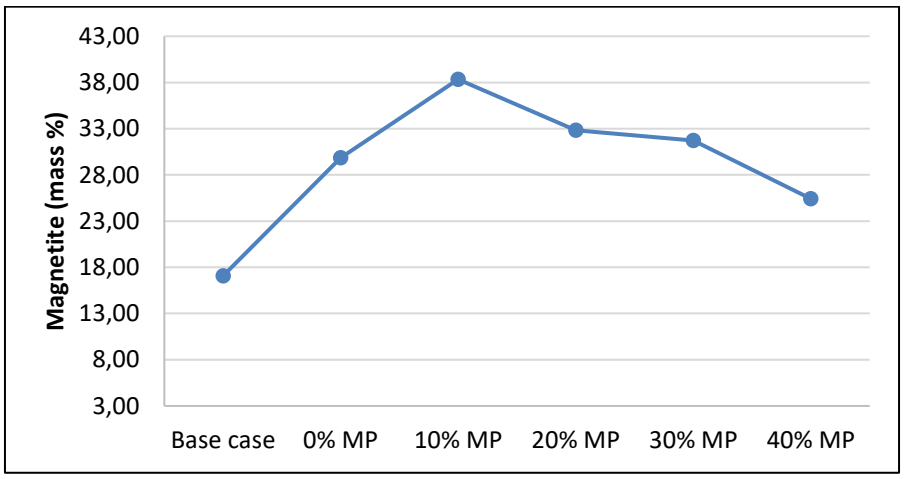

Figure 45: Effect of concentrate to micropellet ratio on the formation of magnetite.

4.3.1.3 Silico-ferrite of calcium and aluminum (SFCA)

The formation of silico-ferrites of calcium and aluminum has been observed as a function of the ratio between micropellets and concentrate (Figures 46 and 47). Industrial sinters typically contain two types of SFCAs namely SFCA and SFCA-I (Webster *et al.*, 2014). The sinters produced in this study also contained these two SFCA phases.

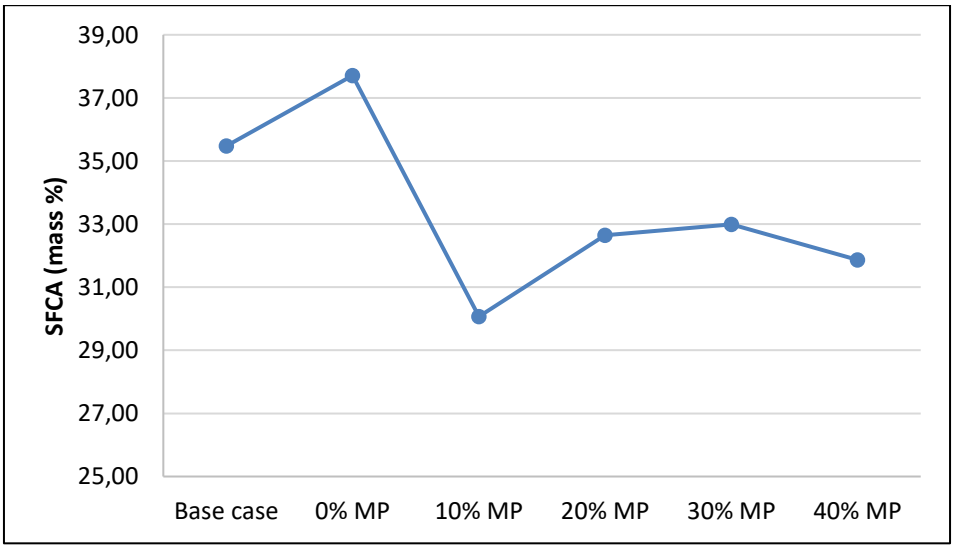

Figure 46: Effect of concentrate to micropellet ratio on the formation of columnar SFCA.

The introduction of micropellets led to a decrease in the percentage of columnar SFCA as opposed to concentrate addition only (Figure 46). The highest amount of columnar SFCA was found in the 0% MP sinter while the 10% MP sinter had the lowest amount, which is however marginally lower than in the sinters containing

© University of Pretoria

more micropellets than concentrate. The base case sinter also showed relatively high amounts of columnar SFCA, but less than that of the 0% MP sample.

An increase can however be seen in the formation of acicular SFCA-I as micropellets replace the concentrate (Figure 47). It has been reported that the formation of acicular SFCA takes place during the heating stage however, most of the acicular SFCA crystallises into columnar SFCA and magnetite during the oxidising conditions of the cooling stages (Webster *et al.*, 2012; Cai *et al.*, 2018). This explains the existence of acicular SFCA in smaller quantities as compared to that of the columnar SFCA.

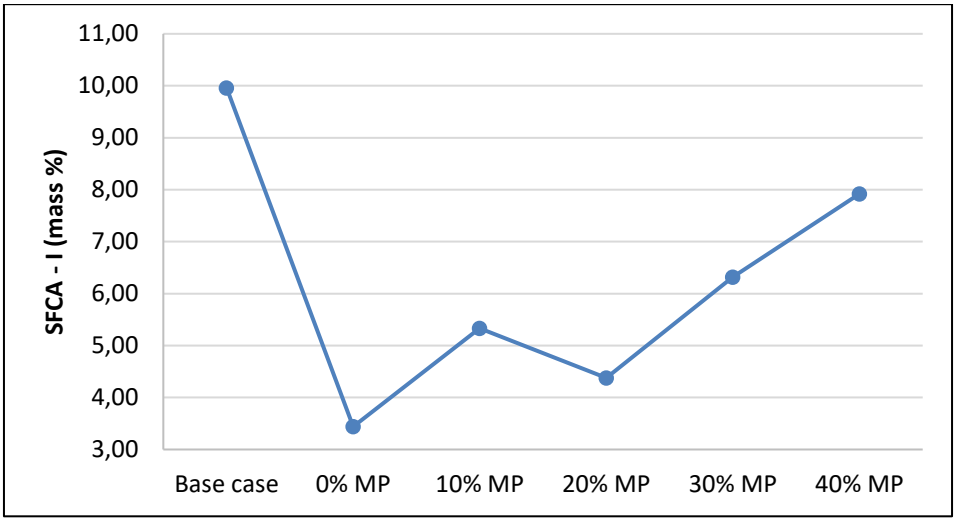

Figure 47: Effect of concentrate and micropellet ratio on the formation of acicular SFCA-I.

In general, SFCA, which is a primary bonding phase in iron ore sinter, formed in relatively large amounts for all the sinters produced. Total SFCA was the predominant phase for each sinter, with the base case sinter reporting the highest total amount of over 45 wt%. The 0% MP sinter had the second highest total amount of 41 wt% which was followed by the mixtures containing high amounts of micropellets (30% and 40% MP) both at just under 40 wt%, with the 10% MP sinter having the lowest total SFCA content of approximately 35 wt%.

4.3.1.4 Larnite

The XRD analysis of the larnite formed in the different sinters is plotted in Figure 48. It can be seen that not a significant quantity of larnite exists in the sinters with the highest amount being that of the base case at 6,78 wt%. Low amounts of larnite are desirable as larnite is reported to have detrimental effects on sinter strength due to its transformation in crystal structure from the β-phase to the γ-phase (Cai *et al.*, 2018). As in the case of acicular SFCA, the amount of larnite decreased significantly with the introduction of micropellets (from 10% MP to 40% MP) suggesting that as the amounts of fines decreased, reaction surface area also decreased as micropellets replaced the concentrate in the mixtures.

© University of Pretoria

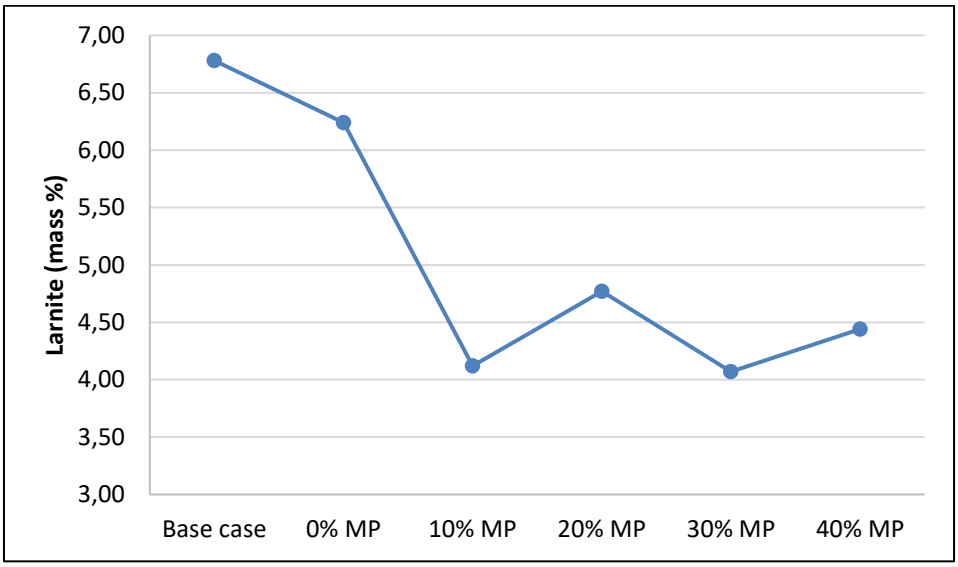

Figure 48: Effect of concentrate to micropellet ratio on the formation of larnite in sinter.

4.3.2 Microstructure

The sinter microstructures were observed using optical microscopy and SEM – EDS analysis.

4.3.2.1 Optical Microscopy

4.3.2.1.1 Base case, 0 – 40% MP sinters

At high temperatures, the mixture of fine material attached to the nuclei particles melts and during cooling different mineral phases crystallizes out of the melt. Sinter quality is strongly dependent on the balance of the mineral phases that form during crystallization. The respective microstructures of the different sinters investigated are shown in Figure 49 - 54. The attachment between the relict particle and bonding phase in the base case sinter is shown in Figure 49a. It can be seen that the structure of the bonding phase along the relict particle consists mainly of SFCA and SFCA-I. The bonding phase structure, which shows a distribution of hematite particles and magnetite crystals suspended in a matrix comprising of a mixture of columnar and acicular SFCA, can also be seen in Figure 49b. The bonding phase in the 0% MP sinter (Figure 50a) is attached to an iron rich matrix, which is primarily composed of secondary hematite. This suggests that the fine hematite that was present in the mixture reduced to magnetite, which re-oxidized to form hematite. It also seems from the bonding structure that crystallization of these secondary iron oxides caused porosity along the rim of the relict material. The bonding structure in Figure 50b shows a distribution of the secondary phases suspended in a melt rich matrix. It can also be seen from Figure 50b that the SFCA phase in the bonding structure is primarily columnar as compared to the base case bonding structure. It can then be argued that the degree of material interaction in the 0% MP mixture was relatively higher than that of the base case mixture as a result of the presence of the high concentration of the fine iron ore concentrate (Debrincat *et al.*, 2004; Mežibrický *et al.*, 2019). This led to sufficient fluxing between CaO and Fe_2O_3, facilitating melt formation. Attachment by SFCA-I can also be seen in Figure 51a for the 10% MP particle. The bonding phase in this instance is slightly denser than the base case with a wider distribution of porosity. The bonding phase structure shown in Figure 51b is

© University of Pretoria

characterized primarily by acicular SFCA as well as magnetite particles. The attachment between the bonding phase and the relict particle in the 20% MP sinter differs slightly from the 10% MP mixture, however, it is similar to that of the base case. It can also be seen from Figure 52a that some reduction and re-oxidation took place as evidenced by the presence of secondary hematite along the rim of the nuclei particle. The bonding phase microstructure in Figure 52b is rather interesting showing a mixture of magnetite distributed across an SFCA/SFCA-I matrix. This behavior of crystallization of phases other than SFCA/SFCA-I was seen in the 0% MP and it can therefore be argued that there was a locally high amount of iron ore concentrate which facilitated this phenomenon. The attachment of the bonding phase to the relict particle in the 30% MP shows the same phenomenon as was reported for the 0% MP (Figure 53a). In this case however, the relict particle seems to have reduced slightly to form magnetite within the particle core. It can also be seen that not all the melt crystallized along the rim of the relict particle. The bonding phase structure shown in Figure 53b comprises of a fine network of acicular SFCA along the pore at the top right of the image. The sinter particle obtained from the 40% MP (Figure 54Figure a) shows an attachment of a relict particle to an SFCA-I-rich bonding phase with some secondary hematite present. The bonding phase structure in Figure 54b consists primarily of an SFCA-I matrix and magnetite particles of small grain size. It can also be seen that there was a considerable lack of secondary hematite precipitation in the 30% and 40% MP sinter as compared to cases with relatively higher concentrate contents.

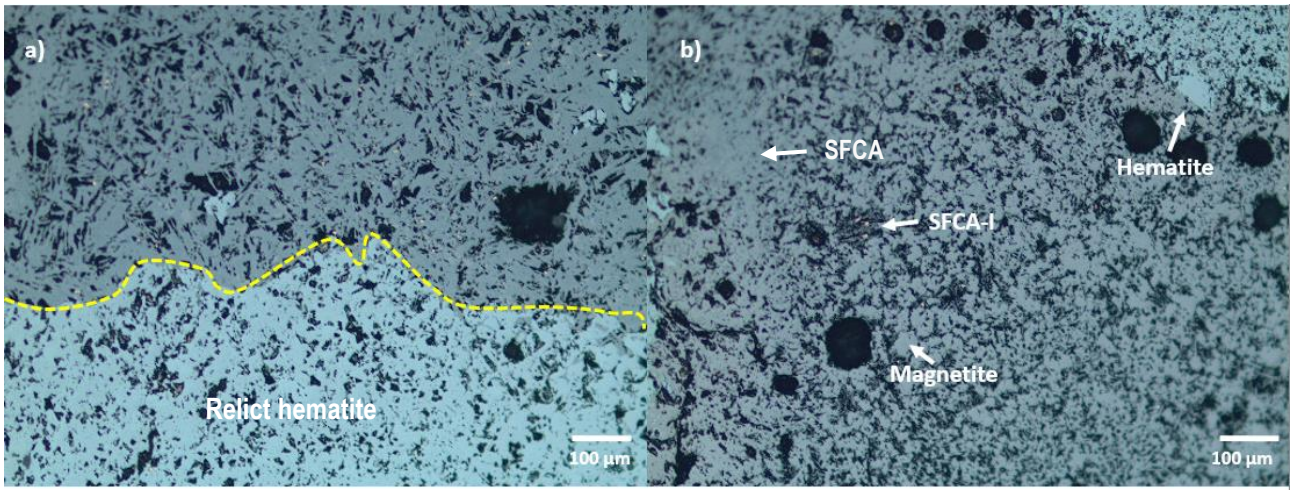

Figure 49: Optical micrographs of the base case sinter. a) Attachment of bonding phase to the relict particle; b) Bonding phase structure.

© University of Pretoria

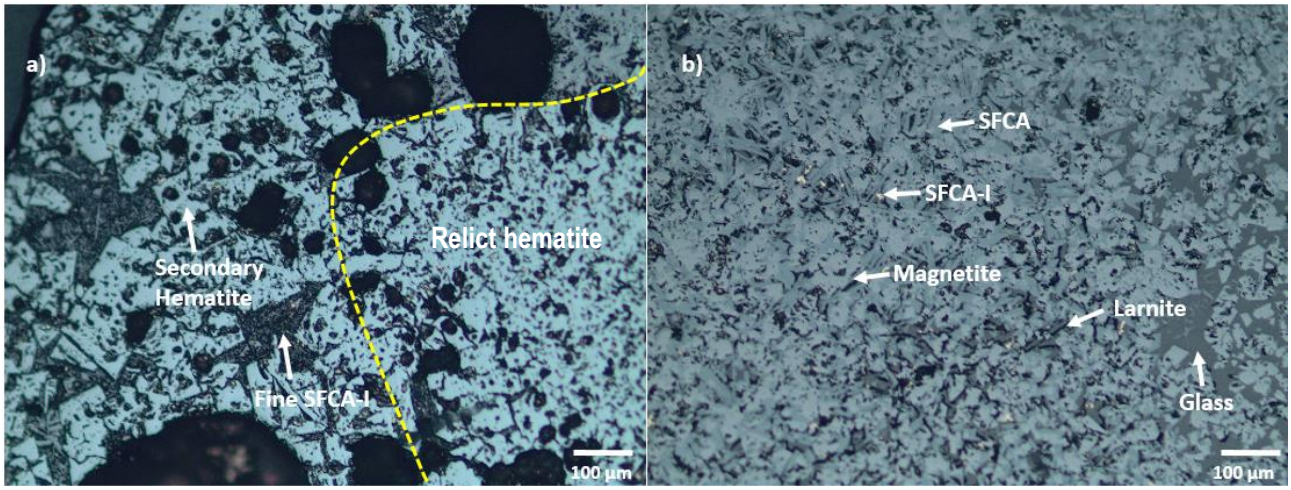

Figure 50: Optical microstructure of the 0% MP sinter. a) Attachment of bonding phase to relict particle; b) Bonding phase structure.

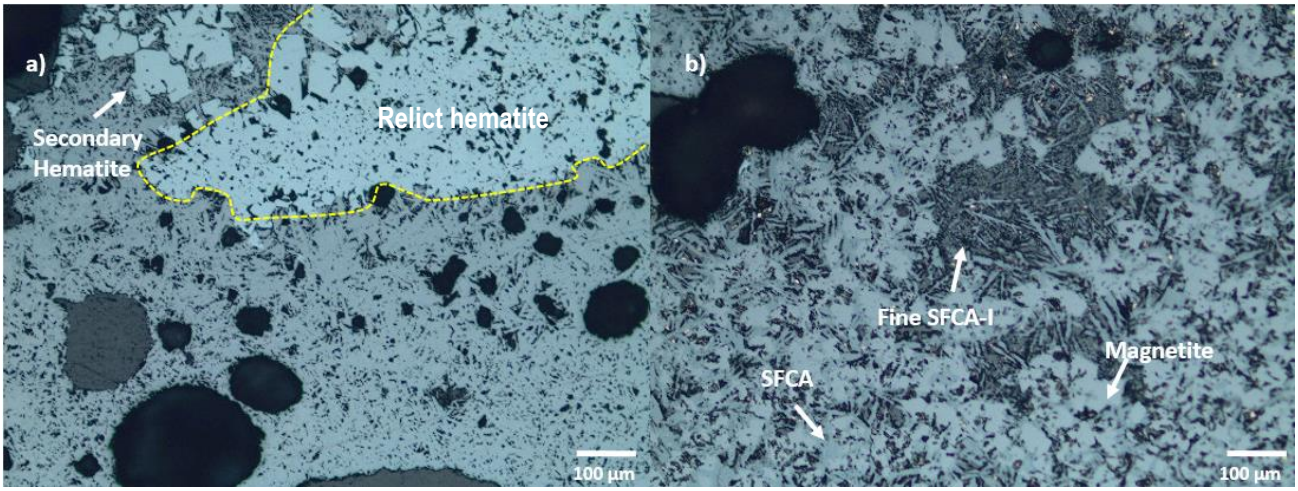

Figure 51: Optical microstructure of the 10% MP sinter. a) Attachment of bonding phase to relict particle; b) Bonding phase structure.

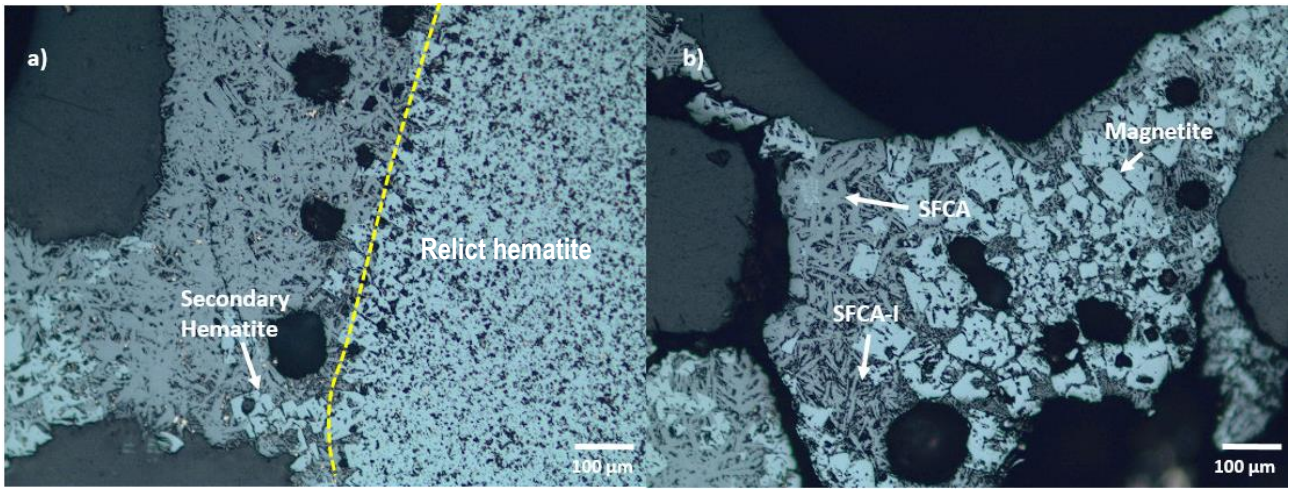

Figure 52: Optical microstructure of the 20% MP sinter. a) Attachment of bonding phase to relict particle; b) Bonding phase structure.

© University of Pretoria

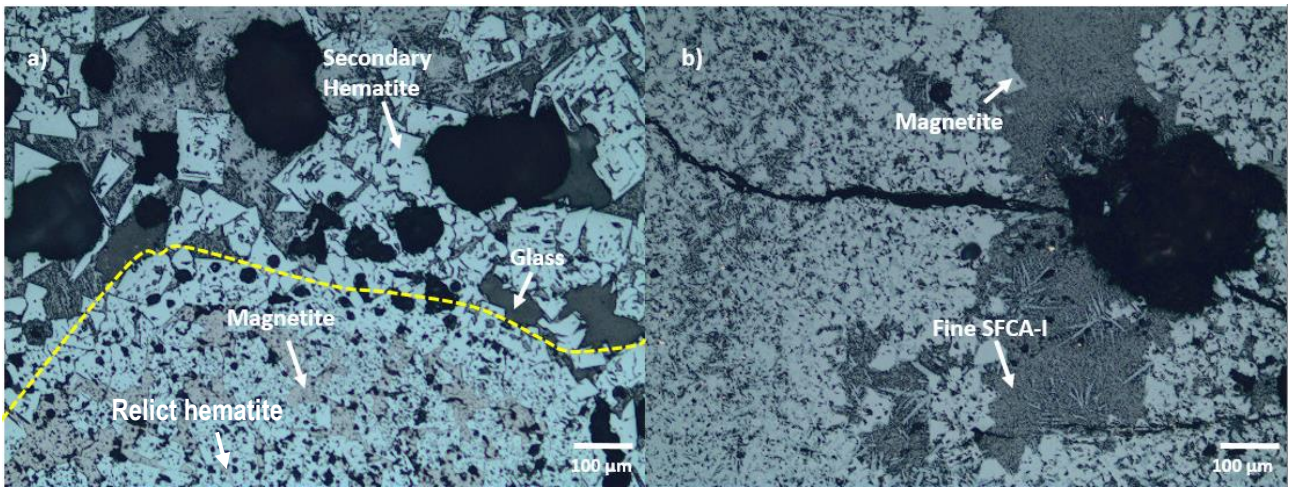

Figure 53: Optical microstructure of the 30% MP sinter. a) Attachment of bonding phase to relict particle; b) Bonding phase structure.

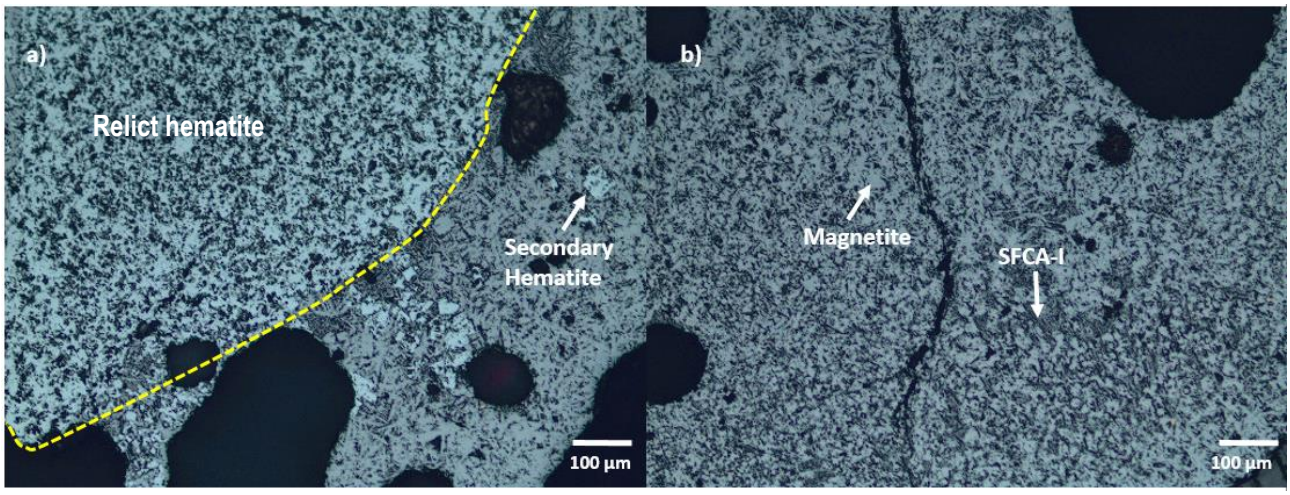

Figure 54: Optical microstructure of the 40% MP sinter. a) Attachment of bonding phase to relict particle; b) Bonding phase structure.

4.3.2.1.2 Iron ore micropellet and concentrate interaction with the melt

The microstructural contributions of iron ore concentrate and micropellets to the sinter microstructure were studied by observing the phase evolution before and after sintering. In the case of micropellets, raw micropellets were also fired using an infrared furnace without the addition of fluxes. This was done in order to assess whether the microstructural changes take place as a result of melt infiltration or not. The iron ore micropellets were prepared from iron ore concentrate and small additions of corn starch and Acronal® 296D acrylic (aqueous butyl acrylate-styrene copolymer dispersion) paint. The concentrate appears as a composite of fine hematite aggregates dispersed in a fine matrix (Figure 55a). Prior to firing, the micropellet consists of a fine hematite-silica matrix and coarse hematite aggregates less than 200 microns in size (Figure 55b). The reflected light micrograph of the unreacted micropellet (Figure 55b) shows that there is some porosity present in the micropellets and this can potentially affect the reactivity of the micropellets. When the micropellets were fired in the infrared furnace, the matrix seems to have sintered slightly as it appears denser than the raw micropellet.

© University of Pretoria

Figure 55c also shows the presence of skeletal hematite particles which would suggest that there was some reduction of hematite aggregates as well as some from the matrix. When the micropellet was coated with mixtures of iron ore fines, fluxes and coke, sintering took place along the rim of the micropellet whilst the core remained unreacted as shown in Figure 55d. This phenomenon is also reported in Figure 55 which shows a micropellet core surrounded by a fairly uniform rim. The fine pores in the rim suggest that there was no extensive melt formation around the micropellet during sintering. The dense nature of the rim also suggests that there was some reduction along the surface of the micropellet. The amount of reducing gas reaching the unreacted part of the micropellet however decreased as the film became thicker causing the core to remain unchanged. It can then be argued that similar to the coarse relict hematite particles, iron ore micropellets can only assimilate provided there are sufficient adhering fines to partially melt during sintering. The breaking down of micropellets during granulation however does also provide a mechanism by which they can be assimilated. Such breakdown however introduces fines which can negatively impact bed permeability.

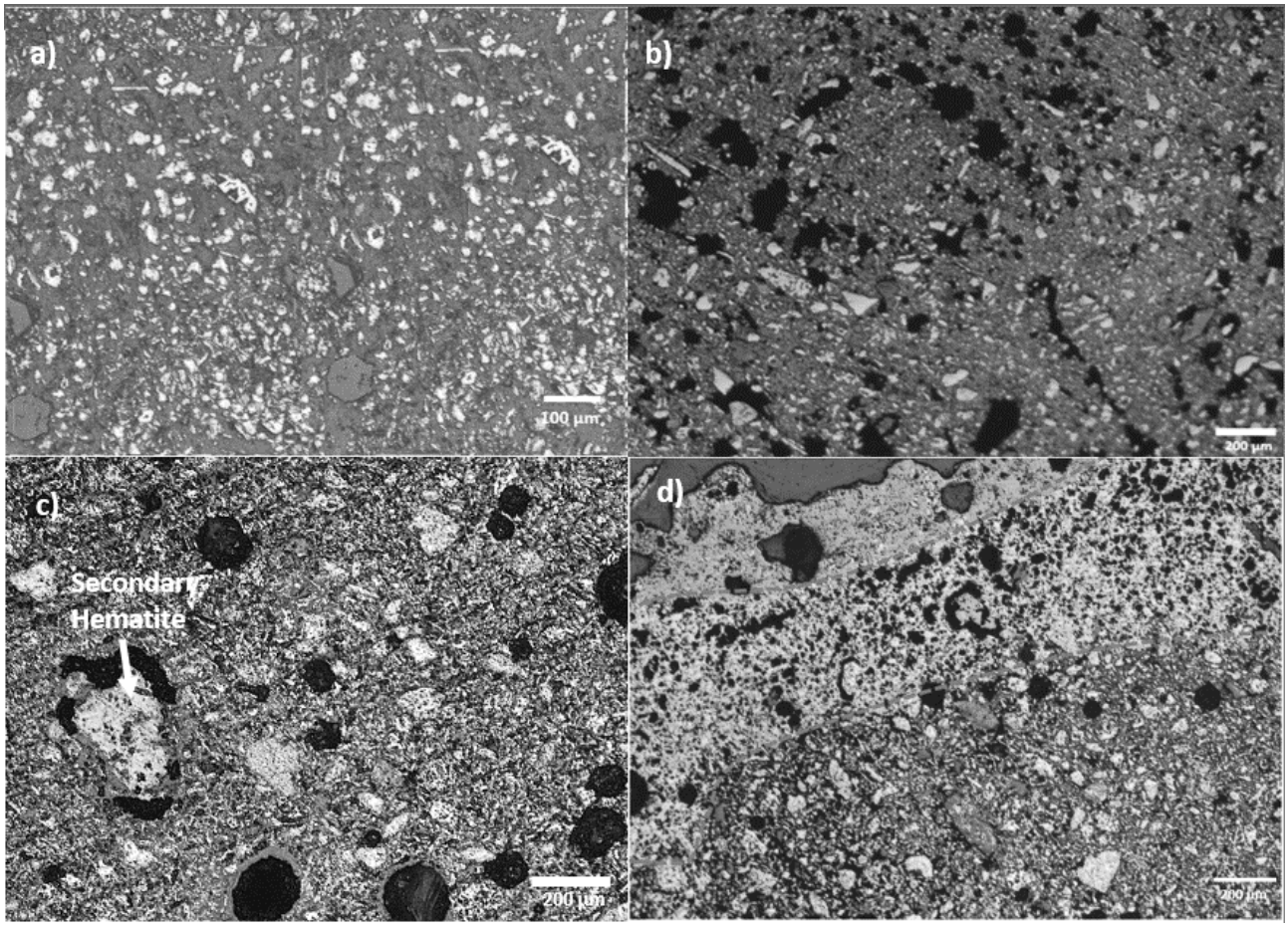

Figure 55: Optical micrographs of iron ore concentrate and micropellets. a) Concentrate; b) unreacted micropellet; c) fired micropellet; d) fired micropellet, which was coated with iron ore fines, fluxes and coke.

© University of Pretoria

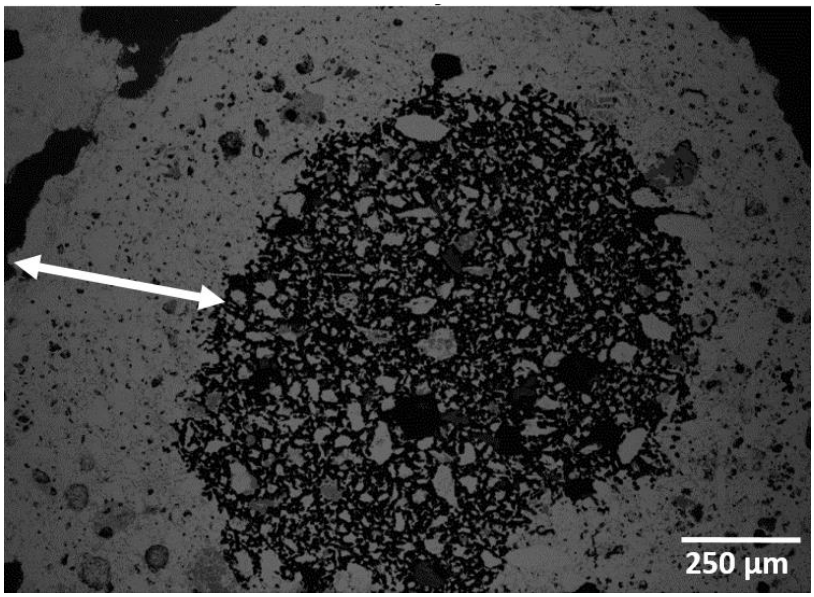

Figure 56: Iron ore micropellet obtained from the 20% MP sinter mixture showing a sintered layer and an unreacted core.

4.3.2.2 SEM – EDS

The electron backscatter images of the different sinters are shown in Figure 57 – 62 with the respective compositions of their major phases reported in Table 8 - 13. The base case microstructure is characterized by a large presence of hematite with patches of secondary phases as shown in Figure 57. The 0% MP sinter in Figure 58 is characterized by the presence of large magnetite and columnar SFCA crystals that have precipitated and grown from the melt during cooling as well as larnite. The crystals in this micrograph are relatively larger than the base case microstructure. The mineralogical makeup of the 10% MP sinter (Figure 59) is similar to that of the 0% MP sinter, with the exception of the secondary hematite having precipitated from the melt. In the melt surrounding the hematite crystal (labeled 1), there exists a lamella structure of hematite and larnite. This is presumably due to the fact that solubility of Fe ions in larnite decreases as it transforms from β to γ phase during cooling (Mulvaney, 1987). In the case of the 20% MP sinter shown in Figure 60, the SFCA appears more acicular rather than columnar as was seen in the case of 0% and 10% MP samples. The mixtures containing a higher amount of micropellets (i.e. 30% MP and 40% MP, Figure 61 and 62) are mainly characterized by more dendritic SFCA and less melt compared to the mixtures containing higher amounts of concentrate (i.e. 0% MP and 10% MP).

A close similarity can be observed regarding the chemistry of hematite in the sinters. The hematite with the highest purity is that of the 40% MP sinter with the lowest Al_2O_3 content. The magnetite phase however also contains Mg^{2+} and Ca^{2+} in its spinel structure. In this case, a higher solubility of these ions was seen in the base case sinter which contained 11.23% MgO and 2.57% CaO. It can also be seen that the 40% MP also absorbed relatively higher amounts of MgO and CaO compared to the other sinters containing either micropellets or

© University of Pretoria

concentrate. Despite appearing both columnar and needle-like, the SFCA phases have shown a relatively similar Fe-rich chemical composition. Iron oxide solubility into SFCA ranges from 64.95% (for the 20% MP) to 82.97% (for the 40% MP). Since K_2O has a significant fluxing effect in sinter, it is typical that it would be found in the glassy phase. The melt in the base case sinter is characterized by its high FeO contents and presence of small amounts of K_2O (0.5 mass%).

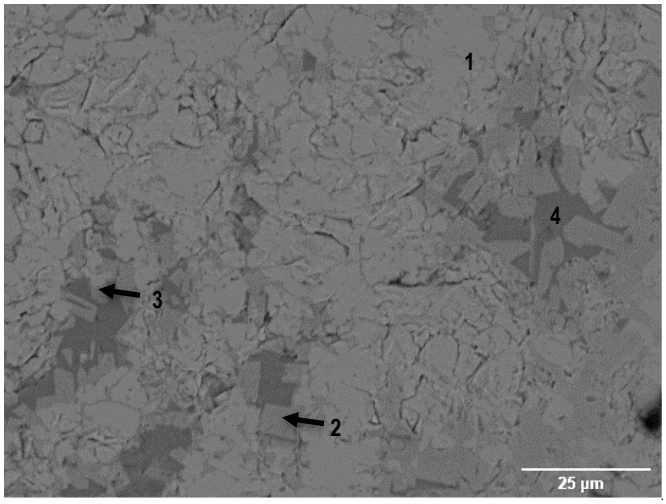

Figure 57: Electron backscatter image showing the phase distribution of the base case sinter (1,2,3,4: Refer to Table 8).

Table 8: Phase composition of the base case sinter (wt%).

Material	Fe-Oxide	SiO_2	Al_2O_3	K_2O	CaO	MgO	Formula
Hematite* (1)	97.42	0.00	2.58	0.00	0.00	0.00	$Fe_{2.09}Al_{0.09}O_{2.82}$
Magnetite**(2)	84.03	0.00	0.00	0.00	2.57	11.23	$Fe_{2.38}Mg_{0.63}Ca_{0.11}O_{3.88}$
SFCA* (3)	82.97	2.24	2.56	0.00	12.24	0.00	$Fe_{11.48}Ca_{2.43}Si_{0.42}Al_{0.56}O_{19.11}$
Larnite	0.00	36.81	0.00	0.00	63.19	0.00	$Ca_{1.78}Si_{0.97}O_{4.25}$
Glass** (4)	22.74	36.06	2.94	0.5	37.75	0.00	--

*Iron Oxide Species = Fe_2O_3
**Iron Oxide Species = FeO

© University of Pretoria

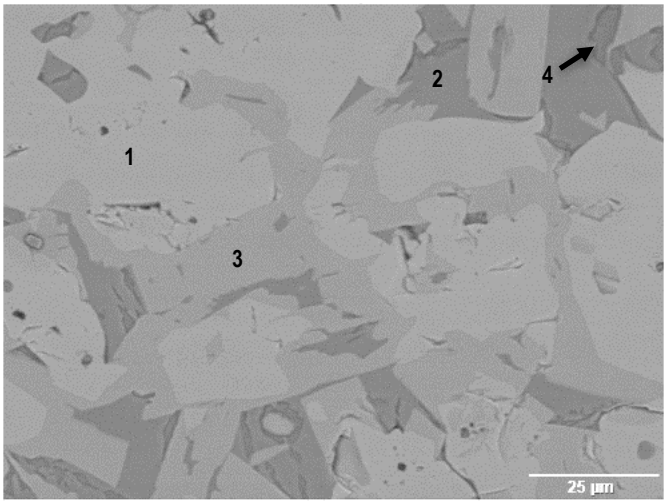

Figure 58: Electron backscatter image showing the phase distribution of the 0% MP sinter (1,2,3,4: Refer to Table 9).

Table 9: Phase composition of the 0% MP sinter (wt%).

Material	Fe-Oxide	SiO_2	Al_2O_3	K_2O	CaO	MgO	Formula
Hematite*	95.43	0.00	4.57	0.00	0.00	0.00	$Fe_{2.13}Al_{0.17}O_{2.71}$
Magnetite** (1)	97.48	0.00	0.00	0.00	1.21	1.31	$Fe_{3.02}Mg_{0.08}Ca_{0.05}O_{3.84}$
SFCA* (3)	71.35	8.67	4.86	0.00	15.12	0.00	$Fe_{9.33}Ca_{2.83}Si_{1.53}Al_{1.00}O_{19.32}$
Larnite (4)	0.00	37.16	0.00	0.00	62.84	0.00	$Ca_{1.81}Si_{1.00}O_{4.19}$
Glass** (2)	18.62	33.97	2.97	3.02	41.41	0.00	--

*Iron Oxide Species = Fe_2O_3
**Iron Oxide Species = FeO

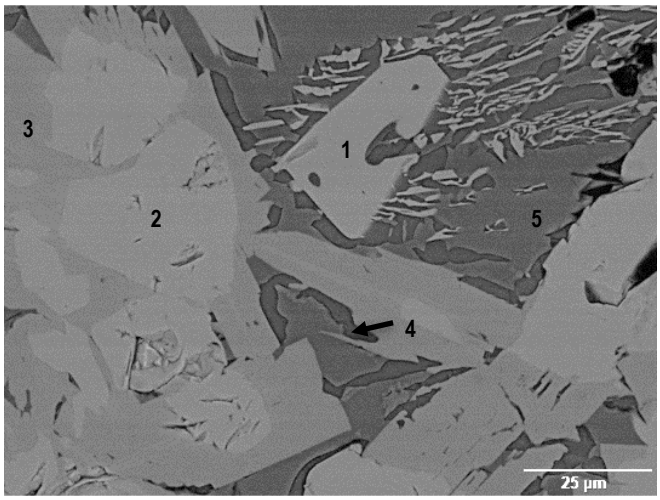

Figure 59: Electron backscatter image showing the phase distribution of the 10% MP sinter (1,2,3,4: Refer to Table 10).

© University of Pretoria

Table 10: Phase composition of the 10% MP sinter (wt%).

Material	Fe-Oxide	SiO_2	Al_2O_3	K_2O	CaO	MgO	Formula
Hematite* (1)	96.37	0.00	3.63	0.00	0.00	0.00	$Fe_{2.00}Al_{0.07}O_{2.92}$
Magnetite** (2)	94.85	0.00	0.00	0.00	2.07	3.08	$Fe_{3.03}Mg_{0.16}Ca_{0.06}O_{3.76}$
SFCA* (3)	69.78	7.15	6.37	0.00	16.70	0.00	$Fe_{8.18}Ca_{2.80}Si_{1.12}Al_{1.16}O_{20.75}$
Larnite (4)	0.00	35.77	0.00	0.00	64.23	0.00	$Ca_{1.73}Si_{0.90}O_{4.37}$
Glass** (5)	18.31	43.88	4.21	2.05	29.94	1.62	--

*Iron Oxide Species = Fe_2O_3
**Iron Oxide Species = FeO

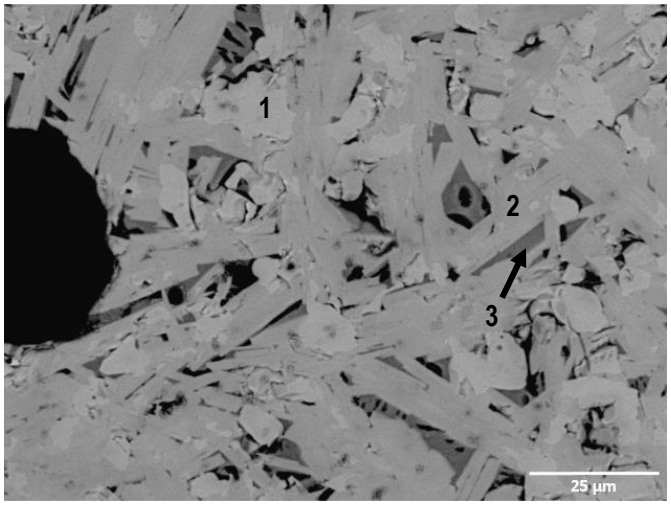

Figure 60: Electron backscatter image showing the phase distribution of the 20% MP sinter (1,2,3: Refer to Table 11).

Table 11: Phase composition of the 20% MP sinter (wt%).

Material	Fe-Oxide	SiO_2	Al_2O_3	K_2O	CaO	MgO	Formula
Hematite*	97.69	0.00	2.31	0.00	0.00	0.00	$Fe_{2.20}Al_{0.08}O_{2.72}$
Magnetite** (1)	95.96	0.00	0.00	0.00	1.06	2.98	$Fe_{2.73}Mg_{0.49}Ca_{0.04}O_{3.75}$
SFCA* (2)	64.95	10.44	5.34	0.00	19.27	0.00	$Fe_{8.18}Ca_{2.80}Si_{1.12}Al_{1.16}O_{20.75}$
Larnite	0.00	35.94	0.00	0.00	64.06	0.00	$Ca_{1.82}Si_{0.96}O_{4.23}$
Glass** (3)	14.63	36.67	7.11	1.43	37.40	1.97	--

*Iron Oxide Species = Fe_2O_3
**Iron Oxide Species = FeO

© University of Pretoria

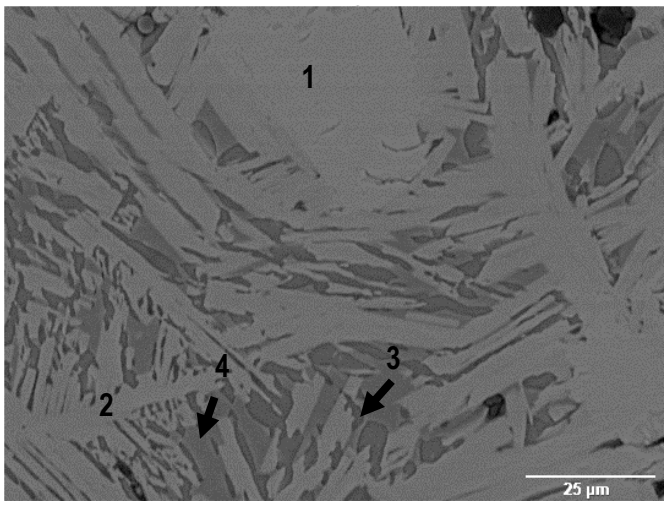

Figure 61: Electron backscatter image showing the phase distribution of the 30% MP sinter (1,2,3,4: Refer to Table 12).

Table 12: Phase composition of the 30% MP sinter (wt %).

Material	Fe-Oxide	SiO_2	Al_2O_3	K_2O	CaO	MgO	Formula
Hematite* (1)	98.82	0.00	1.18	0.00	0.00	0.00	$Fe_{2.05}Al_{0.04}O_{2.91}$
Magnetite**	93.93	0.00	0.00	0.00	0.00	6.07	$Fe_{2.72}Mg_{0.36}O_{3.92}$
SFCA* (2)	73.68	7.34	4.00	0.00	14.98	0.00	$Fe_{9.78}Ca_{2.85}Si_{1.31}Al_{0.84}O_{19.23}$
Larnite (3)	0.00	36.27	0.00	0.00	63.73	0.00	$Ca_{2.06}Si_{1.05}O_{3.88}$
Glass** (4)	17.51	38.98	3.54	3.79	35.54	0.63	--

*Iron Oxide Species = Fe_2O_3
**Iron Oxide Species = FeO

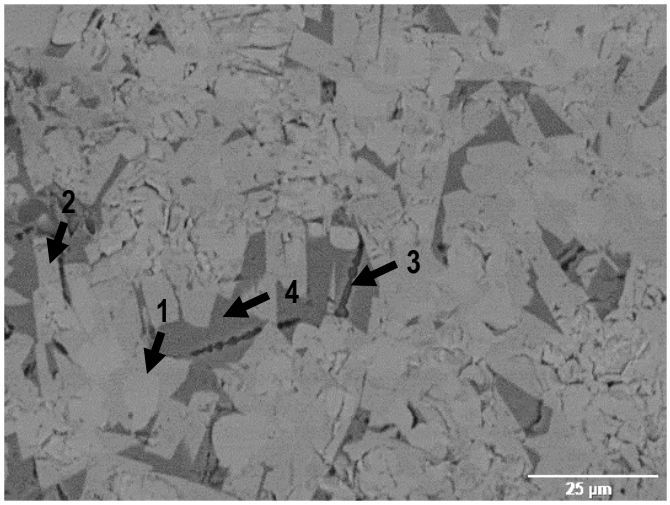

Figure 62: Electron backscatter image showing the phase distribution of the 40% MP sinter (1,2,3,4: Refer to Table 13).

© University of Pretoria

Table 13: Phase composition of the 40% MP sinter (wt%).

Material	Fe-Oxide	SiO_2	Al_2O_3	K_2O	CaO	MgO	Formula
Hematite*	99.14	0.00	0.86	0.00	0.00	0.00	$Fe_{1.97}Al_{0.03}O_{3.00}$
Magnetite** (1)	91.44	0.00	0.00	0.00	2.09	6.47	$Fe_{2.49}Mg_{0.35}Ca_{0.08}O_{4.08}$
SFCA* (2)	72.52	8.39	3.35	0.00	15.74	0.00	$Fe_{8.39}Ca_{2.60}Si_{1.29}Al_{0.60}O_{21.13}$
Larnite (3)	0.00	35.61	0.00	0.00	64.39	0.00	$Ca_{1.88}Si_{1.04}O_{4.08}$
Glass** (4)	17.99	38.51	2.50	2.24	38.76	0.00	--

*Iron Oxide Species = Fe_2O_3
**Iron Oxide Species = FeO

4.3.2.3 Micro focus X-ray micro tomography

The -25+16 mm sinter particles were observed through MF-XRT and the results are shown in Figure 63. It can be seen that the base case sinter and 0% MP sinter appear denser compared to the sinter containing 40% MP. The presence of the fine concentrate can be argued to have played a major role in facilitating the agglomeration of sinter as evidence also by dense regions of the 10, 20 and 30% MP sinters. The sinter containing 40% MP shows a significant number of open pores suggesting that during thermal densification there was less crystallization of phases out of the melt rather, crystallization of a porous phase (such as acicular SFCA). The base case sinter is also denser because it had slightly more adhering fines (-0.5 mm) than the 40% MP.

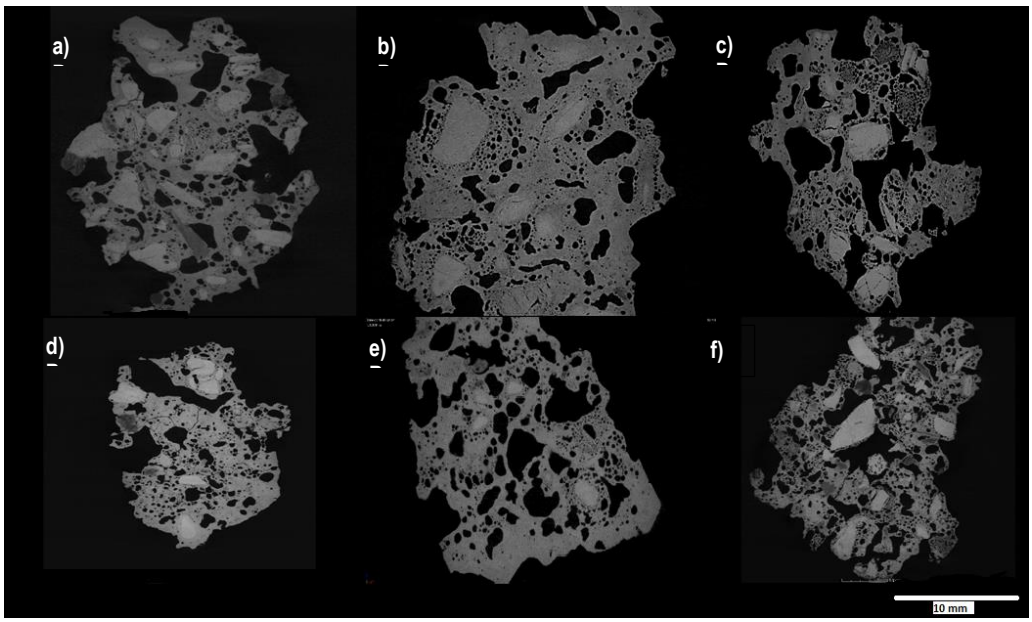

Figure 63: Internal structures of the different sinter particles observed through tomography analysis a) Base Case; b) 0% MP; c) 10% MP; d) 20% MP; e) 30% MP; f) 40% MP.

One aim of the MF-XRT analysis was to observe the interaction of micropellets with the bonding phases as well as other nuclei. It can be seen that most of the relict particles appearing on the tomograms of the sinter particles are mainly the ore particles and not micropellets (Figure 63). This is an important observation since the micropellets were added as spherical particles and it can be that they have been assimilated into the melt during

© University of Pretoria

thermal densification. As it was previously explained in Figure 40, the addition of moisture during granulation led to some degradation of micropellets which caused them to breakdown in the sinter bed. The breakdown of the micropellets exposed them to be completely absorbed in the melt during sintering. This is because little to no micropellets were observed during SEM and optical microscopy analysis. Cracks in the micropellets (reported in Figure 39) might have also played a part in the assimilation of micropellets during thermal densification.

4.4 Sinter Properties

Sinter properties that were examined in this study were the production rate, tumble strength, reduction disintegration and reducibility.

4.4.1 Production Rate

The effect of the addition of micropellets and concentrate on the production rate can be seen in Figure 64. The data points plotted are average values of three sinter pot tests with one standard deviation calculated for the error bars (1σ). The base case samples showed lower sinter times compared to all the other sinters. It can be deduced that the variation of micropellet : concentrate ratio did not have a significant impact on the production rate. However, the production rate of the base case sinter is significantly higher than those of the mixtures of micropellets and concentrate.

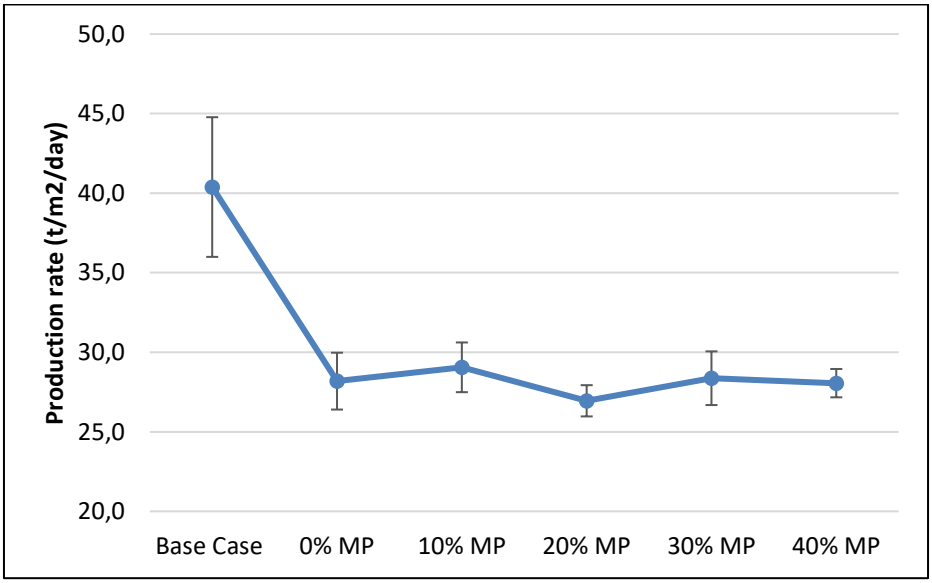

Figure 64: The influence of micropellet and concentrate addition on the production rate.

The relation between production rate and permeability (Figure 27) was not observed. The granulated base case mixture had the lowest permeability but the highest production rate (Figure 64). Table A.8 in Appendix A.3 shows the significant decrease in production rate was mainly due to increase production time when micropellets and concentrate were introduced in the sinter mixtures.

© University of Pretoria

4.4.2 Tumble Index

The effect of iron ore concentrate and micropellet addition on the tumble index is shown in Figure 65. All the sinters had a tumble index that exceeded the minimum industry required value of 70%. The variation in tumble index between the six evaluated sinters is low. The tumble index dropped slightly with the addition of iron ore concentrate. The introduction of micropellets increased the average tumble index however this increase was also slight (0.5% higher than the base case). The highest average tumble index was that of the 20% MP sinter and it was only 1.1% more than the base case sinter. The 30% MP sample presented the sinter with the lowest tumble index which was however 0.5% less compared to the base case. Standard deviations of the tumble indices indicate that the introduction of iron ore concentrate and micropellets does not have a significant impact on sinter strength.

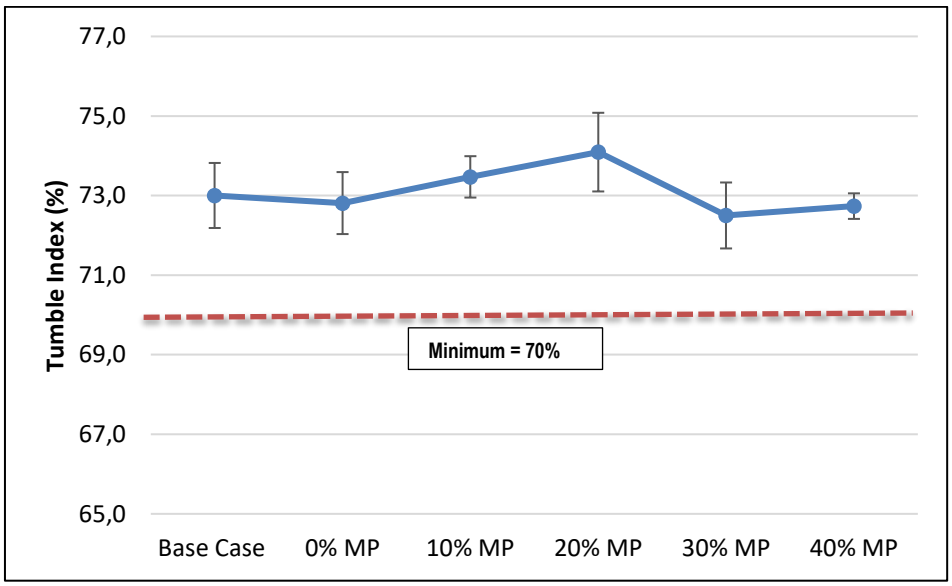

Figure 65: The influence of micropellet and concentrate addition on tumble index.

4.4.3 Reduction Disintegration Index

The effect of iron ore concentrate and micropellet addition on the Reduction Disintegration Index is shown in Figure 66 - 68 for -6.3, -3.15 and -0.5 mm fractions respectively. The addition of iron ore concentrate and micropellets to the sinter mixture generally increased the amount of fines formed during reduction. The 0% MP sinter reported a -6.3 mm fraction of 32.1% which increased to 33.4% when the 10% MP was introduced. Increasing to 20% MP however resulted in the RDI dropping which continued up to the 40% MP sinter. The $RDI_{-6.3\,mm}$ for the 40% MP sinter was even slightly lower than that of the base case sinter. The sinters containing high amounts of concentrate (i.e. 0% MP and 10% MP) however reported lower amounts of -3.15 and -0.5 mm fines compared to both the base case and sinters containing more micropellets. All the sinters however, exceeded the industry required limits on the $RDI_{-3.15\,mm}$ and $RDI_{-0.5\,mm}$.

© University of Pretoria

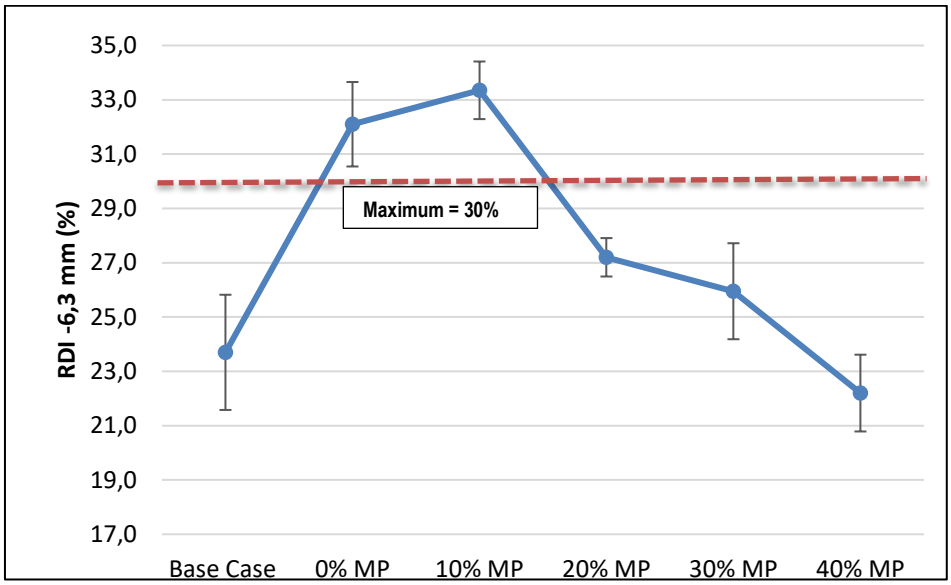

Figure 66: Impact of micropellet and concentrate addition on -6.3 mm disintegration index.

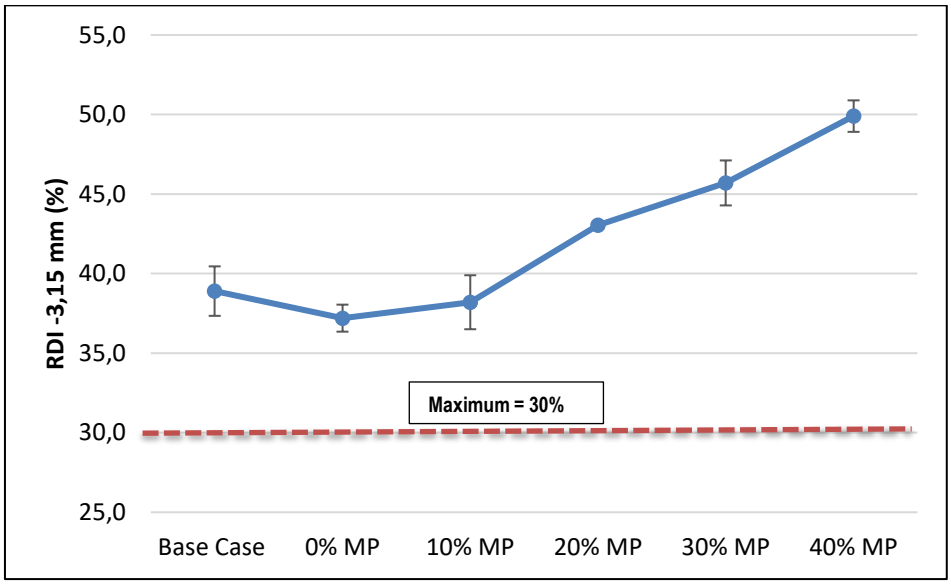

Figure 67: Impact of micropellet and concentrate addition on -3.15 mm disintegration index.

© University of Pretoria

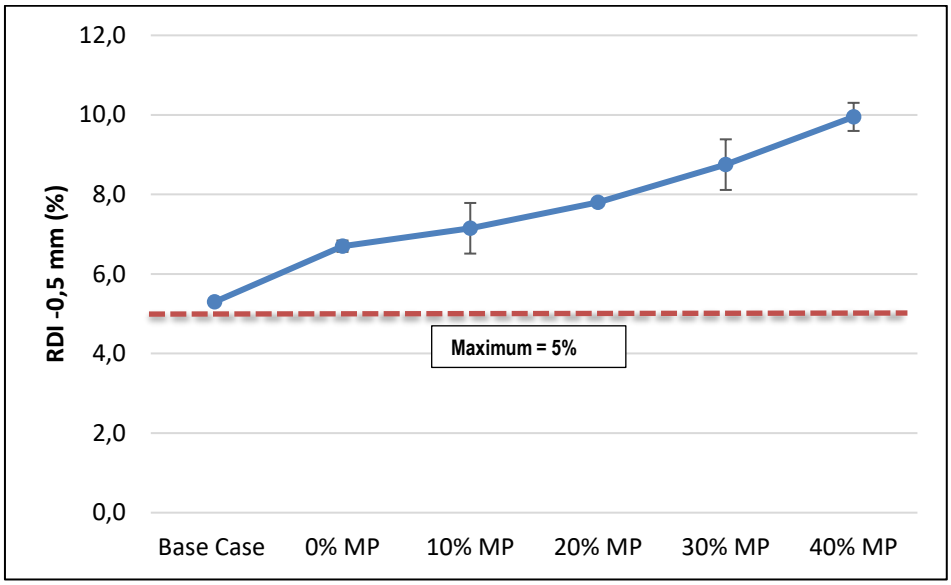

Figure 68: Impact of micropellet and concentrate addition on -0.5 mm disintegration index.

4.4.4 Reducibility Index

The effect of iron ore concentrate and micropellet addition on the reducibility of the sinter was also studied and the results are plotted in Figure 69. The RI of the sinters that contained concentrate and micropellets did not differ significantly from that of the base case sinter, with RI values ranging between 1.5 and 2 $\%min^{-1}$. It can be seen that the 0% MP sinter reported a slightly higher reducibility which however dropped when the 10% MP was introduced. The reducibility index increased with the addition of 20% MP followed by a decrease in the RI's of the 30% and 40% MP sinters.

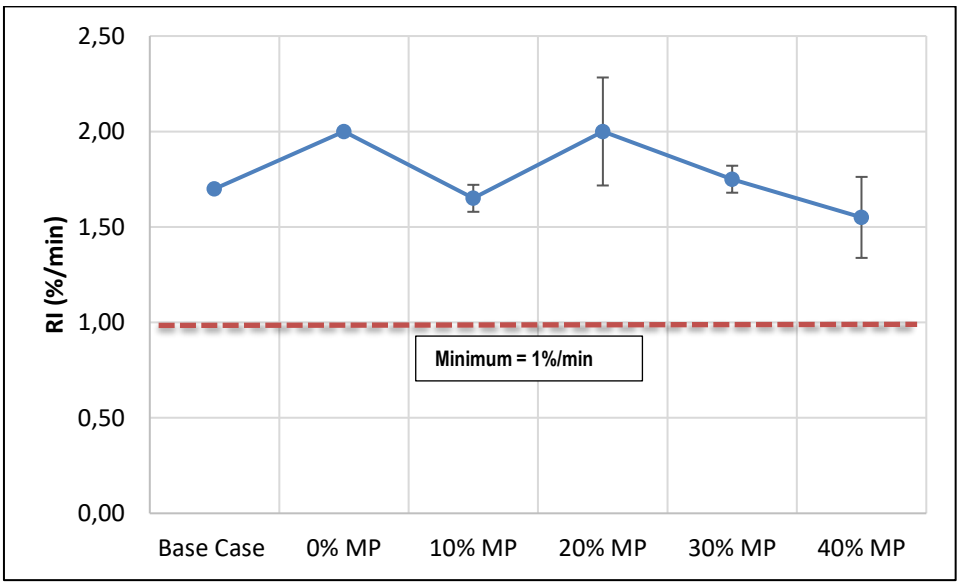

Figure 69: The impact of micropellet and concentrate addition on the reducibility index.

© University of Pretoria

Chapter 5
Discussion of results

5.1 Granulation

The mean granule size before granulation increased when the quantity of micropellets was increased, as was expected. After granulation however it was found that the 10% MP mixture which contained 33.60 mass% particles in the -0.5 mm fraction prior to granulation resulted in the coarsest granules after granulation. The mixture that contained 40% MP had the lowest mean granule size after granulation despite being the coarsest prior to granulation. Together with a variation in material transfer and granule growth, there was some decrease in the thickness of adhering fines as micropellets replaced concentrate in the sinter mixtures. This means that auto layering was less extensive as the amount of concentrate decreased. Coalescence layering however, was relatively similar in both the 0% and 10% MP mixture. It does appear therefore that a significant quantity of concentrate must be present to provide material for coalescence to occur.

5.2 Correlation between mineralogy and granulation

In order to understand the effect of iron ore concentrate and micropellets addition on the mineralogy of the sinter, the particle size has to be taken into consideration. This is due to the fact that by varying the ratio between the concentrate and micropellets only varied the size of the iron ore source and not the chemical compositions of the starting mixtures, since the micropellets were produced from concentrate. The increase in hematite content and decrease in magnetite content with increasing amount of micropellets can be explained by the increase in mean particle size before granulation. This resulted in a decrease in surface contact between the coke, fluxes and hematite in the micropellets. Despite having the highest mean granule size, the 10% MP sinter had the highest amount of magnetite, lowest amounts of SFCA and SFCA-I, but also low amount of larnite. This was presumably due to the coalescence layering mechanism reported by Nyembwe *et al.*, (2016b), which suggests that during granulation, a coagulation of fines from the concentrate in the presence of moisture would lead to the formation of granules without the presence of a core (Nyembwe *et al.*, 2016b).

According to Webster *et al.* SFCA-I can form prior to melt formation as a result of the reaction between Fe_2O_3, calcium ferrites and SiO_2, and decompose upon melt formation into Fe_2O_3 and melt. Although upon cooling SFCA-I forms again, it is short lived as further reaction with the melt leads to the formation of SFCA (Webster *et al.*, 2014). This is particularly important because the 0% MP sinter which has a relatively high mean granule size had the highest amount of SFCA. This suggests that the granules formed from this mixture were sufficiently fluxed to allow for melt formation and the cooling was sufficiently slow to allow for the crystallization of SFCA. Based on the increasing SFCA-I content as the micropellet content was increased, it can be argued that the degree of melt formation decreased. This can also be seen from the decrease in larnite which normally

© University of Pretoria

precipitates from silica rich parts of the melt (Mulvaney and Survey, 2015; Hapugoda *et al.*, 2016). Since SFCA-I is mostly stable during the heating stage, those sinters containing high concentrations of SFCA-I suggest that not a large amount of melt remained.

The sinter microstructure for the different sinter mixtures can be explained by considering the different layering mechanisms that took place during granulation. It can be said that the microstructure of sinter particles is highly dependent on the composition of the quasi-particles that packed the sinter bed. The microstructure of the base case sinter is a result of group I layering (auto layering) which was the only layering mechanism during granulation. In the case of the 0% MP sinter however, coalescence layering came into effect which resulted in iron ore concentrate rich quasi-particles. This explains the melt dispersion across the bonding phase structure. Despite coalescence in the 0% MP, fines rich in iron ore concentrate attached to coarse ore particles during auto layering which resulted in some secondary hematite precipitation along the ore particles. When the concentrate was still in relatively large quantities as in the case of the 10% MP sinter, there was still some slight precipitation of secondary hematite along the bonding phase structure attached to the ore particle. The presence of secondary hematite fragments in the case of the 20% MP bonding phase structure is quite peculiar since the amount of concentrate in the fines was lower than that of the 10% MP. The abrasion of micropellets and disintegration due to moisture during granulation are also a source of iron ore concentrate and this could have led to increased concentrate levels in some parts of the bed. Although the amount of fine concentrate was relatively lower in the 30% MP sinter, auto layering resulted in extensive reaction between the melt and unreacted hematite. This is clear when considering the presence of secondary hematite, magnetite as well as melt together with the SFCA matrix.

There was some auto layering on the micropellets during granulation. However, their smoothness and spherical shape make it difficult for some fine material to attach, which then resulted in less precipitation of phases such as SFCA/SFCA-I. The general reactivity of the micropellets in sinter mixtures is however masked by their disintegration during granulation. Tomographs of green micropellets show that deformed micropellets promoted auto layering, spherical micropellets however contributed less to the picking up of adhering fines. Some micropellets were also identified to have broken off from the sinter particle all together. The inability to identify micropellets in the sinter micrographs (both SEM and light microscopy) also indicates that micropellets did not play an active role of acting as seeds for quasi-particle development. It can therefore be argued that micropellets cannot provide a potential seed for the growth of quasi-particles without modifying their surface properties or preventing them from disintegration during granulation and sintering.

© University of Pretoria

5.3 Correlation between the mineralogy, properties and structure of the sinter

Although the XRD results show slight variations in the amounts of crystalline phases formed in the different sinters, little difference in mechanical properties at room temperature was observed. The TI of sinters that contain concentrate, micropellets or a combination of concentrate and micropellets, are similar to the TI of the base case sinter. The change in measured sinter strengths (TI) does not correspond to the change in the SFCA content of the sinter. Optical micrographs also show that the bonding phase structures of the sinters containing higher quantities of micropellets consisted primarily of fine SFCA. However, they had similar tumble indexes as sinters with denser bonding phase structures. These TI's can be explained by considering the fact that the sinters were of similar chemical composition and that MF-XRT revealed nearly similar geometries.

The RI also remained fairly constant (at acceptable levels exceeding 1% / min) despite varying the concentrate and micropellet quantities. This indicates that the granule size distribution of the mixtures did not play a significant role in reduction. It can be reasoned that since the chemical compositions of the sinter mixtures were similar, their reducibility indices would be similar.

$RDI_{-3.5\ mm}$ and $RDI_{-0.5\ mm}$ increased significantly for sinters prepared from micropellets and concentrate. There was also an abrupt increase in $RDI_{-3.5\ mm}$ for the sinters which implies that sinters with higher proportions of micropellets tend to produce more fines compared to sinters containing higher proportions of concentrate. The $RDI_{-0.5\ mm}$ also indicates a similar phenomenon. In general, mixtures with micropellets resulted in larger amounts of fines produced compared to the base case. The $RDI_{-3.5\ mm}$ and $RDI_{-0.5\ mm}$ also exceeded the acceptable limits of 30% and 5% respectively. It can be argued that with the increasing amounts of fines as micropellets and concentrate are added, there is somewhat a significant binding failure at or near the surface of the sinters. The decrease in the -6.3 mm fraction however also shows that although binding failure is there, the sinters have relatively sound structural integrity. Observing the increase in both -3.15 mm and -0.5 mm when micropellets are increase, it can also be argued that the binding for low micropellet sinters is more effectively and more localized. This would explain the peculiarity of the high -6.3 mm fraction for the 0% and 10% MP sinters.

© University of Pretoria

Chapter 6
Conclusions

The main focus of this study was to assess the viability of utilizing iron ore concentrate and micropellets as sinter feed. Sinters were produced from mixtures containing different proportions of iron ore concentrate and micropellets. The micropellets were produced from the iron ore concentrate. The granulation properties of the sinter mixtures were evaluated, as well as the chemical, mineralogical, structural, strength and metallurgical properties of the produced sinters. From the study it was established that:

- During granulation micropellets can deform, disintegrate or maintain their smooth and spherical nature. Those that deformed seem to have taken part in auto layering, those that disintegrated formed part of the fines and those that maintained their shape contributed little to the formation of quasi-particles.
- Apart from auto layering (Gr I layering), two other granulation mechanisms were observed from the addition of iron ore concentrate and micropellets namely; coalescence (Gr II) and adhesion of micropellets (Gr IV). Coalescence was observed in the 10% MP mixture (containing 10% micropellets – 30% concentrate) and was associated with the pelletization of the concentrate during granulation. The adhesion of micropellets was observed in the 40% MP mixture (containing 40% micropellets – 0% concentrate). It was also determined that the micropellets did not act as nuclei during auto layering as most quasi-particles contained ore particle nuclei.
- Material transfer efficiencies in excess of 94% was achieved during the granulation of the raw material mixtures that contained 0, 10 and 20% micropellets (40, 30 and 20% concentrate).
- Although the 40% MP mixture contained the highest mean particle size before granulation, the 10% MP sample had the highest mean granule size after granulation.
- Auto layering seem to have taken place in a fairly consistent manner across the sinter mixtures with the only exception of the 0% MP mixture which showed a thick layer of adhering fines attached to nuclei. Despite this, mixtures containing high concentrate quantities did show considerable quasi-particle growth.
- The addition of iron ore concentrate and micropellets to the sinter mixture resulted in a considerable increase in permeability. Maximum permeability was achieved when 30% micropellets and 10 % concentrate was used in the granulation mixture (30% MP).
- The hematite content in the sinter increased when the iron ore micropellets replaced the fine concentrate. This was attributed to a decrease in reaction surface area as the mean granule size of the sinter mixtures before granulation decreased. The sinter produced from the mixture that contained the highest amounts of concentrate (0% MP) had the highest SFCA content as a result of a higher reactivity between the concentrate and fluxes. This is consistent with what has been reported by Fan *et al.*, (2013).
- The base case sinter as well as the 0 and 20% MP sinters appeared denser than the 10, 30 and 40% MP sinters as shown by tomography. Micropellets in any of the sinters could not be identified.

© University of Pretoria

- The addition of iron ore concentrate and micropellets resulted in a significant drop in sinter production rates.
- The addition of iron ore concentrate, micropellets and mixtures of concentrate and micropellets did not significantly affect sinter strength as the produced sinters had similar tumble indexes to the base case sinter. These values were however higher than the minimum Tumble Index specified by industry of 70%.
- The introduction of iron ore concentrate and micropellets resulted in a general increase in the amount fines that form due to reduction degradation. It was seen that sinters containing high amounts of micropellets experienced a more severe degradation due to the inability of the micropellet to properly assimilate during sintering. Compared to industry standards, the sinters produced performed fairly poorly in terms RDI with all them showing over 5% fines (-0.5 mm) and over 30% fines for the -3.5 mm fraction.
- Reducibility remained fairly consistent across all the sinters (incl. base case) and all of them were higher than industry specifications of 1%/min.
- The addition of iron ore concentrate and micropellets resulted in a significant drop in production rate compared to the base case. The production rate also remained constant for the mixtures containing the concentrate and micropellets.

From this study, it was observed and concluded that the role of micropellets in the sinter mixtures studied was similar to that of the fine iron ore concentrate. It would seem in this instance rather viable to only use iron ore concentrate as feed due to its lower production cost. For purposes of developing coarse sinter mixtures however, thorough considerations must be made into improving the integrity and surface characteristics of micropellets. This would include using binders that are more water phobic to prevent excessive wetting and disintegration of the green pellets. Since water plays an important role in the general quasi-particle formation, a careful balance would then be required to avoid preventing the micropellets from attaching to the rest of the mixture. Addition of lime can also be attempted in order to improve micropellet strength.

© University of Pretoria

Chapter 7
References

Bhagat, R., Chattoray, U. and SiL, S. . (2006) 'Porosity of sinter and its relation with the sintering indices', *ISIJ International*, 46(11), pp. 1728–1730.

Bish, D. and Post, J. (1989) 'Modern Powder Diffraction. Reviews in Mienralogy', *Mineralogical Society of America*, 20.

Brouwer, P. (2010) *Theory of XRF*, *Almelo: PANalytical BV*.

Cai, B., Watanabe, T., Kamijo, C., Susa, M. and Hayashi, M. (2018) 'Comparison between Reducibilities of Columnar Silico-ferrite of Calcium and Aluminum (SFCA) Covered with Slag and Acicular SFCA with Fine Pores', (May). doi: 10.2355/isijinternational.ISIJINT-2017-552.

Chaigneau, R. (1994) *Fluxed sinter formation and SFCA reduction under Simulated Conditions*.

Chen, Y. G., Guo, Z. C. and Feng, G. S. (2011) 'NO x reduction by coupling combustion with recycling flue gas in iron ore sintering process', *International Journal of Minerals, Metallurgy and Materials*, 18(4), pp. 390–396. doi: 10.1007/s12613-011-0452-7.

Debrincat, D., Loo, C. E. and Hutchens, M. F. (2004) 'Effect of Iron Ore Particle Assimilation on Sinter Structure', *ISIJ International*, 44(8), pp. 1308–1317.

Eisele, T. C. and Kawatra, S. K. (2010) 'A review of binders in iron ore pelletization', *Taylor and Francis*, 7508(2003), pp. 1–86. doi: 10.1080/08827500306896.

Fan, J., Qiu, G., Jiang, T., Guo, Y. and Mu, K. (2013) 'Improvement of Sinter Properties With Ultra Fine-Sized Iron Concentrate by HPRG', *Journal of Iron and Steel Research, International*, 20(9), pp. 47–52. doi: 10.1016/S1006-706X(13)60155-7.

Fernández-González, D., Ruiz-Bustinza, I., Mochón, J., González-Gasca, C. and Verdeja, L. F. (2017a) 'Iron Ore Sintering: Process', *Mineral Processing and Extractive Metallurgy*, 1547(7508), pp. 215–227. Available at: https://doi.org/10.1080/08827508.2017.1288115.

Fernández-González, D., Ruiz-Bustinza, I., Mochón, J., González-Gasca, C. and Verdeja, L. F. (2017b) 'Iron Ore Sintering: Raw Materials and Granulation', *Mineral Processing and Extractive Metallurgy Review*. Taylor & Francis, 38(1), pp. 36–46. doi: 10.1080/08827508.2016.1244059.

Fitton, G. (1997) 'Modern Analytical Geochemistry: An Introduction to Quantitative Chemical Analysis for Earth, Environmental and Material Scientists', in *X-Ray fluorescence spectrometry*.

Formoso, A., Moro, A., Fernández Pello, G., Menéndez, J. L., Muñiz, M. and Cores, A. (2003) 'Influence of nature and particle size distribution on granulation of iron ore mixtures used in a sinter strand', *Ironmaking & Steelmaking*, 30(6), pp. 447–460. doi: 10.1179/030192303225004187.

Fröhlichová, M., Ivanišin, D., Findorák, R., Džupková, M. and Legemza, J. (2018) 'The effect of concentrate/iron ore ratio change on agglomerate phase composition', *Metals*, 8(11), pp. 1–11. doi: 10.3390/met8110973.

Garba, N., Yamusa, A., Isma'ila, A. and Habiba, S. (2013) 'Heavy metal concentration in soil of some mechanic workshops of Zaria-Nigeria', *International journal of physical science*, 44(8), pp. 2029–2034.

Geerdes, M., Toxopeus, H. and van der Vliet, C. (2009) *Modern Blast Furnace Ironmaking*. Second. Edited by R. Chaigneau, T. Vander, and J. Wise. IOS Press.

© University of Pretoria

Hapugoda, S., Lu, L., Donskoi, E., Manuel, J., Lu, L., Donskoi, E., Mineralogical, J. M., Hapugoda, S., Lu, L., *et al.* (2016) 'Mineralogical quantification of iron ore sinter Mineralogical quanti fi cation of iron ore sinter', 9553. doi: 10.1080/03719553.2016.1164797.

Hida, Y., Ito, K., Sasaki, M. and Umezu, Y. (1983) 'Effect of the mineralogical properties of coarse ores on the reducibility and the productivity of sinter', *Transactions ISIJ*, 23, p. B-3.

Higuchi, K., Orimoto, T., Koizumi, F., Furuta, H., Takamoto, Y., Sato, T. and Shinagawa, K. (2006) 'Quality improvement of sintered ore in relation to blast furnace operation', *Nippon Steel Technical Report*, 94, pp. 36-41.

Hoffman, J. W. and De Beer, F. C. D. E. (2012) 'Characteristics of the Micro-Focus X-ray Tomography Facility (MIXRAD) at Necsa in South Africa', (April), pp. 16–20.

Hsieh, L. H. (2017) 'Effect of iron ore concentrate on sintering properties', *ISIJ International*, 57(11), pp. 1937–1946. doi: 10.2355/isijinternational.ISIJINT-2017-276.

Husslage, W. ., Bakker, T., M.E, K. and Heerema, R. (1999) 'Influence of reduction conditions on the expansion and microstructure of sintered hematite compacts during the transition to magnetite', *Minerals & Metallurgical Processing*, 16(3), pp. 23–33.

Kalenga, M. K. and Garbers-Craig, A. M. (2010) 'Investigation into how the magnesia, silica, and alumina contents of iron ore sinter influence its mineralogy and properties', *Journal of the Southern African Institute of Mining and Metallurgy*, 110(8), pp. 447–456.

Lu, L. (2015) *Iron Ore*. 56th edn. Sawston, Cambridge: Woodhead Publishing.

Lu, L., Holmes, R. J. and Manuel, J. R. (2007) 'Effects of Alumina on Sintering Performance of Hematite Iron Ores', *ISIJ International*, 47(3), pp. 349–358. doi: 10.2355/isijinternational.47.349.

Lu, L. and Ishiyama, O. (2016) 'Recent advances in iron ore sintering', *Transactions of the Institutions of Mining and Metallurgy, Section C: Mineral Processing and Extractive Metallurgy*, 125(3), pp. 132–139. doi: 10.1080/03719553.2016.1165500.

Lwamba, E. (2007) 'Optimisation of the grain size distribution of the raw material mixture in the production of iron ore sinter By', *Journal of the Southern African Institute of Mining and Metallurgy*, (August).

Lwamba, E. and Garbers-Craig, A. M. (2008) 'Control of the grain size distribution of the raw material mixture in the production of iron sinter', *Journal of the Southern African Institute of Mining and Metallurgy*, 108(5), pp. 293–300.

De Magalhaes, M. S. and Brandao, P. R. (2003) 'Microstructures of industrial sinters from Quadrilatero Ferrifero's iron ores', *Minerals Engineering, Elsevier*, p. 1251.

Mao, H., Zhang, R., Lv, X., Bai, C. and Huang, X. (2013) 'Effect of surface properties of iron ores on their granulation behavior', *ISIJ International*, 53(9), pp. 1491–1496. doi: 10.2355/isijinternational.53.1491.

Mbele, P. (2012) 'Pelletizing of Sishen concentrate', *Journal of the Southern African Institute of Mining and Metallurgy*, 112(September 2011), pp. 5–7.

Mežibrick, R. and Goettgens, V. S. (2019) 'Ore Assimilation and Secondary Phases by Sintering of Rich and High-Gangue Iron Ores', pp. 1–25. doi: 10.3390/min9020128.

Mežibrický, R., Fröhlichová, M., Findorák, R. and Goettgens, V. (2019) 'Ore Assimilation and Secondary Phases by Sintering of Rich and High-Gangue Iron Ores', *Minerals*, 9(2), p. 128. doi: 10.3390/min9020128.

© University of Pretoria

Mochon, J., CORES, A., RUIZ-BUSTINZA, Í., VERDEJA, L. F., ROBLA, J. I. and GARCIA-CARCEDO, F. (2014) 'Iron Ore Sintering Part 2. Quality Indices and Productivity', *Dyna*, 81(183), pp. 168–177. doi: 10.15446/dyna.v81n183.41568.

Mulvaney, R. (1987) 'Iron ore sinter in the analytical transmission electron microscope', *Mineralogical Magazine*, 51(359), pp. 61–69. doi: 10.1180/minmag.1987.051.359.06.

Mulvaney, R. and Survey, B. A. (2015) 'Iron Ore Sinter in the Analytical Transmission Electron Microscope Iron ore sinter in the analytical transmission electron microscope', (February). doi: 10.1180/minmag.1987.051.359.06.

Mumme, W. G., Clout, J. M. F. and Gable, R. W. (1988) 'The crystal structure of SFCA-I $Ca_{3.18}Fe^{3+}_{14.66}Al_{1.34}Fe^{2+}_{0.82}O_{28}$, a homologue of the aenigmatite structure type, and new structure type, and new crystal refinements of _-CCF, $Ca_{2.99}Fe^{3+}_{14.30}Fe^{2+}_{0.55}O_{25}$ and Mg-free SFCA, $Ca_{2.45}Fe^{3+}_{9.04}Al_{1.74}Fe^{2}_{0.16}S$', *Neues Jahrbuch Miner. Abh*, 173(1), pp. 93–117.

Mumme, W. G. (2003) 'The crystal structure of SFCA-II, $Ca_{5.1}Al_{9.3}Fe_{18.7}^{3+}Fe_{0.9}^{2+}O_{48}$ a new homologue of the aenigmatite structure-type, and structure refinement of SFCA-type, Ca2Al5Fe7O20. Implications for the nature of the "ternary-phase solid-solution" previously reported in', *Neues Jahrbuch Fur Mineralogie-Abhandlungen*, 178(3), pp. 307–335. doi: 10.1127/0077-7757/2003/0178-0307.

Nyembwe, A. M., Cromarty, R. D. and Garbers-Craig, A. M. (2016a) 'Effect of concentrate and micropellet additions on iron ore sinter bed permeability', Mineral Processing and Extractive Metallurgy Transactions of the Institutions of Mining and Metallurgy: Section C. Taylor & Francis, 125(3), pp. 178–186. doi: 10.1080/03719553.2016.1180033

Nyembwe, A. M., Cromarty, R. D. and Garbers-Craig, A. M. (2016b) 'Prediction of the granule size distribution of iron ore sinter feeds that contain concentrate and micropellets', *Powder Technology*. Elsevier B.V., 295, pp. 7–15. doi: 10.1016/j.powtec.2016.03.010.

Nyembwe, A. M., Cromarty, R. D. and Garbers-Craig, A. M. (2017) 'Relationship Between Iron Ore Granulation Mechanisms, Granule Shapes, and Sinter Bed Permeability', *Mineral Processing and Extractive Metallurgy Review*. Taylor & Francis, 38(6), pp. 388–402. doi: 10.1080/08827508.2017.1323750.

Pal, J., Ghorai, S., Venkatesh, P., Goswami, M. C., Bandyopadhyay, D. and Ghosh, S. (2013) 'Development of fluxed micropellets for sintering utilising iron oxide waste fines', *Ironmaking & Steelmaking*, 40(7), pp. 498–504. doi: 10.1179/1743281212Y.0000000069.

Pal, J. (2016) 'Utilization of Microfines in Iron and Steel Making', *Steelworld*, June, pp. 86–90.

Panigrahy, S. C., Verstraeten, P., Dilewijns, J. and Sintering, A. (1984) 'Influence of MgO Addition on Mineralogy of Iron Ore Sinter', 15(March).

Patrick, T. R. C. and Lovel, R. R. (2001) 'Leaching Dicalcium Silicates from Iron Ore Sinter to Remove Phosphorus and Other Contaminants', *ISIJ International*, 41(2), pp. 128–135.

Pettersson, M. (2015) *Effect of magnetite , hematite and pellet screenings as sinter feed*.

Poveromo, B. J. (2010) '5th International Congress on the Science and Technology of Ironmaking', in *Steel Times International*, pp. 28–30.

Poveromo, B. J. (2018) 'Iron Ore For Alternate Iron Processes', *Society for Mining and Metallurgy*, 1(1), pp. 1–7.

Roshan, V., Kumar, K., Kumar, R. and Nageswara Rao, G. V. S. (2018) 'Preparation of Iron Ore Micro-pellets

© University of Pretoria

and Their Effect on Sinter Bed Permeability', *Transactions of the Indian Institute of Metals*. Springer India, 71(9), pp. 2157–2164. doi: 10.1007/s12666-018-1347-3.

Scarlett, N.V.Y, Pownceby, M.I, Madsen, I. C. and Christensen, A. N. (2004a) 'In situ X-ray diffraction analysis of iron ore sinter', *Journal of Applied crystallography*, 37(3), pp. 362–368.

Scarlett, Nicola V.Y, Pownceby, M. I., Madsen, I. C. and Christensen, A. N. (2004b) 'Reaction sequences in the formation of silico-ferrites of calcium and aluminum in iron ore sinter', *Metallurgical and Materials Transactions B: Process Metallurgy and Materials Processing Science*, 35(5), pp. 929–936. doi: 10.1007/s11663-004-0087-4.

Sharma, S. K., Verma, D. S., Khan, L. U., Kumar, S. and Khan, S. B. (2018) *Handbook of Materials Characterization*, *Handbook of Materials Characterization*. doi: 10.1007/978-3-319-92955-2.

Umadevi, T., Deodhar, A. V., Mahapatra, P. C., Prabhu, M. and Ranjan, M. (2010) 'Influence of coating granulation process on iron ore sinter quality and productivity', *Steel Research International*, 81(9), pp. 716–723. doi: 10.1002/srin.201000030.

Umadevi, T., Brahmacharyulu, A., Roy, A. K., Mahapatra, P. C., Prabhu, M. and Ranjan, M. (2011) 'Influence of Iron Ore Fines Feed Size on Microstructure, Productivity and Quality of Iron Ore Sinter', *ISIJ International*, 51(6), pp. 922–929. doi: 10.2355/isijinternational.51.922.

Van den Berg, T. and De Villiers, J. P. R. (2009) 'An assessment of the production of fine material in iron ore sinter', *Mineral Processing and Extractive Metallurgy*, 118(4). doi: 10.1179/174328509X455313.

Venkataramana, R., Gupta, S. S. and Kapur, P. C. (1999) 'A combined model for granule size distribution and cold bed permeability in the wet stage of iron ore sintering process', *International Journal of Mineral Processing*, 57(1), pp. 43–58. doi: 10.1016/S0301-7516(99)00005-8.

Webster, N. A. S., Pownceby, M. I., Madsen, I. A. N. C. and Justin, A. (2012) 'Silico-ferrite of Calcium and Aluminum (SFCA) Iron Ore Sinter Bonding Phases : New Insights into Their Formation During Heating and Cooling', *Metallurgical and Materials Transactions B: Process Metallurgy and Materials Processing Science*, 43B(1), pp. 1344–1356. doi: 10.1007/s11663-012-9740-5.

Webster, N. A. S., Pownceby, I., Madsen, I. C. and Kimpton, A. (2012) 'Silico-ferrite of Calcium and Aluminum (SFCA) Iron Ore Sinter Bonding Phases: New Insights into Their Formation During Heating and Cooling', 43(6), pp. 1344–1357. doi: 10.1007/s11663-012-9740-5.

Webster, N. A. S., Pownceby, M. I., Madsen, I. A. N. C., Studer, A. J., Manuel, J. R. and Kimpton, J. A. (2014) 'Fundamentals of Silico-Ferrite of Calcium and Aluminum (SFCA) and SFCA-I Iron Ore Sinter Bonding Phase Formation : Effects of CaO : SiO 2 Ratio', *Metallurgical and Materials Transactions B: Process Metallurgy and Materials Processing Science*, 45(December), pp. 2097–2105. doi: 10.1007/s11663-014-0137-5.

Yang, C., Zhu, D. and Pan, J. (2018) 'Granulation Effectiveness of Iron Ore Sinter Feeds : Effect of Ore Properties Granulation Effectiveness of Iron Ore Sinter Feeds : Effect of Ore Properties', (October). doi: 10.2355/isijinternational.ISIJINT-2018-141.

Yang, L. X. and Matthews, E. (1997) 'Sintering reactions of magnetite concentrates under various atmospheres', *ISIJ International*, 37(11), pp. 1057–1065.

Yang, L. X. and Davis, L. (1999) 'ssimilation and mineral formation during sintering for blends containing magnetite concentrate and hematite/pisolite sintering fines', *SIJ International*, 39(3), pp. 239–245.

Zi-wei, Y., Mao-fa, J. and Li-xian, X. (2006) 'Effects of mineral composition and microstructure on crack resistance of sintered ore', *Journal of Iron and Steel Research, International*, 13(4), pp. 9–12.

© University of Pretoria

© University of Pretoria

Appendix

A.1 Granulation Data

Calculations of gain/loss, material transfer and material transfer efficiency were carried out using the particle sizes distribution of the sinter mixtures. X was read off the gain/loss graphs.

Table A1: Granulation data for the base case sinter mixture.

Size (mm)	Mass % (BG)	Mass % (AG)	%Gain/Loss
4	29.63	34.43	4.80
2	31.63	41.90	10.27
1	18.14	19.79	1.65
0.5	6.99	3.62	-3.37
0.35	13.60	0.26	-13.35
X	0.8	mm	
S	16.71	%	
E_X	81.18	%	

Table A2: Granulation data for the 0% MP sinter mixture.

Size (mm)	Mass % (BG)	Mass % (AG)	%Gain/Loss
4	19.29	34.71	15.42
2	21.95	39.20	17.25
1	12.96	21.35	8.39
0.5	4.86	4.62	-0.24
0.35	40.95	0.12	-40.82
X	0.5	mm	
S	40.82	%	
E_X	99.68	%	

Table A3: Granulation data for the 10% MP sinter mixture.

Size (mm)	Mass % (BG)	Mass % (AG)	%Gain/Loss
4	21.97	39.12	17.15
2	25.14	44.13	18.99
1	13.83	14.73	0.90
0.5	4.86	1.95	-2.91
0.35	33.60	0.07	-33.53
X	0.85	mm	
S	36.44	%	
E_X	94.77	%	

© University of Pretoria

Table A4: Granulation data for the 20% MP sinter mixture.

Size (mm)	Mass % (BG)	Mass % (AG)	%Gain/Loss
4	21.97	39.12	17.15
2	25.14	44.13	18.99
1	13.83	14.73	0.90
0.5	4.86	1.95	-2.91
0.35	33.60	0.07	-33.53
X	0.50	mm	
S	25.03	%	
E_X	95.45	%	

Table A5: Granulation data for the 30% MP sinter mixture.

Size (mm)	Mass % (BG)	Mass % (AG)	%Gain/Loss
4	27.36	38.37	11.02
2	31.53	38.59	7.05
1	15.58	18.62	3.05
0.5	4.86	4.13	-0.72
0.35	18.86	0.28	-18.58
X	0.55	mm	
S	19.30	%	
E_X	81.36	%	

Table A6: Granulation data for the 40% MP sinter mixture.

Size (mm)	Mass % (BG)	Mass % (AG)	%Gain/Loss
4	30.04	31.62	1.58
2	34.73	39.48	4.75
1	16.45	20.73	4.28
0.5	4.86	7.12	2.26
0.35	11.51	1.05	-10.46
X	0.45	mm	
S	10.46	%	
E_X	90.09	%	

© University of Pretoria

A.2 XRD Data

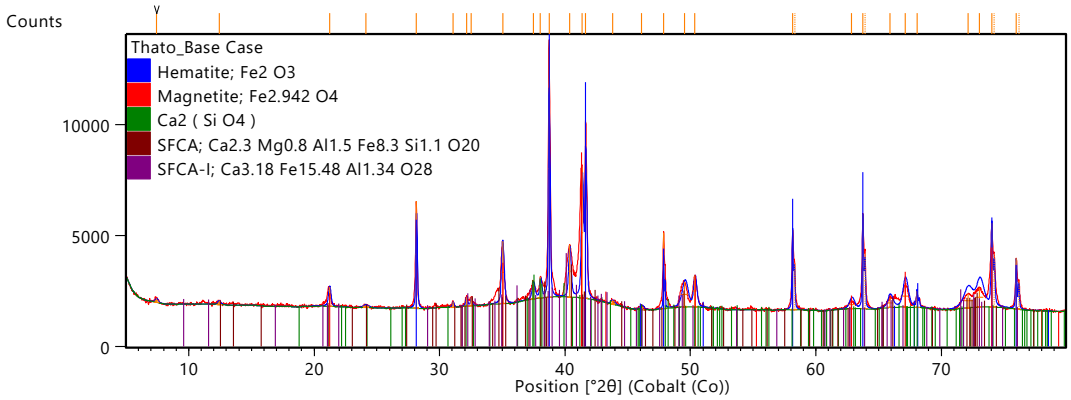

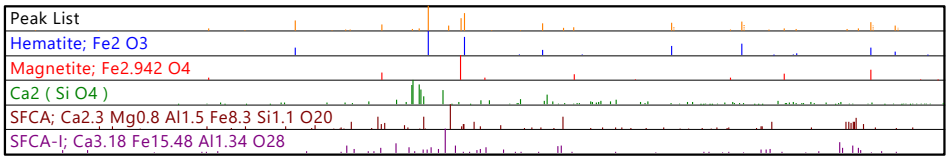

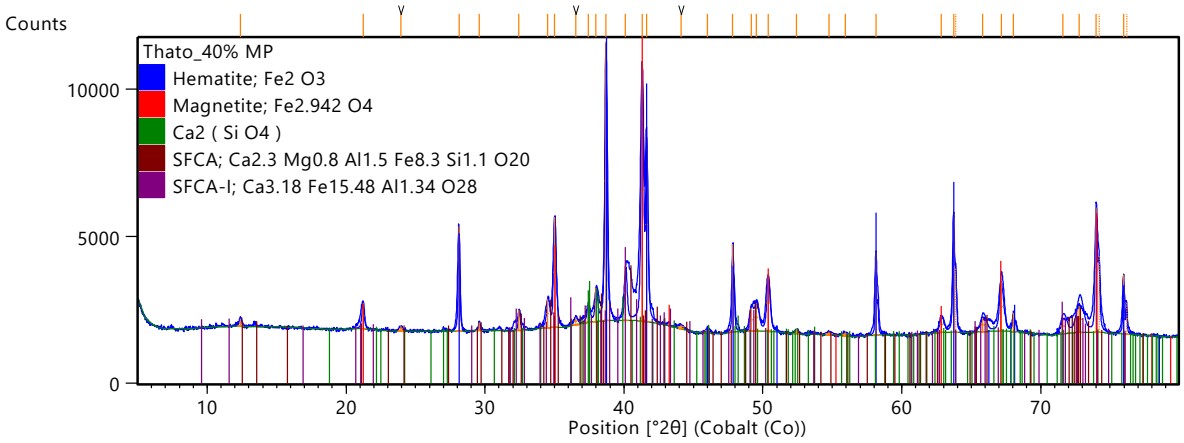

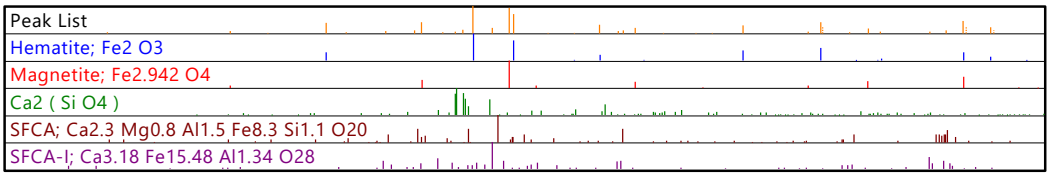

© University of Pretoria

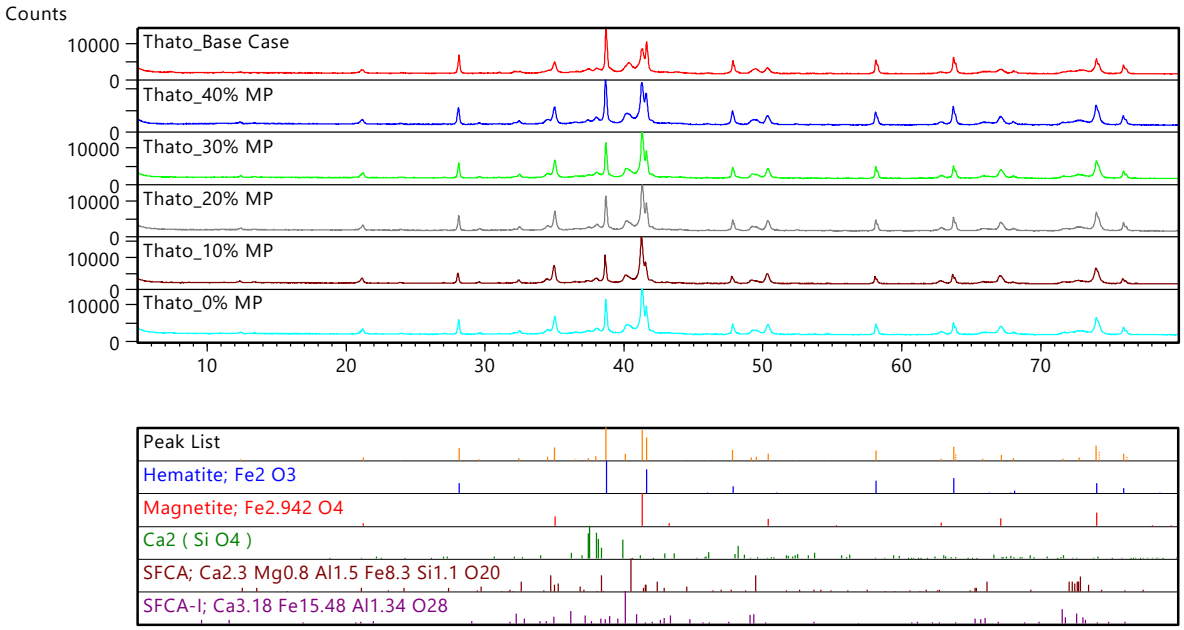

Table A7: Quantitative XRD analysis for the sinters produced.

Mixture	Hematite	Magnetite	SFCA	SFCA-I	Larnite	Total
Base case	30.70 (0.69)	17.08 (0.57)	35.48 (2.04)	9.96 (1.62)	6.78 (1.08)	100
0% MP	22.77 (0.57)	29.84 (0.63)	37.71 (1.59)	3.44 (1.05)	6.24 (0.72)	100
10% MP	22.14 (0.69)	38.34 (0.96)	30.07 (2.01)	5.33 (1.86)	4.12 (0.75)	100
20% MP	25.38 (0.69)	32.81 (0.93)	32.65 (1.56)	4.38 (1.44)	4.77 (0.81)	100
30% MP	24.89 (0.69)	31.73 (0.81)	32.99(1.59)	6.32 (1.32)	4.07 (0.72)	100
40% MP	30.37 (0.69)	25.40 (0.66)	31.87 (1.68)	7.92 (1.44)	4.44 (0.69)	100

(x.xx) = 3 σ error

A.3 Production Rate Data

Table A8: Production rate data for the sinters produced.

Sinter	Time	Std Dev	Minus 5 (%)
Base Case	20.90	2.19	32.79
0% MP	27.87	1.06	34.61
10% MP	28.53	1.00	31.68
20% MP	30.16	1.97	33.05
30% MP	28.35	0.48	32.87
40% MP	27.30	0.90	36.24

© University of Pretoria

© University of Pretoria